國立交通大學

電子工程學系 電子研究所

博 士 論 文

第二型砷化銦鎵/砷銻化鎵 "W" 量子井之光學特性及

光激發中紅外線雷射之研究

Optical Characteristics of Type-II InGaAs/GaAsSb "W"

Quantum Wells and Optically-Pumped Mid Infrared Lasers

研 究 生：潘建宏

指導教授：李建平 教授

中 華 民 國 一〇一 年 十一 月
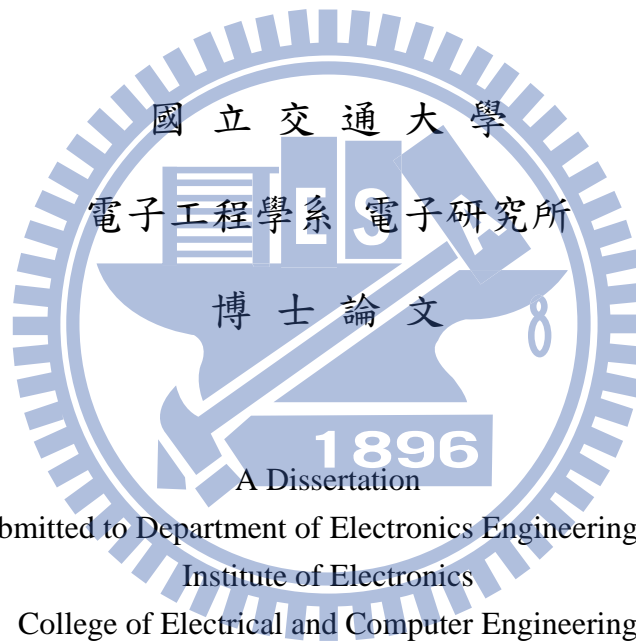
第二型砷化銦鎵/砷銻化鎵 "W" 量子井之光學特性

及光激發中紅外線雷射之研究

Optical Characteristics of Type-II InGaAs/GaAsSb "W"

Quantum Wells and Optically-Pumped Mid Infrared Lasers

研 究 生：潘建宏　　　　　Student：Chien-Hung Pan

指導教授：李建平　　　　　Advisor：Dr. Chien-Ping Lee

國 立 交 通 大 學

電子工程學系 電子研究所

博 士 論 文

中華民國一〇一年十一月

第二型砷化銦鎵/砷銻化鎵 "W" 量子井之光學特性及光激發中紅外線雷射之研究

研究生：潘建宏　　　　　　　　　　　　指導教授：李建平　博士

國 立 交 通 大 學
電子工程學系電子研究所 博士班

摘要

　　此篇論文主要貢獻在探索與開發半導體中紅外線光源，有別於一般較昂貴且不成熟的銻化鎵及砷化銦基材，我們使用較普遍且散熱較佳的磷化銦基板成長第二型砷化銦鎵/砷銻化鎵 "W" 量子井。不同於一般第二型電洞的量子井，此 "W" 結構藉由阻擋層(barrier layer)對電子侷限來增加電子電洞波函數耦合並提升光躍遷率。

　　我們透過理論計算改變各結構參數(例如量子井厚度及砷銻化鎵的比例成分)能得到 2 到 3 微米的發光範圍並且得知發光波長的延伸與光耀遷率的強度有一交替關係(trade-off)，亦即發光波長越長通常伴隨光躍遷率的下降，此為 "W" 結構本質的特性。而在給定一個發光波長下，較薄量子井厚度及較高銻成分的結構設計組合能提供較高的電子電洞耦合。我們更進一步用八個能帶的 k．p 理論來計算能帶關係及不同載子濃度下的材料光增益，在適當的設計下單一層量子井增益即能達到 10^3cm^{-1}，此已符合一般雷射元件的需求。我們也顯示出藉由適當增加電洞量子井的壓縮應變，能使電子電洞的等效質量較平衡進而降低透明載子濃度（ transparency carrier density ）及提高材料光增益。

　　在實驗上，我們使用分子束磊在（001）磷化銦基板上成長一系列的樣品，系統性地分

別改變砷化銦鎵、砷銻化鎵的厚度以及砷銻化鎵合金中銻的比例,在低溫下樣品的光激發螢光光譜可顯示出 2-2.5 微米的波長範圍,其螢光強度與發光波長如前所述有一交換關係,並且如理論預測其螢光積分強度與計算的電子電洞波函數耦合平方成正比。樣品品質表現良好,螢光積分強度從低溫到室溫只約下降了 10 倍。在室溫下我們首次展示出其波長能超過 3 微米。我們透過變功率光激發螢光實驗來研究"W"量子井中第二型能帶排列的特徵,光譜的峰值位置隨激發功率增加而藍移,但不同於一般第二型量子井其藍移量並未與激發光功率的 1/3 次方成正比,對此現象我們提出局域的能態填充(localized states band filling)來解釋,其局域能態來自於合金成分的不均勻及磊晶層表面起伏所致,模擬結果與實驗值可以得到良好的吻合。

最後我們首次成功的展示室溫操作光激發 2.56 微米的"W"量子井中紅外線雷射,此為所知在磷化銦基板上波長最長的能帶間躍遷(interband transition)雷射,其閥值功率密度約為 40kW/cm^2,其特徵溫度 T_0 在操作溫度小於 250K 時為 487.8K,而從 250K 到室溫其 T_0 為 41.8K,此劇烈的 T_0 變化及較小的室溫 T_0 我們認為是歐傑複合所導致,經由不同雷射腔長的實驗萃取波導光損耗以及理論計算波導模態增益,我們得以估計歐傑常數約為 1.67 x10^{-27} cm^6/s。

最後我們提出並評估一方法能將"W"量子井發光波長延升至 3-5 微米波段,此即成長緩衝層將晶格常數轉至~5.94A$^\circ$,並接著使用 In$_{0.7}$Ga$_{0.3}$As/GaSb/In$_{0.7}$Al$_{0.3}$As "W"量子井的結構設計。

Optical Characteristics of Type-II InGaAs/GaAsSb "W" Quantum Wells and Optically-Pumped Mid Infrared Lasers

Student: Chien-Hung Pan   Advisor: Dr. Chien-Ping Lee

Department of Electronics & Institute of Electronics
National Chiao Tung University

Abstract

This dissertation mainly dedicates to explore and develop mid-infrared light sources. In difference with usual expensive and immature InAs-based and GaSb-based materials, we utilized more popular, better thermal conductive InP substrates and employed type-II InGaAs/GaAsSb "W" type quantum wells (QWs). Distinguishing from general type-II hole quantum well, the "W" structure includes barrier layers to confine electrons and to increase electron-hole wavefunction overlap, hence the optical transition rate.

Through theoretical calculations changed with structure parameters (such as QWs thickness and GaAsSb composition), a range of 2-3μm emission wavelength can be derived. It also shows a trade-off situation between the extending of emission wavelength and the intensity of optical transition rate, meaning a longer emission wavelength generally accompanied with a decreased optical transition rate, which is an intrinsic feature for the "W" structure. However, at a given emission wavelength, the design with thinner InGaAs and GaAsSb layers and a higher Sb content in GaAsSb is more desirable, which could provide of a larger electron-hole wavefunction overlap. We further used the eight-band k.p theory to calculate the E-k relation and material gain as a function of carrier density. With a proper design, the material gain of a single "W" QW is able to reach above 10^3 cm^{-1}, which is sufficient for general mid-IR lasers applications. We also pointed out that adopting proper compressive strain in hole QW makes a more balanced electron and hole

masses that could reduce the transparency carrier density and increase the material gain.

In experiments, we grew a series of samples systematically varied with thickness of InGaAs, thickness of GaAsSb and Sb mole fraction in GaAsSb. The photoluminescence (PL) spectra of samples cover the range of 2-2.5 μm at low temperature. The trade-off between optical transition rate and wavelength emission is confirmed as the prediction of the theoretical calculations, where the integrated PL intensity is proportional to the square of electron-hole wavefunction overlap. The samples showed good optical quality that integrated PL intensity only decreases an order from cryogenic temperature to room temperature (RT). For the first time we demonstrated PL emission wavelength longer than 3 μm at RT by the InP-based "W" structure. The type-II band alignment in the "W" structure has been characterized by the power dependent PL measurements. The peak position shifts to shorter wavelength as the excitation power (P_{ex}) increases. It was found the amount of energy shifts does not follow the $P_{ex}^{1/3}$ law as most type II structures. The localized states filling effect due to the surface roughness and alloy fluctuation is proposed to explain the observed phenomenon. The calculated results agree well with the experiment results.

For the first time we demonstrated the room temperature optically-pumped mid-IR "W" type lasers on InP substrates. The lasing wave length is 2.56 μm, which is known as the longest for the InP-based interband transition, with a threshold pumping power density of ~40kW/cm^2. The laser shows a characteristic temperature (T_0) of 487.8K as operated below 250K and a T_0 of 41.8K as operated near room temperature. This abrupt T_0 change and the small T_0 at room temperature are considered due to the dominated Auger processes. An Auger coefficient of 1.67×10^{-27} cm^6/s was estimated via different laser cavity length studies for the extraction of waveguide optical loss and theoretical calculations for the waveguide modal gain.

Finally, we propose and evaluate an approach capable of extending the "W" QWs emission

wavelengths into 3-5µm regime, which uses a metamorphic buffer layer to shift the lattice constant to ~5.94$\mathring{A}$ and then grows the designed "W" QW structure of In$_{0.7}$Ga$_{0.3}$As/ GaSb/In$_{0.7}$Al$_{0.3}$As.
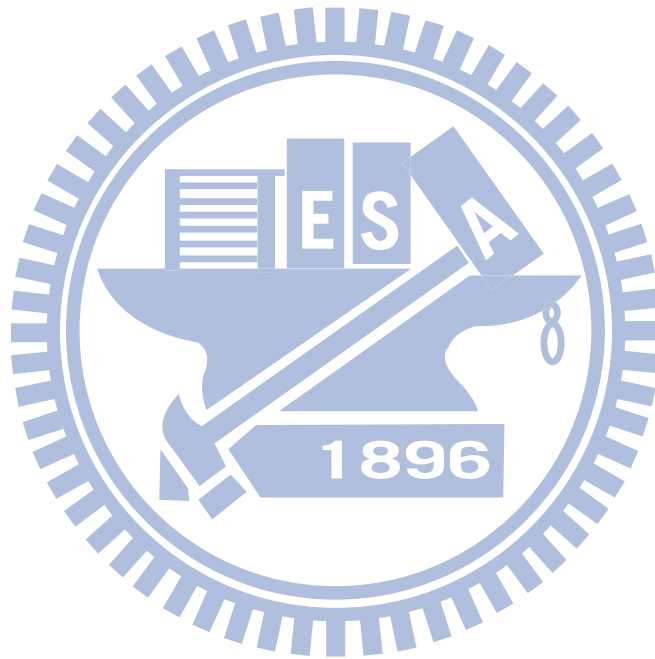
致謝

　　第一個要感謝的就是李建平老師，是以無私的付出與廣闊的胸襟，能成就如此規模的實驗室，讓我能在裡頭馳騁、犯錯以及學習，老師總在適時給予提點，在論文上給予關鍵的指導，能遇到如此好的老師，總深深地感到幸運及感恩。接著感謝林聖迪老師幫忙維護整個大實驗室的運作，當然包括辛勞的ＭＢＥ事務，從老師身上也看到對道理追求的態度。感謝林國瑞老師，光電子學課程真的很受用。感謝曾經一起生活的畢業學長們：羅明城博士、凌鴻緒博士及林大鈞博士，有你們的傳承及實驗的討論使研究順利不少。感謝實驗室一同奮鬥的夥伴們：鄭旭傑、蘇聖凱、林建宏、林岳民、傅英哲、張家豪、林仕偉、李宗霖、徐偉程、周柏存...等，在實驗上互相幫忙及討論，還能一起熱血的運動流汗，讓彼此都很健康，可以分享喜怒哀樂，掃除研究路途上的陰霾。最後，最重要的，要感謝我最親愛的家人，我的父母及姊姊，沒有爸媽你們建立如此健全沒有經濟負擔的家庭，還有對我人生路上的指引，便沒有今日的我，能當你們兒子真有福氣，真要好好感謝你們，榮耀你們。

CONTENTS

Table Captions

Figure Captions

Chapter 1

Introduction

1.1 Mid infrared applications

Mid infrared (mid-IR) light sources have many applications that can benefit human society [1, 2]. Fundamental vibration, rotation and other movements of molecules mainly resonate with mid-IR photons and cause substantial absorptions. Since resonant frequencies primarily depend on molecular structures, the molecular species can be identified by the characteristics of the absorption spectrum.   The molecular density can also be measured by the absorption intensity. Figure 1.1(a) shows a typical setup for the mid-IR absorption spectroscopy, and Fig. 1.1(b) shows the absorption lines of some important molecules within the wavelength range of 2-5 µm, which is derived from the HITRAN database [3]. The application of the light sources in this wavelength range covers a wide area of environmental protection, industrial safety, healthcare, biomedicine, and homeland security. Some of the examples include trace gas and greenhouse gas sensing, environmental monitoring, industrial in situ gaseous species analysis and control, noninvasive breath air diagnosis, mid-IR medical laser surgery, hazard chemical agents detection, etc. A resolution down to part per trillion of mole fraction could be achieved with advanced techniques like cavity ring-down spectroscopy (CRDS) [1]. The mid-IR wavelengths of 3-5µm also coincide with the atmospheric transparency window, where light has low water vapor absorption and atmospheric scattering. This feature can facilitate other applications such as free-space optical communication, range finding and remote sensing systems. To meet the demand in so many applications, cheap and reliable mid-IR light sources are needed. III-V semiconductor lasers are undoubtedly suitable candidates. With advantages of a small size, compatibility for system integration, high output

efficiency, cost effective, etc., the Sb based semiconductor light sources have drawn a lot of attention in recent years. Next section will give a brief review of the development and current status of mid-IR semiconductor lasers.
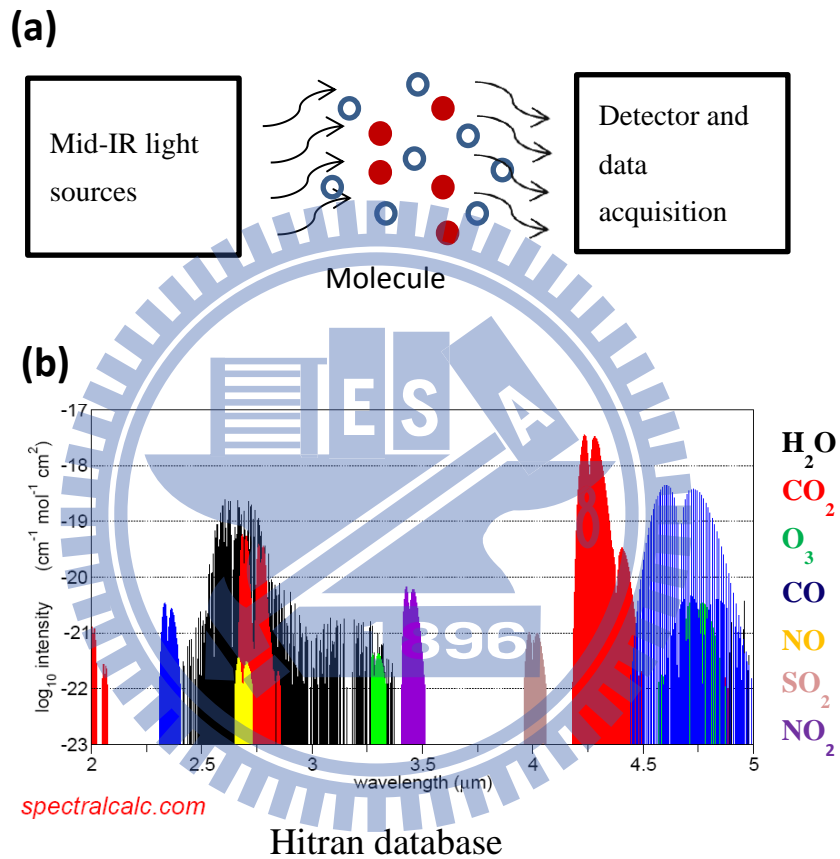
Fig 1.1(a) A Scheme of a typical setup for mid-IR spectroscopy. (b) Absorption lines and intensity of some important molecules (derived from Hitran database [ref. 3]).

1.2   A brief review of III-V semiconductor mid-IR lasers

Direct band gaps in Γ-valley of III-V semiconductors and their relative band alignments of conduction band (CB) and valence band (VB) edges for binary compounds are plotted against lattice constant in Fig. 1.2 (a) and Fig. 1.2 (b) respectively [4]. GaSb based material systems, which are made of either binaries or compounds from InAs, GaSb, and AlSb with lattice constant $\sim 6.1\text{\AA}$, attracts most interests for the development of semiconductor mid-IR lasers and has been researched over two decades.
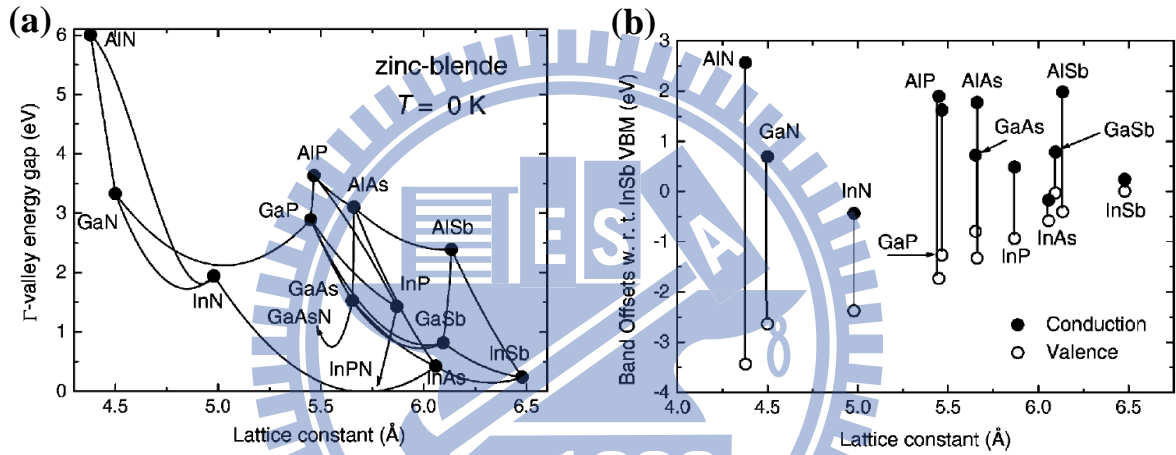
Fig 1.2(a) Direct Γ-valley band gaps of binary (filled dot) and ternary (joined curve) III-V semiconductors. (b) Relative band alignments of conduction band (CB) and valence band (VB) edges for binary semiconductors [ref. 4].

The first double hetero structure (DH) mid-IR laser with InGaAsSb active region was reported by Caneau et al. in 1985 using liquid phase epitaxy (LPE). It had an emission wavelength of 2.2μm and a threshold current density $\sim 6.9\text{kA/cm}^2$ [5]. The $In_xGa_{1-x}As_ySb_{1-y}$ quaternary alloy can actually cover a much wider wavelength range from 1.7μm to 4.3μm while remaining to be lattice matched to GaSb. However, the alloy grown by LPE has a serious miscibility problem that prevents the extending of the emission wavelength. With the appearance of more advanced growth technologies such as molecular beam epitaxy (MBE) and metal organic chemical vapor deposition (MOCVD), the thermally meta-stable alloys are

easier to grow and the material quality is greatly improved. The MBE grown InGaAsSb/AlGaAsSb DH laser emitting at 2.2μm with a low threshold current density (940A/cm^2) at room temperature (RT) was achieved by Choi et al. in 1991 [6]. These advanced technologies also are able to create sharp hetero interface and precisely control the layer thickness within a few nanometers. Taking the advantage of these capabilities and adopting the design of separate confinement heterostructure (SCH), the performance of mid-IR lasers were further improved. The design contains a single quantum well (QW) or multiple quantum wells (QWs) in an active region to confine carriers, and the active region is embedded in a waveguide which is formed by lower and upper low refraction index cladding layers to confine electromagnet waves. The structure of QW has many advantages than the DH structure. One is to reduce the threshold current density below the order of ~kA/cm^2. Others are like higher differential gain and better temperature performance. Those can be attributed to the reduced 2D density state and the enhanced optical oscillation strength of the quantum structure.

There are two types of QW lasers in terms of band edge alignment of the heterojunction in the active region. The type-I QW lasers, as shown in Fig 1.3(a), have the CB and VB edges of QW lying deeper than the CB and VB edges of surrounding barriers, so both electrons and holes are confined inside the QW layer [7]. The type-I InGaAsSb/AlGaAsSb QW mid-IR lasers perform well in the wavelength region of ~2-2.3μm. However, a higher threshold current density and a lower operation temperature are needed if one wants to extend to longer wavelengths. There are two main reasons accounted for this trend. One is that as increasing the indium and arsenide composition in InGaAsSb alloy for a longer emission wavelength, the hole confinement is insufficient caused by a reduced VB offset to the adjacent barrier layer. The other reason is the more pronounced nonradiative Auger recombination, especially for CHHS process here (the recombination of the CB to the heavy hole band accompanied by the

transition of heavy hole band to the split-off band), for a small band gap material. The laser performance degrades even quickly beyond 2.7μm owing to the miscibility effect which is inevitable for the alloy even using the MBE technique [1, 8]. The design of the strain-compensated InGaAsSb/AlGaAsSb QWs, which have higher arsenic fraction in the tensile-strained barrier layers and higher indium fraction in compressive-strained QW layers, can provide an adequate VB offset and therefore an extended lasing wavelength ~2.89μm at RT was reported [9]. However it is still difficult to extend the lasing wavelength beyond 3μm by this kind of structure. In 2005, the design of a quinternary AlGaInAsSb SCH region was firstly employed by Grau et al. and demonstrated 3.26μm type-I QW lasers at 50°C under pulsed operation [10]. The work of optimization continues and several breakthroughs have been archived. By using the AlGaInAsSb SCH region, RT operated mid-IR lasers with CW output powers have been reported: 3μm/310mW [11], 3.1μm/90mW, 3.2μm/160mW, 3.32μm/50mW, 3.44μm/29mW [12], and the lasing wavelength up to 3.73μm was obtained in the pulsed operation [13].

Mid-IR lasers with wavelengths beyond 3μm are achievable using type-II QWs and interband cascade active region. The type-II QWs have staggered band edge alignment to the surrounding barriers, thus only one kind of carriers is confined inside the QWs and the other one is located in the region of the barrier layers. Figure 1.3(b) shows the band alignment of electron confined type-II QW lasers [7]. The optical transition takes place by recombination of the spatially separated electrons and holes. However the reduced electron-hole wavefunction overlap causes the optical oscillator strength to reduce, hence resulting a small optical gain, which limits the laser performance. The type-II "W" QWs were proposed and demonstrated by the research group of Naval Research Laboratory (NRL) in 1995. The "W" structure, as shown in Fig. 1.3(c), confines holes in the center GaInSb QW and electrons in the coupled two InAs QWs formed by the surrounding AlSb barrier layers to increase the

electron-hole wavefunction overlap [8]. The "W" configuration preserves two dimensional

density states for both carriers and can suppress the Auger processes. The type-II "W" QWs

lasers with emission wavelengths in the range of 3-7.3 μm by optical pumping were reported,

and an electrical injected laser using five periods of the "W" QWs emitting at ~3.5μm in CW

operation up to T=218K has been demonstrated [14-17].
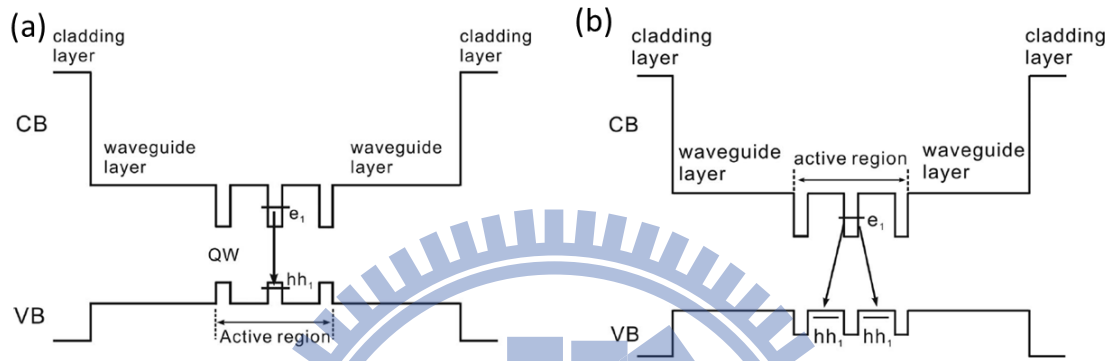
Fig 1.3(a) Band alignments and fundamental electron-hole optical transition of type-I, and (b) type-II QW lasers [ref. 7].
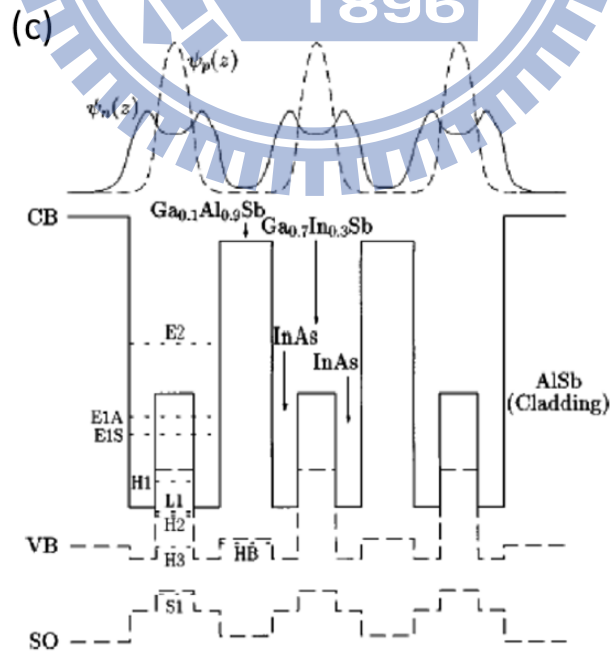
(d)
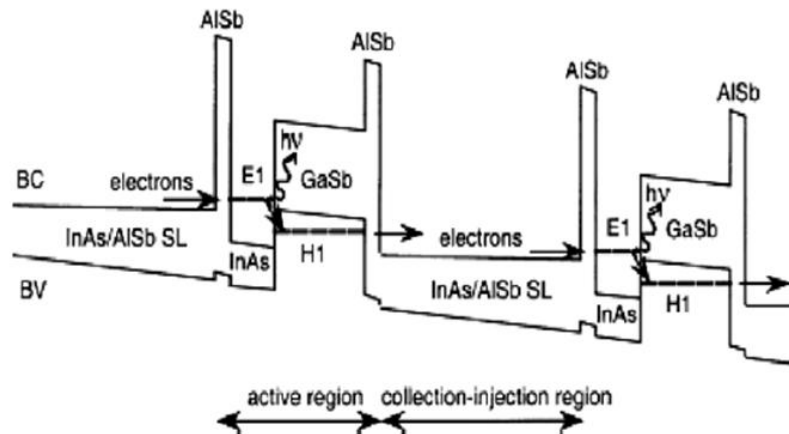
Fig 1.3(c) Band alignment along with ground state electron and hole wavefunctions of type-II "W" structure QWs. (d) Band profile (not to scale) under bias of an interband quantum cascade active region and also indicated with the carrier optical transition in the AlSb/InAs/GaSb quantum well [ref. 8].

Interband cascade lasers are promising for the wavelength range of 3-4μm. Optical gain is realized through a sequential cascade processes in such structure, as shown in Fig. 1.3 (d). Electrons enter from the InAs/AlSb supper lattice (SL) injection region, and then resonantly tunnel into InAs QW region, in which then undergo an optical transition to the adjacent GaSb valence band states (in other words, a recombination process with holes in the GaSb layer). This transition is made possible due to the large band edge offset at the GaSb/AlSb interface. Finally, by using the broken-gap alignment carriers are able to resonantly tunnel back to the next collection/injection region rapidly (with rate ~0.1 ps). The processes repeat in the following periods. The interband quantum cascade laser emitting at 3.8-3.9 μm operated at 210K in pulsed mode with the differential quantum efficiency >460%, and peak output power > 4W/facet was reported [18]. "W" type QWs have been used in interband cascade lasers for better performance. In 2008, the first above RT CW operated interband cascade laser with

7

5-stage "W" QWs design emitting at 3.75µm has been reported [19]. With further optimization, a record of 59mW CW output power with a 3.4% wall plug efficiency at 300K for such devices have been obtained [20]. By varying the thickness of InAs in "W" QWs, the interband cascade lasers have been demonstrated accurate lasing wavelength tuning in the region of 3-4 µm, which could facilitate practical implementations [21].

We restrict ourselves in this brief review for interband transition active region lasers; therefore the part of intraband cascade lasers is not included here. Intraband cascade lasers are suitable for even longer wavelengths (> 4µm). However, it is hard to fabricate due to the difficulties of requiring thickness controllability in few monolayers and up to thousands of sharp interfaces among layers. Besides, a high voltage is needed as operating the device, which generates lots heat cross the junctions, thus extra thermal management is always needed.

1.3   Research motivation

GaSb and InAs substrates are conventionally used for the development of mid-IR lasers. However, they are more expensive, with lower thermal conductivity and immature process technology as comparing to more popular substrates such as GaAs and InP. Thus, replacing the platform toward GaAs or InP substrate is highly desirable for the fabrication of mid-IR lasers. However, Sb-based mid-IR laser structures has large lattice mismatch between GaAs or InP substrate, which generates dislocation and degrades the laser performance. The method of inter facial misfit (IMF) arrays grown by MBE has been employed to reduce threading dislocations of lattice-mismatched GaSb-based mid-IR lasers on Si and GaAs substrates. Room temperature CW operated lasers emitting at 2µm and ~2.2µm have been demonstrated respectively on Si and GaAs substrates by Reboul and Rodriguez et al. [22, 23]. A thick

InAlSb buffer layer (~8 μm) has been used by Nash et al. to eliminate defects for InGaSb QW mid-IR laser grown on GaAs substrate, which has 3.3μm emission wavelength in pulse operation up to 219K [24].

InP-based material remains a relatively unexplored area in terms of interband mid-IR lasers. Type-I QW with emission wavelength longer than 2 μm on InP is difficult due to lattice mismatch. The longest wavelength reported is 2.33 μm with a highly strained InAs/InGaAs system [25]. However, if we use the type-II InGaAs/GaAsSb heterostructure on InP substrates, we can bypass the requirement for small band gap materials by using the staggered band alignment and therefore the wavelength can be extended longer without being limited by the band gaps of the constituent materials. The "W" type QWs with the type II staggered band alignment using InGaAs/GaAsSb have been shown to be able to extend the lasing wavelength in the mid-infrared range [26-29]. Thanks to the development of 1.3 and 1.55 μm lasers for fiber communication applications. InP-based system has very mature process technologies including regrowth of devices. Mid-IR optoelectronics using type-II InGaAs/GaAsSb hetero-structure on InP substrates have caught attention recently [30, 31].

This dissertation is aimed to investigate type-II InGaAs/GaAsSb "W" type QWs on InP substrates in both theory and experiments, and then to design and fabricate the mid-IR lasers with "W" type QWs. The organization of this dissertation is described in the following section.

1.4   Organization of this dissertation

Chapter 2 presents theoretical studies of the "W" type structure of QWs. The nature of the tradeoff between extending of wavelength and optical oscillation strength is analyzed by the results of calculations based on simple one-band effective mass approximation. The E-k band structures of "W" QWs are simulated by using the 8-band $k.p$ theory to look more insight to

the characteristics like band edge effective masses and momentum matrix elements. The results lead to calculations of optical gain based on basic laser theorem, which can be treated as a design guideline of "W" laser active region.

Chapter 3 presents experimental techniques including how to prepare samples, material analysis methods, and device measurement setups. Our samples are grown by a MBE system. X-ray diffraction helps to understand the lattice constant of epi layers. Photoluminescence (PL) studies could characterize the type-II nature of grown samples. And the apparatus to measure optically pumped "W" mid-IR lasers will be detailed.

Chapter 4 describes PL experiment results of the designed samples, which will be compared and found consistent with theoretical predictions. The peak of emission wavelength shifting to short wavelength as increasing PL excitation power (P_{ex}) reveals the nature of type-II structure; however which does not follow the $P_{ex}^{1/3}$ law as described in published literature. This observation will be discussed more and reasonably explained by a proposed model.

Chapter 5 describes the structure of the designed "W" QWs mid-IR laser along with the waveguide calculation. The lasing results are demonstrated via optical pumping experiments. Studies of different laser cavity lengths and operation temperatures are implemented to analyze "W" lasers. Laser performance related parameters such characteristic temperature (T_0) and internal loss (αi) are extracted. It also includes a detailed discussion of Auger process and an estimation of Auger coefficient, which are important for mid-IR lasers.

Chapter 6 gives conclusions and suggestions for future works.

Chapter 2

Theoretical studies of InGaAs/GaAsSb type-II "W" type quantum wells on InP substrates

The type-II InGaAs/GaAsSb heterostructure has staggered band alignment that offers a good strategy for developing mid-IR light sources on InP substrates. The "W" type structure introduces barrier layers for better electron confinement and carriers wavefunction overlap and hence optical oscillator strength. This chapter gives the theoretical view of the "W" structure. One band effective mass approximation provides a simple way to study the trade-off nature of "W" type QWs, longer emission wavelength accompanied with reduced wavefunction overlap. More deliberate calculations are carried based on the 8-band $k.p$ theory, which eventually leads to optical gain calculations for needs of design considerations of "W" mid-IR lasers. The gain spectra and their peak values at various carrier densities were calculated. We have found that a more balanced electron and hole masses in the type-II "W" QWs can benefit the material gain. In our designed cases, we have seen that the reduced hole effective mass due to a higher Sb content can partially compensate the gain loss caused by the reduced transition matrix element. Based on the optimized design, a material gain above 10^3 cm^{-1} is readily achievable for a single properly designed "W" quantum well. In order to be self-contained, all simulation parameters used will be listed as completely as possible.

2.1 Band alignments of "W" type quantum well

Four kinds of ternary semiconductors can be lattice matched to InP substrate with a lattice constant of 5.87Å, which are InAlAs, InGaAs, GaAsSb, and AlAsSb. Table 2.1 lists their

alloy compositions and band gaps. Their band alignments together with band offset values are depicted in Fig. 2.1, which are based on experiment results in literatures[32-34].

Table 2.1 Room temperature (300K) and low temperature (0K) direct band gaps of ternary alloys lattice matched to InP substrate.

		$In_{0.52}Al_{0.48}As$	$In_{0.53}Ga_{0.47}As$	$GaAs_{0.49}Sb_{0.51}$	$AlAs_{0.56}Sb_{0.44}$
Γ-Γ direct band gap (eV)	0K	1.51	0.81	0.81	2.5
	300K	1.42	0.73	0.72	2.4
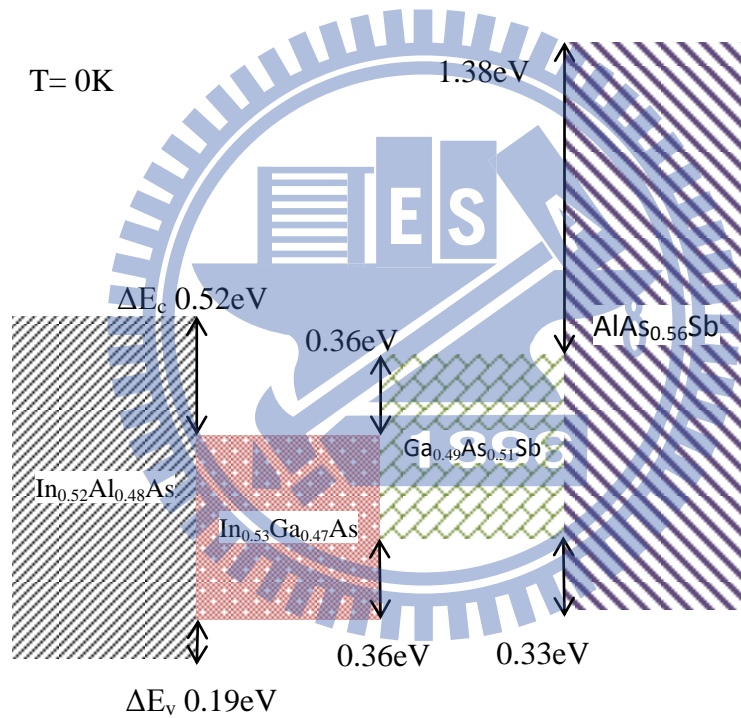
Fig 2.1 Band lineups, with values of conduction and valence band offsets (ΔE_c and ΔE_v) indicated, of the four ternary alloys lattice matched to InP substrate.

In this material system, the two narrower bandgap materials, InGaAs and GaAsSb, form a type II heterjunction. The transition between the conduction band state in InGaAs and the valence band state can give out light emission with wavelength longer that the direct band-to-band transition in individual materials. Based on the band offset, the energy

difference between the conduction band edge of InGaAs and the valence band edge of GaAsSb is ~0.5eV, which can generate a ~2.5 μm light emission [35]. The two wider bandgap materials, InAlAs and AlAsSb, form type-I heterojunctions with the two narrower bandgap materials and can be used as barrier layers for carrier confinement. The emission wavelength can be further extended by increasing either the indium content in InGaAs alloy or the antimony fraction in GaAsSb alloy. To better understand this, the band edge evolutions by altering the alloy compositions will be described in next paragraph.

The calculations are based on the "model-solid" theory, which uses deformation potentials to predict behavior of band offsets in either lattice matched or pseudomorphic layers[36, 37]. Here only gives the case that normal directions of ternary alloys are all along [001]. In the condition without strained, the lattice constant (a_0) of a ternary alloy $A_xB_{1-x}C$ is assumed to follow the Vegard law and estimated from the lattice constants of two binary constituents.

$$a_{0}\_A_xB_{1-x}C \ = \ x\, a_{0}\_AC + (1-x)\, a_{0}\_BC\,, \tag{2.1.1}$$

Band gap (E_g), spin-orbit split-off energy (Δ_0), average valence band edge (E_{vav}), i.e. the average of the heavy-hole, light-hole, and spin-orbit split-off bands ($E_{hh}+E_{lh}+E_{so}$)/3, and other parameters of the ternary are assumed fitted to a simple empirical quadratic formula:

$$P_{A_xB_{1-x}C} = x\, P_{AC} + (1-x)P_{BC} - x\,(1-x)C_{ABC} \ \ , \tag{2.1.2}$$

where P represents an arbitrary semiconductor parameter, and C is so called the bowing parameter, which accounts for the deviation from a linear interpolation of the two constituent binaries. In general, the band gap bowing parameter of ternary alloy is negative, which means the ternary band gap is always smaller than the linear interpolation result. The reason can be originated to the disorder effect formed by the presence of different cations or anions. Conduction band (E_c) and valence band (E_v) of the alloy can be described as:

$$E_v = E_{hh} = E_{lh} = E_{vav} + \Delta_0/3, \text{ (where } E_{hh} \text{ and } E_{lh} \text{ degenerated)} \tag{2.1.3}$$

$$E_c = E_g + E_v. \tag{2.1.4}$$

A pseudomorphic layer implicates a thin epi layer that can bear the lattice mismatch by subjecting its in-plan lattice constant to the underneath host material. The strain, expressed by biaxial strain $\varepsilon_{\parallel}$ and uniaxial strain $\varepsilon_{\perp}$ described below, held within the pseudomorphic layer could change its electronic properties:

$$\varepsilon_{\parallel} = (a_s - a_0)/a_0, \tag{2.1.5}$$

$$\varepsilon_{\perp} = -\frac{2C_{12}}{C_{11}}\varepsilon_{\parallel}, \tag{2.1.6}$$

where a_s and a_0 denote substrate lattice constant and unstrained alloy lattice constant. C_{12} and C_{11} refer to material elastic constants. $\varepsilon_{\parallel}$ is negative/positive when the pseudomorphic layer is under compressive/ tensile strain.

The shift of band edge levels caused by strain effects can be divided into two components, one of which is hydrostatic contribution and the other is shear contribution. The former push outward (pull inward) conduction and valence band edges from band gap center as the epi layer under compressive (tensile strain). The later splits energy levels of heavy hole and light hole bands at Γ point. Now conduction and valence band edges can be expressed as :

$$E_v = \text{VBO} + \Delta E_{vav}^{hy} + \max\left(\Delta E_{hh}^{sh}, \Delta E_{lh}^{sh}\right), \tag{2.1.7}$$

$$E_c = \text{VBO} + E_g + \Delta E_c^{hy}, \tag{2.1.8}$$

$$\text{VBO} = E_{vav} + \Delta_0/3. \tag{2.1.9}$$

where ΔE_{vav}^{hy} and ΔE_c^{hy} account for hydrostatic components,

$$\Delta E_{vav}^{hy} = a_v (2\varepsilon_{\parallel} + \varepsilon_{\perp}), \tag{2.1.10}$$

$$\Delta E_c^{hy} = a_c (2\varepsilon_{\parallel} + \varepsilon_{\perp}), \tag{2.1.11}$$

a_v/a_c refers to hydrostatic deformation potentials for conduction/valence bands. The $\max\left(\Delta E_{hh}^{sh}, \Delta E_{lh}^{sh}\right)$ in equation (2.1.7) means only select the maximum term between the ΔE_{hh}^{sh} and ΔE_{lh}^{sh}. The shear contribution couples to spin-orbit interaction and can be described below:

$$\Delta E_{hh}^{sh} = -b(\varepsilon_\perp - \varepsilon_{||}), \tag{2.1.12}$$

$$\Delta E_{lh}^{sh} = 1/2(-\Delta_0 + b(\varepsilon_\perp - \varepsilon_{||}) + \sqrt{\Delta_0^2 + 2\Delta_0 b(\varepsilon_\perp - \varepsilon_{||}) + 9b^2(\varepsilon_\perp - \varepsilon_{||})^2} \text{ [37]}, \tag{2.1.13}$$

where b is the tetragonal deformation potential.

Fig. 2.2 is depicted below for better understanding of strain effects induced energy shift of energy levels. In general, if pseudomorphic layer is biaxial compressive-strained, ΔE_{hh}^{sh} will be larger than ΔE_{lh}^{sh} and make heavy hole band shifted above light hole band. In the tensile-strained case $\Delta E_{lh}^{sh} > \Delta E_{hh}^{sh}$ and light hole is above heavy hole band.
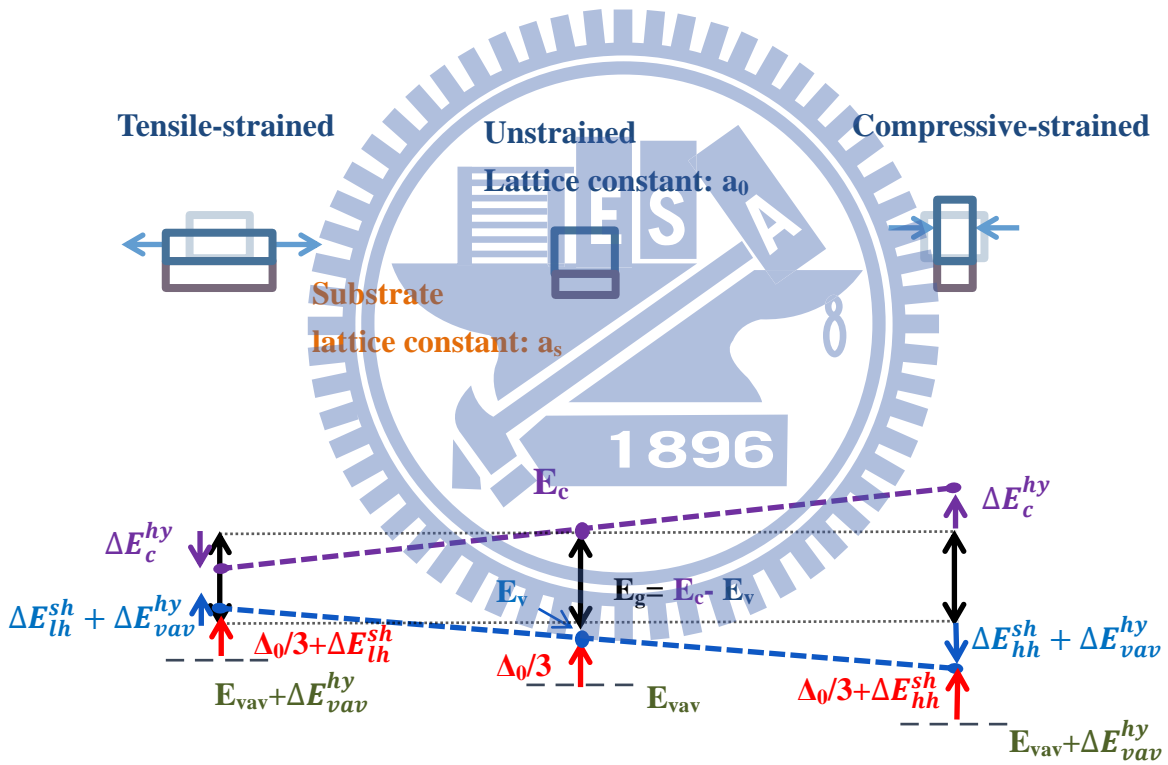
Fig 2.2 Strain effects induced band edge shifts for the three cases: tensile-strained, unstrained, and compressive-strained.

Band structure parameters for binary semiconductors of InAs, GaAs, and GaSb are listed in Table 2.2(a), including and which are used to empirically fit binary band gap as a function of temperature,

$$E_g(T) = E_g - \frac{\alpha T^2}{T + \beta}. \qquad (2.1.14)$$

Bowing parameters of InGaAs and GaAsSb ternary semiconductors are listed in Table 2.2(b).

These values of parameters are from the literature [4]. Other material parameters also can be

found there, while only most related InGaAs/GaAsSb ternaries are presented here. It is known

the material parameter values are varied among references and should be treated within a

certain range. However we use the exact values suggested by the literature without tuning,

because the purpose of our simulations, including the latter k.p calculations, is to study

overall tendency and characteristics of the "W" QWs as the structure parameters, such as

layer thickness and alloy composition, are varied and not intended to fully match with

experiment results. Fig. 2.3(a) and Fig. 2.3(b) show the calculation results of the amount of

band edge shifts for InGaAs and GaAsSb pseudomorphic layers on InP substrate caused by

varying indium fraction and antimonite fraction respectively. In order to see explicitly the

energy shifts of conduction band (CB) edge of InGaAs and valence band (VB) edge of

GaAsSb, their energy values have been reset to zero when they are lattice matched to InP

substrate. Notice that, CB edge of InGaAs drops as increasing indium fraction, while VB edge

of GaAsSb goes up as increasing antimony fraction. Either of them leads to decrease energy

difference between CB edge of InGaAs and VB edge of GaAsSb for InGaAs/GaAsSb

heterostructure, and hence helps to extend emission wavelength.

Table 2.2(a) Band structure parameters for binary semiconductors of InAs, GaAs, and GaSb.

	InAs	GaAs	GaSb
a_0 (Å)	6.058	5.653	6.096
E_g^Γ(eV)	0.417	1.519	0.812
α(meV/K)	0.276	0.5405	0.417
β(K)	93	204	140

VBO(eV)	-0.59	-0.8	-0.03
Δ_0(eV)	0.39	0.341	0.76
a_c(eV)	-5.08	-7.17	-7.5
a_v(eV)	1	1.16	0.8
b(eV)	-1.8	-2.0	-2.0
C_{11}(Gpa)	832.9	1221	884.2
C_{12}(Gpa)	452.6	566	402.6

Table 2.2(b) Bowing parameters for InGaAs and GaAsSb.

	InGaAs	GaAsSb
E_g^{Γ}(eV)	0.477	1.43
VBO(eV)	-0.38	-1.06
Δ_0(eV)	0.15	0.6
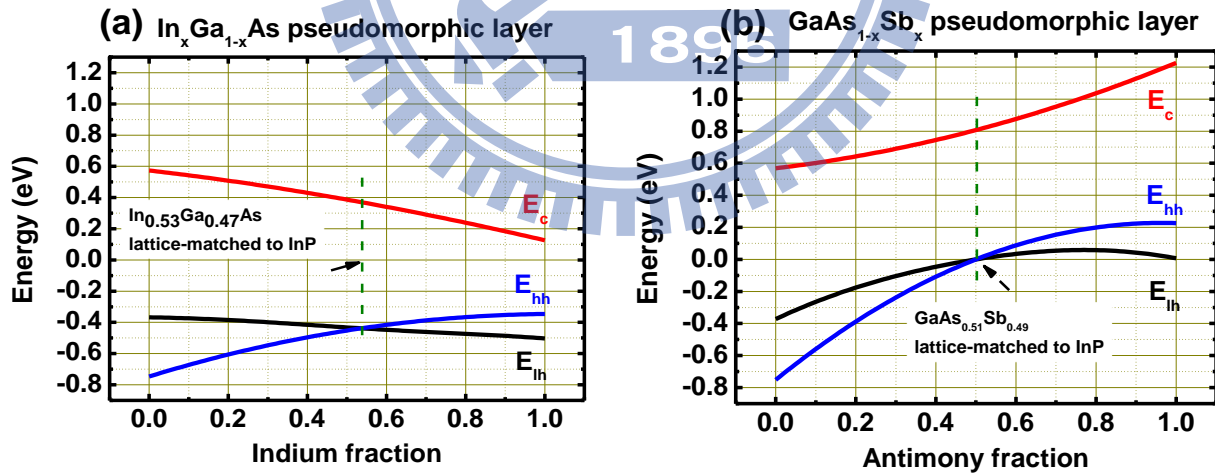
Fig. 2.3(a) Energy shifts of band edges, including conduction (E_c), heavy hole (E_{hh}), and light hole (E_{lh}) bands, vs. indium fraction for InGaAs pseudomorphic layer, and Fig. 2.3(b) those for GaAsSb pseudomorphic layer with varied antimony fraction on InP substrate.

A typical band alignment of the "W" type QW along with the electron and hole fundamental wavefunctions are shown in Fig. 2.4. The "W" structure mainly consists of symmetric InGaAs/GaAsSb/InGaAs layers sandwiched by InAlAs barrier layers. The structure gains the name from the "W"-like shape of conduction band profile. Because of the type-II band alignment, holes are confined inside the valence band (VB) of GaAsSb QW, forming heavy hole (HH) and light hole (LH) sub-bands, and electrons are confined in the two coupled InGaAs QWs, which have the split symmetric (E1) and the anti-symmetric (E2) states. The fundamental E1-HH1 optical transition has a smaller effective band gap energy not limited by the bandgaps of the constituent layers, and therefore gives a longer emission wavelength. The barrier layers provide quantum confinement for the electrons and increase the electron-hole wavefunction overlap, which leads to enhanced momentum matrix elements for optical device operation. Two dimensional densities of states for both carries are preserved in the "W" structure, and the type II configuration suppresses the Auger recombination.
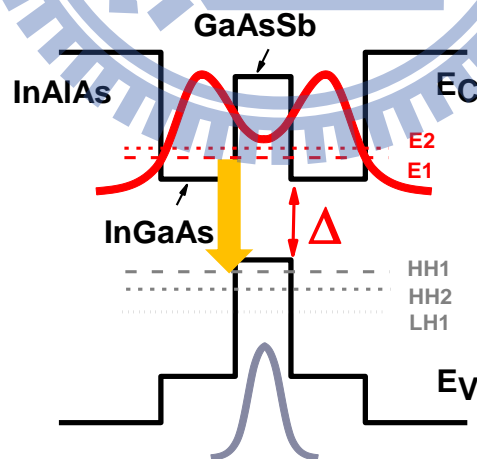
Fig. 2.4 A Scheme of a typical band alignment for the "W" type QW along with fundamental electron and hole wavefunctions based calculations of one band effective mass model.

Fig. 2.5 shows the relative position of the band edges of the materials used in the "W" QW,

including $In_{0.53}Ga_{0.47}As$ and $In_{0.52}Al_{0.48}As$ which are lattice matched to InP substrate, and The

Sb mole fraction in $GaAs_{1-x}Sb_x$ is varied from 0 to 1. The top horizontal axis indicates the

biaxial strain in the GaAsSb layer, which is assumed to be pseudomorphically grown with the

same in-plane lattice constant as InP. The plot of band edge energy shifts of GaAsSb are

calculated based on "model solid" theory same as Fig. 2.3(b) but takes an offset to meet

consistency with the band lineup for lattice matched case ($GaAs_{0.51}Sb_{0.49}$) depicted in Fig. 2.1.

The energy difference (Δ) between CB edge of $In_{0.53}Ga_{0.47}As$ and VB edge of GaAsSb shrinks

as the Sb fraction, x, increases. It is only around 0.25eV when x is 0.8. This energy

corresponds to a very respectable 4.96 μm mid-IR light emission (without adding the electron

and hole quantized energies). In next section, emission wavelength and wavefunction overlap

of "W" QWs with varied structure parameters, including thickness of InGaA and GaAsSb and

Sb fraction of GaAsSb, will be simulated by simple one band effective mass approximation.
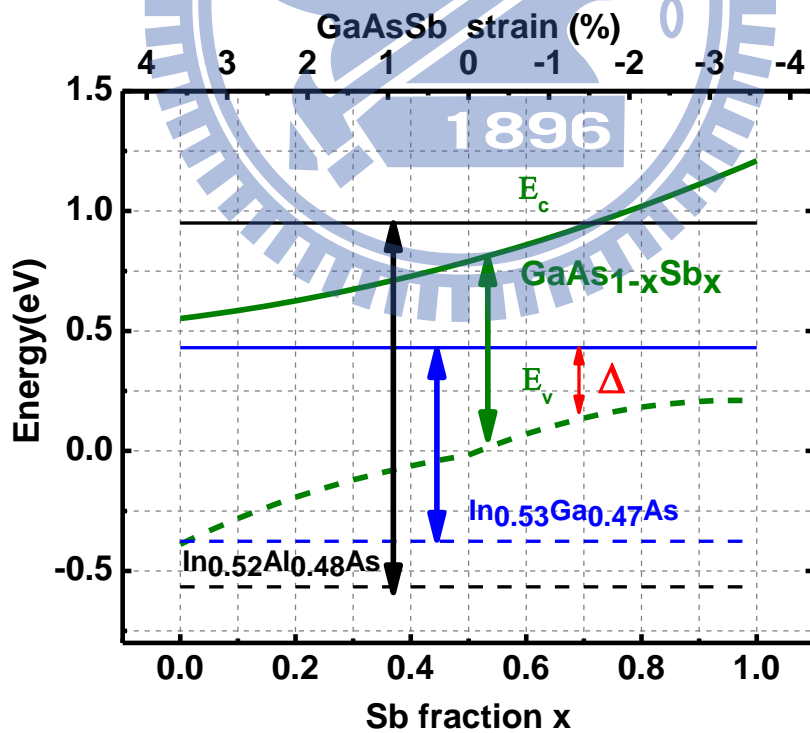
Fig. 2.5 Band edge energy levels (conduction band edge E_c denoted by solid line and valence band edge E_v by dashed line) of $In_{0.53}Ga_{0.47}As$ and $In_{0.52}Al_{0.48}As$ which are lattice matched to InP substrate, and $GaAs_{1-x}Sb_x$ pseudomorphic layer with Sb fraction varied from 0 to1. The biaxial strain is indicated on the top horizon axis. The band gap values for each material are indicated by the arrows. The Δ denotes the energy separation between the E_c of $In_{0.53}Ga_{0.47}As$ and the E_v of $In_{0.53}Ga_{0.47}As$

2.2 The tradeoff feature for the "W" type quantum well explored by one band effective mass approximation

One band effective mass approximation provides basic way to calculate quantized energy levels and wavefunction profile for quantum structure, which is time saving for computation so that it can be used to simulate cases with various structure parameters to reveal overall behaviors. Once knowing band alignment values of "W" structure in early section, electron and hole confinement energies are computed by solving one band Schrödinger wave equation with conduction band effective mass and valence band effective mass respectively. It also needs to fit proper boundary conditions for wavefunction across hetero interfaces described below.

Conduction band:
$$\frac{-\hbar^2}{2m_0} \nabla \frac{1}{m_c^*} \nabla \phi_e + E_c = E_{nc}\phi_e, \qquad (2.2.1)$$

Valence band:
$$\frac{-\hbar^2}{2m_0} \nabla \frac{1}{m_v^*} \nabla \phi_h + E_v = E_{mv}\phi_h, \qquad (2.2.2)$$

Boundary conditions:
$$\phi_{e,h}|_{hetero^+} = \phi_{e,h}|_{hetero^-} \qquad (2.2.3)$$

$$\frac{1}{m_{c,v}^*} \nabla \phi_{e,h}|_{hetero^+} = \frac{1}{m_{c,v}^*} \nabla \phi_{e,h}|_{hetero^-} \qquad (2.2.4)$$

Notations: m_0 : Free electron mass

m_c^*/m_v^* : Conduction band/valence band effective mass divided by m_0

ϕ_e/ϕ_h : Electron / hole wavefunction

E_c/E_v : Conduction/ valence band edge potential profile

E_{nc}/E_{mv} : Conduction/ valence band quantum confined levels

$\hbar$: Reduced plank constant

The effective mass values used for simulations are listed in Table 2.3. For simplicity, the effective mass for GaAsSb remains the same value without considering changes contributed

by strain effect and different composition. Calculations were performed with InGaAs and GaAsSb thickness varied from 2nm to 7 nm, and with Sb fraction of GaAsSb varied from 0.5 to 0.9. We used $In_{0.52}Al_{0.48}As$ as the barrier material in our "W" structure, which has a higher conduction band offset as compared to the (Ga)InP layer used in ref. 28 and the GaAsSb layer used in ref. 29. Our structure has a better electron confinement and a higher energy level when the same InGaAs width is used in the structure. In this parameter range, the ground state of valence band is always from heavy hole band because of the compressive strain of GaAsSb layer, which splits heavy hole band above light hole band, and the heavier effective mass of heavy hole as compared to light hole band makes the first heavy hole confined level more deeper. One can deduce the emission wavelengths of ground states optical transitions (E1 to HH1) and their corresponding electron-hole wavefunction overlaps. The square of wavefunction overlap is known to proportional to optical transition rate. Figure 2.6(a) shows the 3D contour plot for the three chosen wavelengths of 2μm, 2.5μm, and 3μm, where the x, y, and z axes are, in turn, values of the InGaAs layer width, GaAsSb layer width, and Sb mole fraction in GaAsSb. Figure 2.6(b) shows their corresponding wavefunction overlap square displayed in in grayscale, where the brightness increases with the magnitude. The maximum and minimum values in the plot are 0.261 and 0.015 respectively.

Table 2.3 The conduction and valence band effective mass values of ternaries used for simulations

	$In_{0.53}Ga_{0.47}As$	$In_{0.52}Al_{0.48}As$	$GaAs_{1-x}Sb_x$
m_c^*	0.043	0.075	0.047
m_v^*	-0.38	-0.34	-0.3

As shown in Fig. 2.6(a), wavelength can be tuned in the range from 2 to 3μm via modifying by varying the three parameters mentioned above. However, as the wavelength is increased

the wave function overlap decreases resulting in a smaller matrix element. A gradual increase in darkness in the plot is clearly seen as the wavelength changed from 2μm to 3μm in Fig. 2.6(b). This is a trade-off between the long wavelength emission and the optical matrix element and it is an intrinsic feature for the "W" type QW. The electron and hole are confined separately in different layers, the electron in the two coupled InGaAs layers and the hole in the GaAsSb layer, as shown in Fig. 2.4. Since the confinement potentials are large (~0.4eV) for both carriers, the quantization energies are decided by their own layer thickness; a thicker InGaAs or GaAsSb layer leads to a smaller electron or hole quantization energy and hence a longer emission wavelength. Although the increase of the InGaAs or GaAsSb layer thickness extends the emission wavelength, it also makes the electron and hole wave functions more concentrated in individual layers, and causes the reduction of electron-hole wavefunctions overlap. A similar trade-off exists when the Sb content in the GaAsSb layer is varied. The wavelength can be extended longer with a higher Sb content due to the reduced energy separation, Δ indicated in Fig 2.5, between the electron and the hole states. The raised conduction band edge, however, blocks the electron wave function penetration into the GaAsSb layer causing a reduction of the electron-hole wave function overlap. In order to a better elucidation, Fig. 2.7 (a) gives the wavefunctions at a chosen "W" structure indicated with values of ground state wavelength emission and overlap, and for comparisons, Fig. 2.7(b), Fig. 2.7 (c) ,and Fig. 2.7 (d) give the cases with each varying thickness of InGaAs, GaAsSb, and Sb fraction respectively.

As shown in Fig. 2.6(a), there are many possibilities in choosing the layer parameters to achieve the same emission wavelength. However, a different combination of the three parameters has a different strength in the transition matrix element. Looking carefully at Fig. 2.6(b), one can see that a better optical gain is generally obtained with a higher Sb mole fraction and thinner InGaAs/GaAsSb layers even for the same wavelength. Given such design

flexibility, one has to be careful, however, when using a high Sb content in the GaAsSb layer because the material quality may degrade.
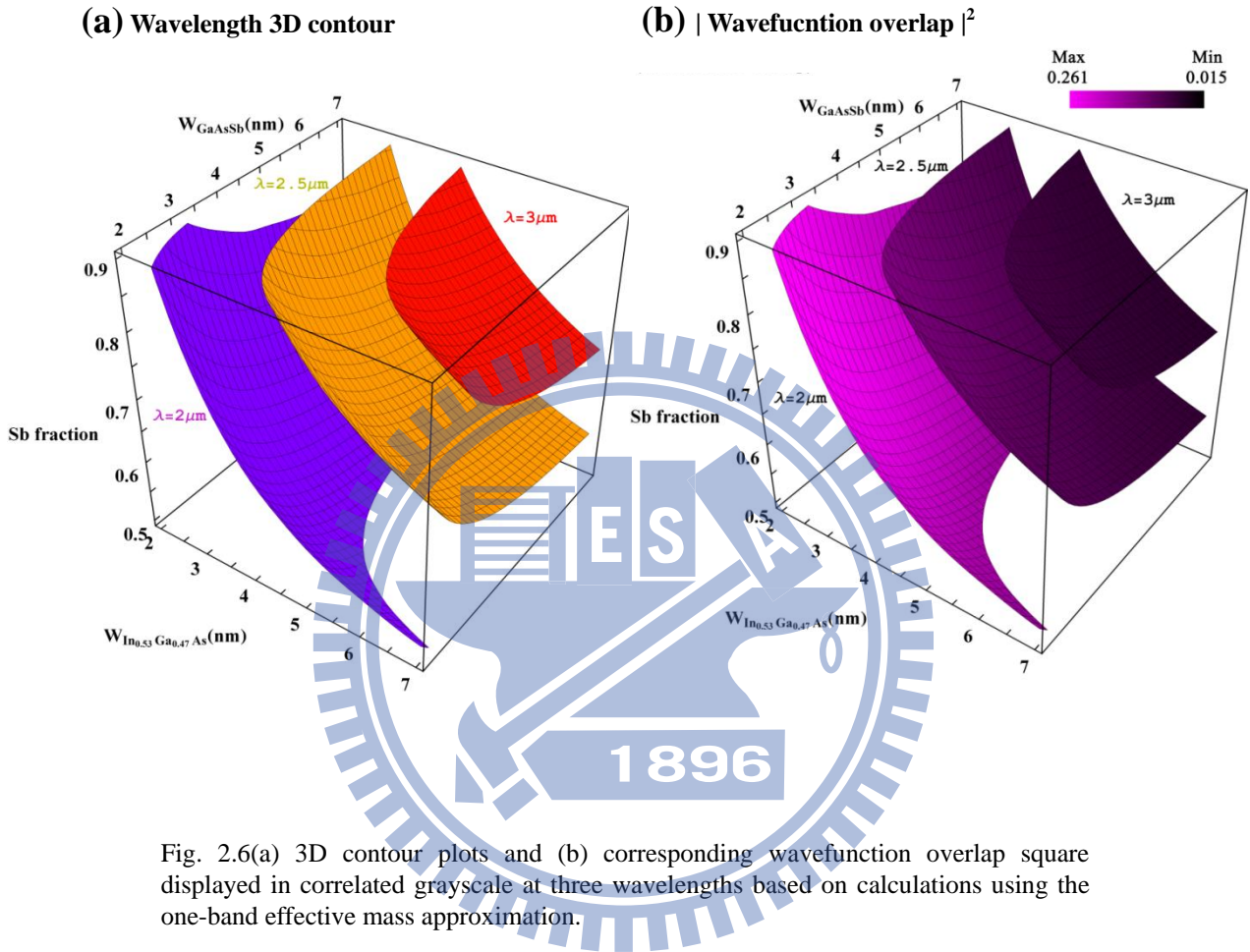
Fig. 2.6(a) 3D contour plots and (b) corresponding wavefunction overlap square displayed in correlated grayscale at three wavelengths based on calculations using the one-band effective mass approximation.
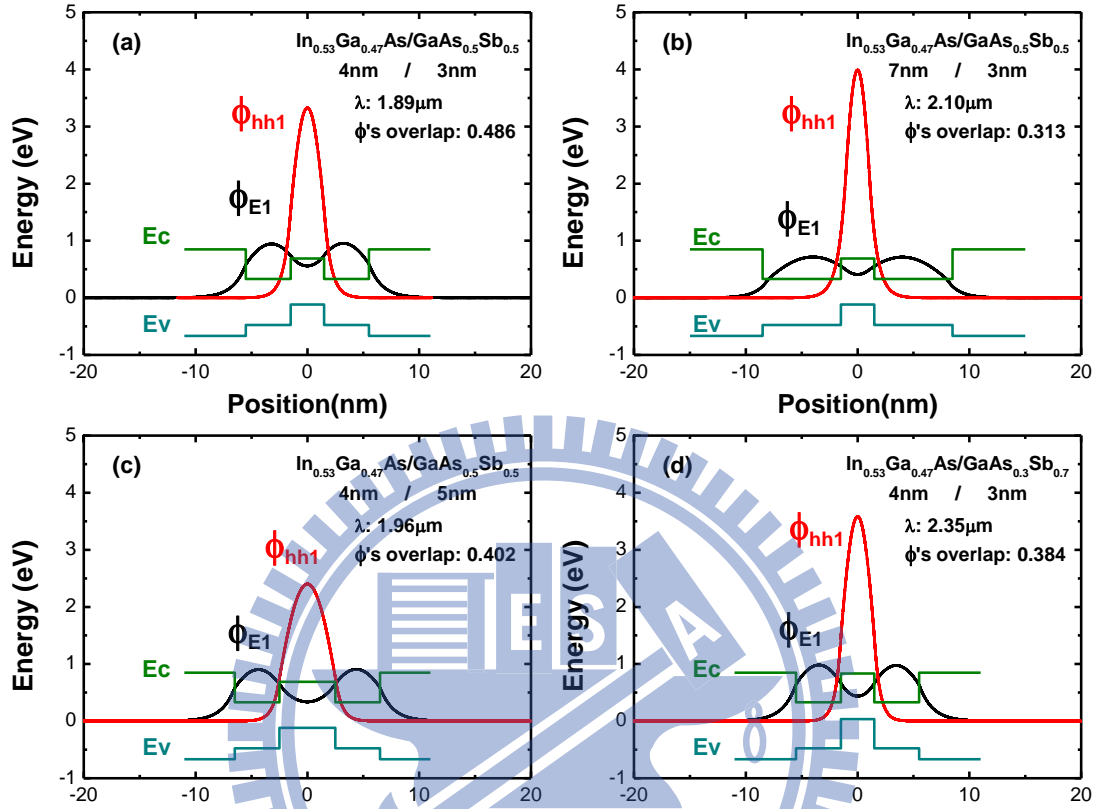
Fig. 2.7(a) The band diagram and calculation results of wavefunctions for a chosen "W" structure, indicated with values of structure parameters, emission wavelength, and electron-hole wavefunction overlap. For comparison, (b), (c), and (d) are results with increased thickness of InGaAs, GaAsSb, and Sb fraction of GaAsSb respectively. By comparing to (a), each shows a trade-off behavior, Extending wavelength accompanying with the reduction of wavefunction overlap.

2.3 Energy band dispersion relations and material gain simulations of "W" quantum wells based on the eight band $k.p$ theory

The $k.p$ theory has been widely used to simulation semiconductors energy dispersions and momentum matrix elements [38], which cannot be provided by the previous one band calculations. It includes minimum number of parameters deduced from the group theoretical treatment as in a high symmetric point at Brillouin zone (BZ). The parameter set can be experimentally determined to truly reflect the band structure. The theory works well at vicinity of band extreme, where the most cared place for the optoelectronics consideration.

The Schrödinger equation incorporated spin-orbit interaction for one electron in a bulk semiconductor material can be described as

$$\widehat{H}\psi(\mathbf{r}) = \left[\frac{-\hbar^2}{2m_0} \nabla^2 + V(\mathbf{r}) + \frac{\hbar}{4m_0^2 c^2} \boldsymbol{\sigma} \cdot (\nabla V \times \mathbf{p}) \right] \psi(\mathbf{r}) = E(\boldsymbol{k})\psi(\mathbf{r}), \quad (2.3.1)$$

where the σ is the Pauli spin matrix. Based on Bloch's theorem, the electronic wavefunctions in a periodic potential follows the form:

$$\psi(\mathbf{r}) = e^{i\boldsymbol{k}\cdot\boldsymbol{r}} * U_{n\boldsymbol{k}}(\boldsymbol{r}), \quad (2.3.2)$$

which is a slowly varying plane wave, with a wave vector $\boldsymbol{k}$, times a fast changing cell-periodic Bloch's function, with a n referring to different bands. In a zinc blende crystal, by taking the Bloch bases in turns of S↑, X↑,Y↑, Z↑, S↓, X↓, Y↓, Z↓, which are spin up and down of anti-bonding S-like atomic orbital and three degenerate bonding P-like symmetry states at Γ(k=0) point respectively, the $\boldsymbol{k.p}$ Hamiltonian can be written down as

$$\widehat{H} = \begin{pmatrix} \widehat{H}_4 & 0 \\ 0 & \widehat{H}_4 \end{pmatrix} + \widehat{H}_{so} + \widehat{H}_\varepsilon \quad [39, 40]. \quad (2.3.3)$$

Here Löwdin perturbation theorem has been used to set conduction band, heavy hole, light hole, and split-off band as Class A group, and other remote bands as Class B group. Then the $\widehat{H}_4$ is 4 x 4 block k related Hamiltonian expressed as

$$\widehat{H}_4 = \begin{pmatrix} \widehat{H}_{cc} & \widehat{H}_{cv} \\ \widehat{H}_{vc} & \widehat{H}_{vv} \end{pmatrix}. \tag{2.3.4}$$

$\widehat{H}_{cc}$ is the scalar

$$\widehat{H}_{cc} = E_c + \sum_{i=x,y,z} \hat{k}_i A_c \hat{k}_i, \tag{2.3.5}$$

where Ec is the conduction band edge, Ac include the influence of remote bands on the electron effective mass and can be described as

$$A_c = \frac{\hbar^2}{2m_0 m_c^*} - \frac{2P^2}{3E_g} - \frac{P^2}{3(E_g + \Delta)}. \tag{2.3.6}$$

Here P is related to the interband momentum matrix element :

$$P = \frac{\hbar}{im_0} < S|\hat{p}_x|x >, \tag{2.3.7}$$

which is often related to the parameter Ep with a dimension of energy,

$$E_p = \frac{2m_0 P^2}{\hbar^2}. \tag{2.3.8}$$

$\widehat{H}_{cv}$ is the 1 x 3 matrix and equals to $\widehat{H}^\dagger{}_{vc}$,

$$\widehat{H}_{cv} = \widehat{H}^\dagger{}_{vc} = \begin{pmatrix} iP\hat{k}_x & iP\hat{k}_y & iP\hat{k}_z \end{pmatrix}. \tag{2.3.9}$$

$\widehat{H}_{vv}$ is the 3 x 3 matrix,

$$\widehat{H}_{vv} = \begin{pmatrix} \widehat{H}_{xx} & \widehat{H}_{xy} & \widehat{H}_{xz} \\ \widehat{H}_{yx} & \widehat{H}_{yy} & \widehat{H}_{yx} \\ \widehat{H}_{zx} & \widehat{H}_{zy} & \widehat{H}_{zz} \end{pmatrix}, \tag{2.3.10}$$

where typical diagonal and off-diagonal terms are given by

$$\widehat{H}_{xx} = E_v - \frac{\Delta}{3} + \hat{k}_x L \hat{k}_x + \hat{k}_y M \hat{k}_y + \hat{k}_y M \hat{k}_y \tag{2.3.11}$$

$$\widehat{H}_{xy} = \hat{k}_x N_+ \hat{k}_y + \hat{k}_y N_- \hat{k}_x. \tag{2.3.12}$$

Other elements can be derived by cyclically permuting x, y, and z notes. The parameters of L, M, N_+, and N_- are described as

$$L = \frac{-\hbar^2}{2m_0}(\gamma_1 + 4\gamma_2), \tag{2.3.13}$$

$$M = \frac{-\hbar^2}{2m_0}(\gamma_1 - 2\gamma_2), \tag{2.3.14}$$

$$N_- = M - \frac{\hbar^2}{2m_0}, \tag{2.3.15}$$

$$N_+ = \frac{-\hbar^2}{2m_0}(6\gamma_3) - N_-. \tag{2.3.16}$$

Because it is an eight band Hamiltonian, the γ_1, γ_2, and γ_3 now are modified Luttinger parameters with taking the effect of conduction band into account and can be given by

$$\gamma_1 = \gamma_1^L - \frac{E_p}{3E_g}, \tag{2.3.17}$$

$$\gamma_2 = \gamma_2^L - \frac{E_p}{6E_g}, \tag{2.3.18}$$

$$\gamma_3 = \gamma_3^L - \frac{E_p}{6E_g}, \tag{2.3.19}$$

where Luttinger parameters γ_1^L and γ_2^L describe the coupling of valence band states to higher bands, and γ_3^L describe anisotropy. $\widehat{H}_{so}$ is the spin-orbit Hamiltonian as

$$\widehat{H}_{so} = -\frac{\Delta}{3} \times \begin{pmatrix} 0 & 0 & 0 & 0 & 0 & 0 & 0 & 0 \\ 0 & 0 & i & 0 & 0 & 0 & 0 & -1 \\ 0 & -i & 0 & 0 & 0 & 0 & 0 & i \\ 0 & 0 & 0 & 0 & 0 & 1 & -i & 0 \\ 0 & 0 & 0 & 0 & 0 & 0 & 0 & 0 \\ 0 & 0 & 0 & 1 & 0 & 0 & -i & 0 \\ 0 & 0 & 0 & i & 0 & i & 0 & 0 \\ 0 & -1 & -i & 0 & 0 & 0 & 0 & 0 \end{pmatrix}.$$

(2.3.20)

$\widehat{H}_\varepsilon$ is added to describe the strain effect on electronic band structure expressed as

$$\widehat{H}_\varepsilon = \begin{pmatrix} \widehat{H}_{\varepsilon 0} & 0 \\ 0 & \widehat{H}_{\varepsilon 0} \end{pmatrix}.$$

(2.3.21)

$\widehat{H}_{\varepsilon 0}$ is the 4 x 4 block included with strain tensor components ε_{ij}

$$\widehat{H}_{\varepsilon 0} = \begin{pmatrix} a_c \varepsilon & 0 & 0 & 0 \\ 0 & h_{xx} & n\varepsilon_{xy} & n\varepsilon_{xz} \\ 0 & n\varepsilon_{yx} & h_{yy} & n\varepsilon_{yz} \\ 0 & n\varepsilon_{zx} & n\varepsilon_{zy} & h_{zz} \end{pmatrix},$$

(2.3.22)

where a_c is conduction band deformation potential as described in early section, and

$$\varepsilon = \varepsilon_{xx} + \varepsilon_{yy} + \varepsilon_{zz},$$

(2.3.23)

$$h_{xx} = l\varepsilon_{xx} + m(\varepsilon_{yy} + \varepsilon_{zz}),$$

(2.3.24)

Other terms are given by cyclic permutations of x, y, and z. The parameters of l, m, and n

relate to valence band deformation potentials as the following.

$$l = -a_v + 2b,$$

(2.3.25)

$$m = -a_v - b,$$

(2.3.26)

$$n = \sqrt{3}d.$$

(2.3.27)

$$\varepsilon_{xx} = \varepsilon_{yy} = \frac{a_0}{a} - 1,$$

$$(2.3.28)$$

$$\varepsilon_{zz} = -\frac{2C_{12}}{C_{11}}\varepsilon_{xx},$$

$$(2.3.29)$$

$$\varepsilon_{xy} = \varepsilon_{xz} = \varepsilon_{yx} = \varepsilon_{yz} = \varepsilon_{zx} = \varepsilon_{zy} = 0.$$

$$(2.3.30)$$

a_0 and a refer to lattice constants of substrate and pseudomorphic layer respectively. Here only hydrostatics' strains have been considered, so except the diagonal terms of $\hat{H}_{\varepsilon 0}$ exist, other terms are zero.

When dealing with quantum wells or multilayer structure, all the $\hat{k}_z$ terms in the above 8-band Hamiltonian need to be replaced by the operator $-i\partial/\partial z$. Here epi-layer is grown along the (001) direction which is defined as z axis, while the (100) and (010) directions are defined as x axis and y axis respectively. Now the parameters become z dependent such as Ac(z), Ec(z), Ev(z), L(z), M(z), and ε(z), etc. The electron wavefunction can be expressed as the following form:

$$\psi = \sum_{j}^{class\ A} F_j u_j,$$

$$(2.3.31)$$

where F_j is so called the envelope function. By taking the same Bloch bases, it tries to find eight coupled equations:

$$\sum_{j=1}^{8} \hat{H}_{ij} F_j = E F_i,$$

$$(2.3.32)$$

where E is the electron energy level and $i = 1, 2 \dots, 8$. The envelope function can be further expanded by a set orthonormal basis. Since quantum well is confined in z direction, the envelope function will be vanishes in a certain distance from the well and it remains free in

x-y direction. The M series of z dependent Sin functions are chosen for the bases while plane waves are set for the other two directions. The expanded envelope function can be described as

$$F_j(\mathbf{r}) = \sqrt{\frac{2}{V}} \, e^{i(k_x x + k_y y)} \sum_{m=1}^{M} C_m^j \, \mathrm{Sin}\left(\frac{m\pi}{L} z\right), \tag{2.3.33}$$

where L is the properly chosen boundary width and $\sqrt{\frac{2}{V}}$ is a normalization constant. Since it adapts extra M bases, now every element in the origin $\hat{H}_{ij}$ expands into M x M block. The full Hamiltonian can be rewritten to an 8M x 8M matrix as the form:

$$\sum_{j}^{8} \sum_{m}^{M} H_{(i-1)M+n,(j-1)M+m}^{F} C_m^j = E C_n^i, \tag{2.3.34}$$

where i=1,2,…,8 and n=1,2,…,M. The matrix element is given by

$$H_{(i-1)M+n,(j-1)M+m}^{F} = \frac{2}{L} \int_0^L \sin\left(\frac{n\pi}{L} z\right) \hat{H}_{ij} \sin\left(\frac{m\pi}{L} z\right) dz. \tag{2.3.35}$$

By solving this eigen system, energy dispersions of electron quantized levels with different in-plane wave vector (kx and ky) can be derived from eigen values. The corresponding envelope function possibility distribution can be found by the absolute magnitude of the superposition of bases functions with eigen vectors as coefficients.

The functions used to calculate parameter values of ternary alloys with different composition are presented in Table 2.4, which are derived by either a linear interpolation from values of constituent binaries or that modified with a quadratic term due to a bowing parameter[4]. The parameters listed in Table 2.4 are with temperature at 300 K. Temperature dependence of band gap (Eg) and lattice constant (a) are provided in Table 2.5, conduction band edge (Ec) also changed by Ec=Eg+Ev, while other parameters are treated as invariable with temperature.

Three cases of "W" quantum wells are calculated, which all consist of $In_{0.52}Al_{0.48}As/In_{0.53}Ga_{0.47}As/GaAs_{1-x}Sb_x/In_{0.53}Ga_{0.47}As/$ $In_{0.52}Al_{0.48}As$ with thicknesses of 92/4/3/4/92 nm but with Sb fraction in turns of 0.5, 0.7, and 0.9 in GaAsSb. The simulations are used 125 Sin function series, so the full Hamiltonian is a 1000 x 1000 block, which is programmed and solved by using the Matlab software. The total boundary width (L) is 205nm, which is large enough to ensure the wavefunction of the "W" well diminishes at the boundary points. The results of E-k relations at temperature of 300K are shown in Fig. 2.8(a), Fig. 2.8(b) and Fig. 2.8(c) for the three cases. The two CB sub-bands, C1 and C2, corresponding to the symmetrical and anti-symmetrical states of the two coupled electron QWs and the HH1, LH1 and HH2 sub-bands in the VB are shown. The band offsets of the type-II GaAsSb/InGaAs heterojunction and the values of the effective band gap (C1-HH1), the energy separations of C1-C2 and HH1-LH1, the effective masses of C1 electrons and HH1 heavy holes at the zone center are listed together in Table 2.6 for the three cases.
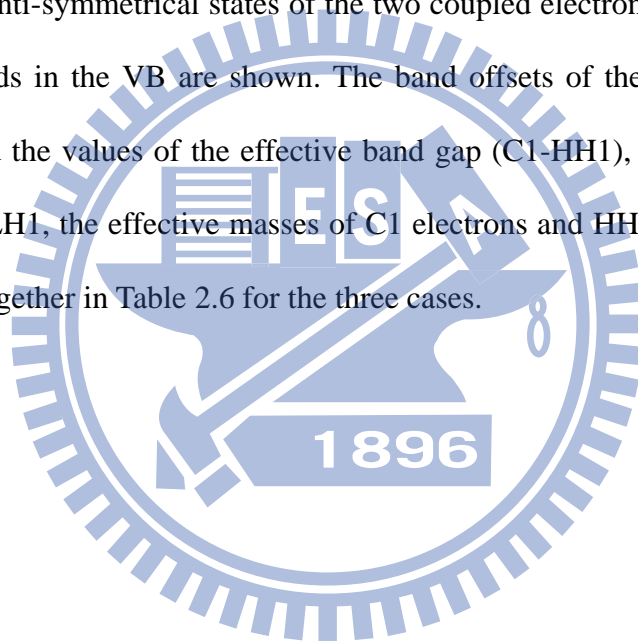
Table 2.4 The parameters of the constituent materials in the "W" QW used for the $k.p$ calculations.

T= 300 K	In$_{0.52}$Al$_{0.48}$As	In$_{0.53}$Ga$_{0.47}$As	GaAs$_x$Sb$_{1-x}$
E_g(eV)	1.45	0.74	$0.812-0.723x+1.43x^2$
E_v(eV)	0	0.19	$0.678+0.29x-1.06x^2$
E_c(eV)	1.45	0.93	$1.49-0.433x+0.37x^2$
Δ(eV)	0.30	0.33	$0.76-1.019x+0.6x^2$
g$_{1(Luttinger)}$	12.20	13.88	$14.5-7.52x$
g$_{2(Luttinger)}$	4.81	5.47	$3-0.94x$
g$_{3(Luttinger)}$	5.47	6.25	$6-307x$
E_p(eV)	21.31	24.93	$27+1.8x$
a(Å)	5.87	5.87	$6.096-0.443x$
C11(Gpa)	1033.1	1015.3	$884.2+336.8x$
C12(Gpa)	278.1	505.9	$402.6+163.4x$
a_c(eV)	-5.35	-3.63	$-7.5+5.5x$
a_v(eV)	-1.71	-3.90	$-0.8-6.37x$
b(eV)	-2.04	-1.50	$-2+0.84x$
d(eV)	-3.50	-4.16	$-4.7-0.1x$

Table 2.5 The temperature dependences of band gaps and lattice constants for the three alloys.

$In_xAl_{1-x}As$	Eg(eV)	$x\left(0.417 - \frac{0.276\times10^{-3}T^2}{T+93}\right) + (1-x)\left(3.099 - \frac{0.885\times10^{-3}T^2}{T+530}\right) - x(1-x)0.7$
	a (Å)	$x(6.058 + 2.74\times10^{-5}(T-300)) + (1-x)(5.661 + 2.9\times10^{-5}(T-300))$
$In_xGa_{1-x}As$	Eg(eV)	$x\left(0.417 - \frac{0.276\times10^{-3}T^2}{T+93}\right) + (1-x)\left(1.519 - \frac{0.54\times10^{-3}T^2}{T+204}\right) - x(1-x)0.477$
	a (Å)	$x(6.058 + 2.74\times10^{-5}(T-300)) + (1-x)(5.6533 + 3.88\times10^{-5}(T-300))$
$GaAs_xSb_{1-x}$	Eg(eV)	$x\left(1.519 - \frac{0.54\times10^{-3}T^2}{T+204}\right) + (1-x)\left(0.812 - \frac{0.417\times10^{-3}T^2}{T+140}\right) - x(1-x)1.43$
	a (Å)	$x(5.6533 + 3.88\times10^{-5}(T-300)) + (1-x)(6.096 + 4.72\times10^{-5}(T-300))$

Table 2.6 The $\Delta E_c/\Delta E_v$ band offsets of GaAsSb/InGaAs type-II heterostructure and the extracted values of effective band gap, the energy differences of C1-C2 and HH1-LH1, and the C1 electron /HH1 hole effective masses at zone center for the three cases.

Sb fraction	0.5	0.7	0.9
$\Delta E_c/\Delta E_v$ (meV)	0.36/0.36	0.52/0.51	0.68/0.58
Effective E_g (meV)	597.1	515.8	461.3
ΔC1-C2 (meV)	35.2	14.7	7.0
ΔHH1-LH1 (meV)	123.7	183.6	235.3
Effective m_e for C1 (m_0)	0.062	0.069	0.073
Effective m_h for HH1(m_0)	-0.105	-0.098	-0.093
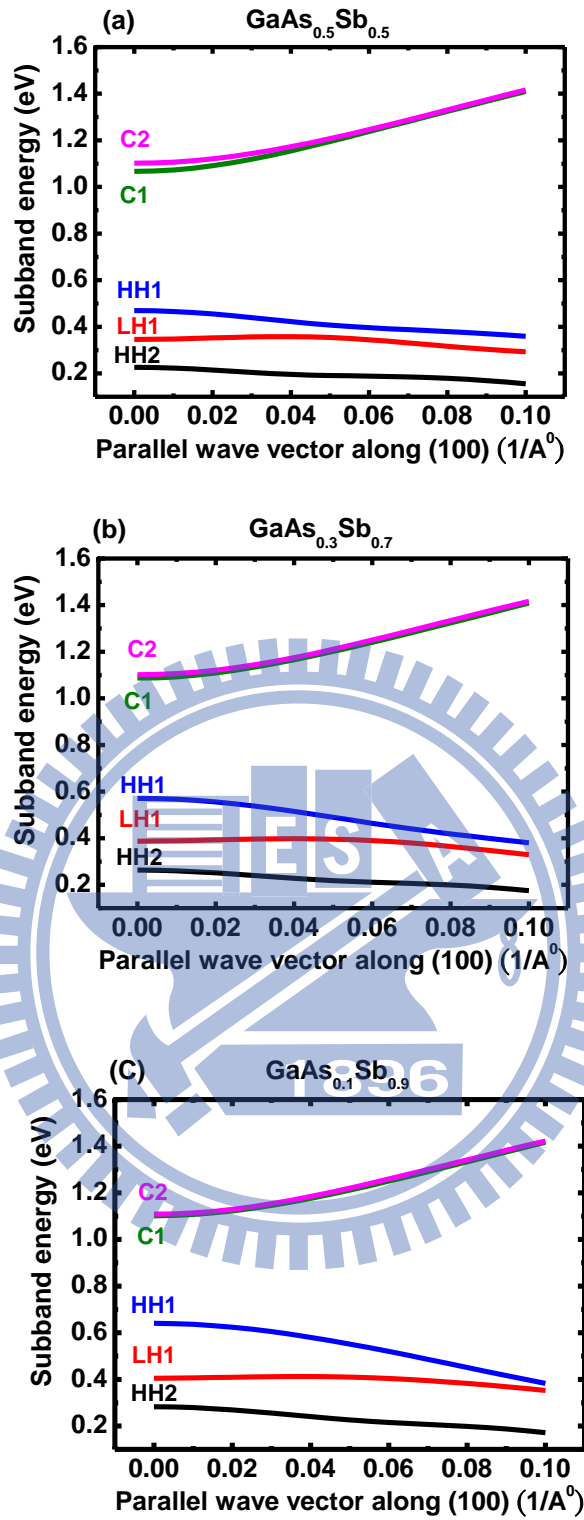
Fig. 2.8 The energy dispersion of the "W" QW consisting of $In_{0.53}Ga_{0.47}As/GaAs_{1-x}Sb_x/In_{0.53}Ga_{0.47}As$ (4/3/4nm) sandwiched between $In_{0.52}Al_{0.48}As$ barrier layers for the three cases with different Sb fraction: (a) $x_{sb}= 0.5$, (b) $x_{sb}=0.7$, and (c) $x_{sb}=0.9$, where C1 and C2 refer to the symmetric and the anti-symmetric conduction subbands, HH1 and HH2 refer to the first and the second confined heavy hole subbands, and LH1 refers to the first confined light hole subband.

As seen in Table 2.6, the effective band gap decreases from 597.1meV to 461.3meV as the Sb fraction increases from 0.5 to 0.9, which is caused by the raised valence band edge of the GaAsSb pseudomorphic layer. The increased valence band offset at the InGaAs/GaAsSb junction also leads to the increase of hole subband energy separation. The Δ(HH1-LH1) values increases from 123.7 to 235.3 meV. However, the conduction subband splitting Δ(C1-C2) decreases from 35.2 to 7.0 meV. The reason comes from the raised conduction band edge of GaAsSb pseudomorphic layer causing the two InGaAs electron QWs less coupled to each other. The higher the Sb fraction, the more compressively strained is within the GaAsSb layer. This shapes the energy dispersion and leads to the reduction of the HH1 effective mass from $0.105m_0$ to $0.093m_0$ as presented in Table 2.6. More balanced effective masses between electron and hole have been known to benefit laser operation, which can be archived by introducing a proper compressive strain in the hole QW.

The optical momentum matrix elements ($\hat{e} \cdot P_{nm}^{\eta\sigma}$) are expressed as the following:

$$\hat{e} \cdot p_{nm}^{\eta\sigma} = <\Psi_n^\eta | \hat{e} \cdot p | \Psi_m^\sigma > = \sum_{i,j} < F_j^{n\eta} u_j | \hat{e} \cdot p | F_i^{m\sigma} u_i >, \quad (2.3.36)$$

where n and m represent high and low energy levels, η and σ stand for spin notations, **p** is momentum operator, and ê states polarization directions. The calculation can be approximated by taking the material parameter dependent value of $<u_j | \hat{e} \cdot p | u_i>$, which relates to the parameter P, integrated with the relatively slow varying envelope functions along z axis. The optical transition mainly takes place between C1 and HH1, because holes are mostly populated in the HH1 band due to the large HH1-LH1 energy separation. The transition between HH1 and C2 is forbidden due to different the parity in the envelop wave functions. Fig. 2.9(a)-(c) show the square of matrix elements of HH1-C1 transition for the three cases, where TE polarization is with an in-plane optical electric field ($\hat{e} = \hat{x} \, or \, \hat{y}$) and TM polarization is with an optical electric field normal to plane ($\hat{e} = \hat{z}$). It can be seen that the

HH1-C1 transition only contributes to TE polarization near zone center. The matrix element decreases as the in-plane wave vector moves away from the zone center. The TM component of the matrix elements rises at around the midway in the Brillouin zone where the HH1 and LH1 bands are mixed. Comparing the three cases, it is obvious that the matrix element reduces as the Sb mole fraction is increased.
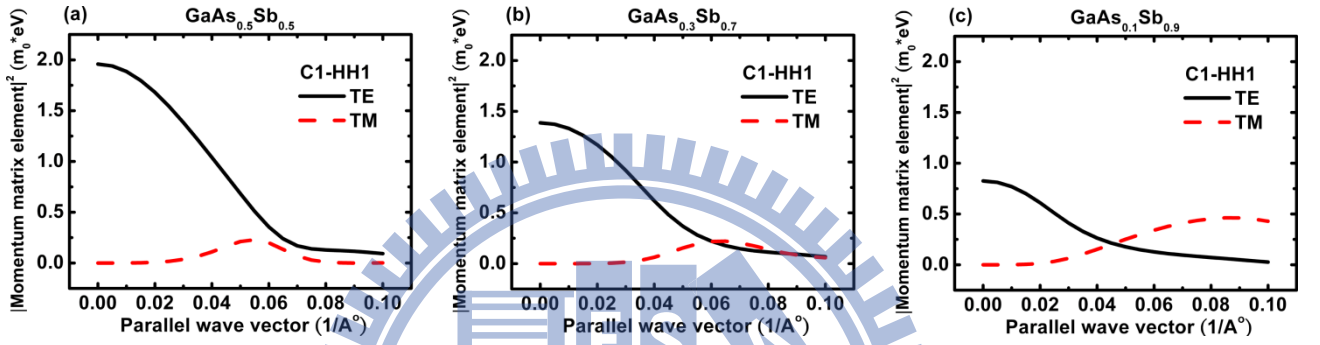
Fig. 2.9 The squared momentum matrix element of the C1-HH1 transition for the three cases: (a) x_{sb}= 0.5, (b) x_{sb}=0.7, and (c) x_{sb}=0.9.

Material gain can be calculated by

$$g(\hbar\omega) = \frac{\pi e^2}{n_r c \varepsilon_0 m_0^2 \omega} \frac{1}{L_z} \sum_{\eta,\sigma} \sum_{n,m} \int |\hat{e} \cdot P_{nm}^{\eta\sigma}|^2 \frac{\Gamma/(2\pi)}{[E_{hm}^{en}(k_t) - \hbar\omega]^2 + (\Gamma/2)^2} (f^{\eta n} - f^{\sigma m}) \frac{k_t \, dk_t}{2\pi},$$

(2.3.37)

with the following parameter notations:

n_r : refraction index;
m_0 : free electron mass;
ε_0 : permittivity in free space;
c : light velocity;
L_z : QW thickness;

36

$|\hat{e} \cdot P_{nm}^{\eta\sigma}|^2$: *squared momentum matrix element,*

  $\hat{e}$ *is the electric field polarization vector;*

E_{hm}^{en} : *electron − hole transition energy;*

$\hbar\omega$: *photon energy;*

η, σ : *spin notation;*

n, m : *conduction, valence subbands;*

k_t : *parallel wave vector;*

Γ : *linewidth of Lorenzian broadening;*

f : *Fermi − Dirac distribution.*

Fig. 2.10 shows the results of TE material gain as a function of transition energy for the three cases. 2D carrier densities of 1×10^{12}, 2×10^{12}, and 3×10^{12} cm^{-2} were used in the calculation. Fig. 2.11 shows the peak gain as a function of 2D carrier density. Here we have used a line broadening factor, Γ, of 20meV and a "W" QW thickness, Lz, of 11nm in the calculations.
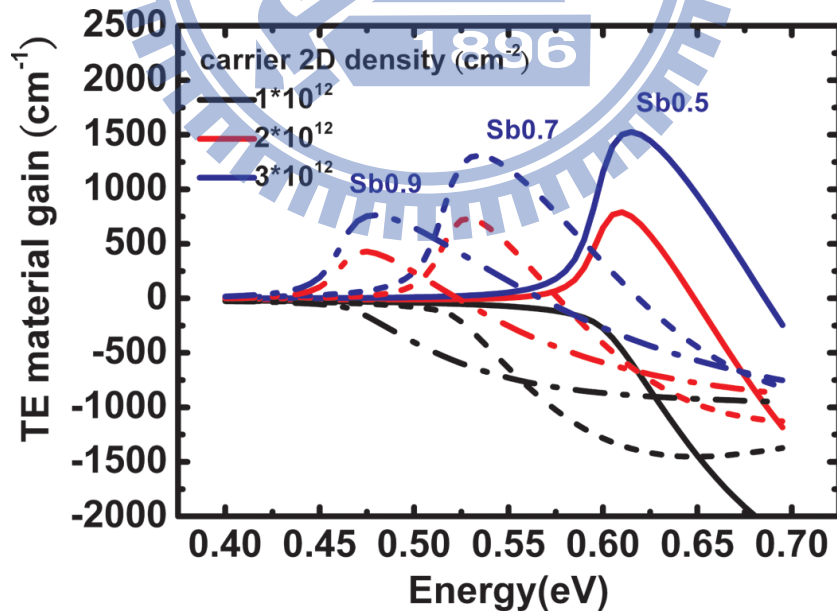
Fig. 2.10 The calculated TE material gain spectra for the three cases with 2D carrier densities of 1×10^{12}, 2×10^{12}, and 3×10^{12} cm^{-2}.
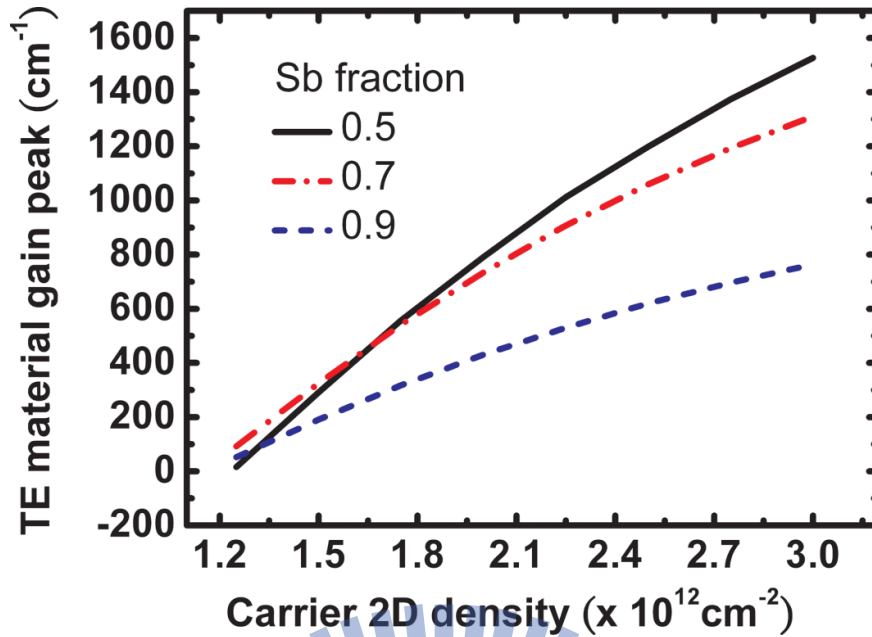
Fig. 2.11 The TE material gain peak value as function of carrier 2D density for the three cases.

As displayed in the gain spectra shown in Fig. 2.9, the gain increases and the spectrum broadens as more carriers are injected into the well. Except for the case with $x_{Sb} = 0.9$, the peak gain of the other two ($x_{Sb} = 0.5, 0.7$) can all go beyond 10^3 cm^{-1} with a 2D carrier density of 3×10^{12} cm^{-2}. For InP-based type-I compressively strained InGaAs/InGaAsP QWs in near-IR 1.5μm lasers, lower 2D carrier density values around $1.2\text{-}1.6 \times 10^{12}$ cm^{-2} are needed to get gain values over 10^3 cm^{-1}, which is mainly due to the better wave function overlap than "W" type QWs [41, 42]. However such gain and carrier density for "W" type QWs are in general sufficient to satisfy the requirements for the operation of mid-IR lasers. It should be mentioned that the calculation presented above was for only one "W" QW. If needed (such when $x_{Sb} = 0.9$), multiple QWs can be used to boost the gain.

Looking at Fig. 2.10 and Fig. 2.8 carefully, we notice that the reduction in gain as the Sb mole fraction is increased (especially from $x_{Sb} = 0.5$ to 0.7) is not in proportion to the reduction in the magnitude of the matrix element. When the 2D carrier density is below $\sim 1.7 \times 10^{12}$ cm^{-2}, the peak gain for the case with $x_{Sb} = 0.7$ is even superior to that of the $x_{Sb} = 0.5$ case. This is due to the reduced HH1 effective mass caused by the increased compressive

strain in the GaAsSb layer when a higher Sb mole fraction is used. The upward electron energy band dispersion is than more symmetric to the downward hole energy band dispersion, and it generates a larger value of $(f^{\eta n} - f^{\sigma m})$ as they accumulating carriers. The more balanced electron/hole effective masses cause the transparency carrier density to drop and the gain to rise.

By introducing a proper compressive strain via increasing Sb fraction in GaAsSb layer, the "W" QW material gain can be increased while the optical wavelength is also extended. It can benefit mid-IR lasers and therefore can be incorporated into design principles.

2.4 Summary

We have theoretically investigated the InP based InGaAs/GaAsSb "W" type QWs for mid-IR light sources and lasers. The trade-off between the emission wavelength and the momentum matrix element is studied in the 2μm to 3μm range. At a given wavelength, the design with thinner InGaAs and GaAsSb layers and a higher Sb content in GaAsSb is more desirable because of a larger matrix element. Calculations are based on the eight band *k.p* theory and proceed by the basis expansion of the envelope function. Besides the emission wavelength and the matrix element, the strain in the GaAsSb layer also plays an important role in the determination of the material gain. The enhanced compressive strain in the GaAsSb layer when a high Sb content is used can reduce the transparency carrier density and increase the gain. So the benefit of a more balanced electron/hole effective masses can partial compensate the gain loss caused by the reduced matrix element caused by the higher Sb content. With a proper design, the material gain of a single "W" QW is able to reach above 10^3 cm^{-1} with a 2D carrier density of 3×10^{12} cm^{-2}. The result presented in this work shows that the InP based "W" type QWs are suitable for mid-IR lasers and it provides a guideline for the design of such complex structure.

Chapter 3

Experiment techniques

This chapter presents the experiment techniques that needed to carry out the overall research. It includes molecular beam epitaxy (MBE) for samples growth, X-ray for material characterization, photoluminescence for optical spectrum studies, and finally the optically pumping setup for demonstration of lasing phenomenon and analysis of the "W" type mid-IR lasers.

3.1 Molecular beam epitaxy

Our molecular beam epitaxy (MBE) apparatus comprises of two linked VEECO (or Varian) MBE systems, Fig 3.1 showing the front view. One is the GEN-II type on left hand side (called Lm MBE) without antimony source, and the other one is the modified GEN-II on right hand side (called Rn MBE) equipped with antimony source. The two systems are similar to each other and linked with a trail-included extension chamber for wafer manipulation. The samples studied here are grown with the Rn MBE. Fig 3.2(a) and 3.2(b) respectively shows the side view and rear view of the Rn MBE. A sketch is depicted in Fig. 3.3 for better understanding of the configuration. The system comprises of three parts: entry/exit chamber, buffer chamber, and growth chamber. They are joined with 6-inch VAT gate valves as seen in the sketch. Each chamber is connected to the vent system via a metal-sealed angle valve, which can lead to a pure nitrogen gas line and a pump station (not shown in the sketch) for purposes of system purge and roughly pumping down from atmosphere. The pump station consists of an oil-free diaphragm pump and a turbo-pump. Each chamber has its own function described in the following section.
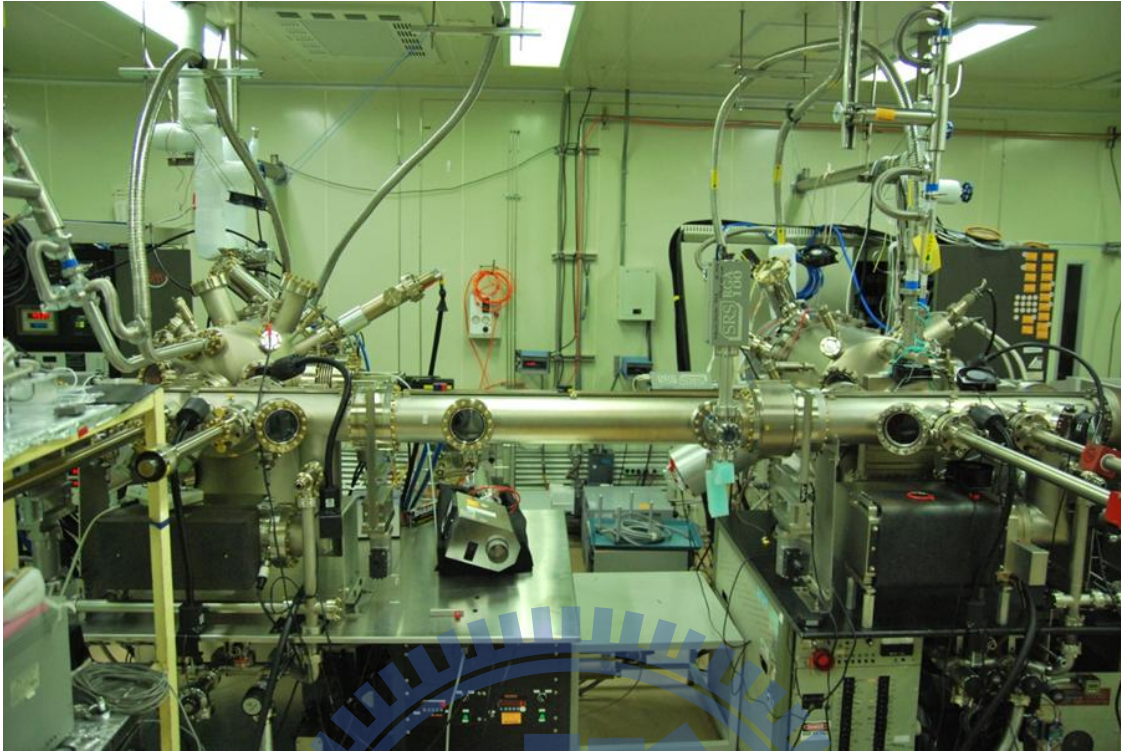
Fig. 3.1 Front view of the Lm MBE and Rn MBE linked with a center extension chamber.
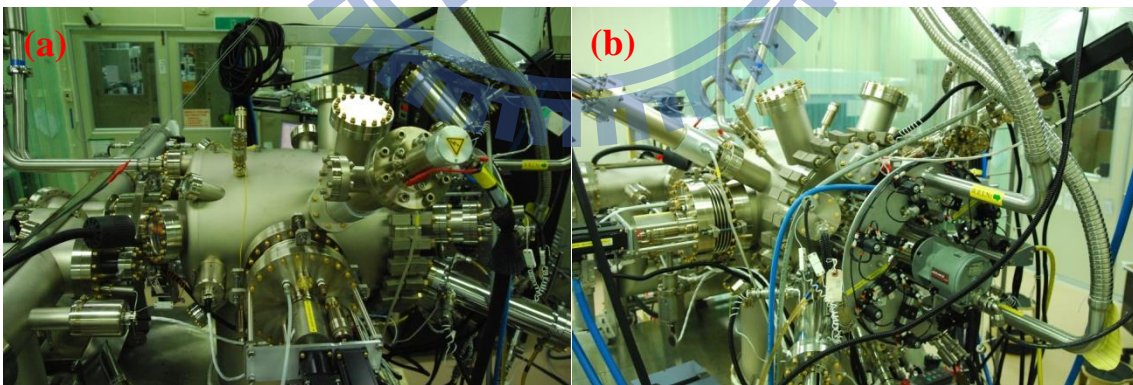
Fig. 3.2(a) side view and (b) rear view of the Rn MBE.
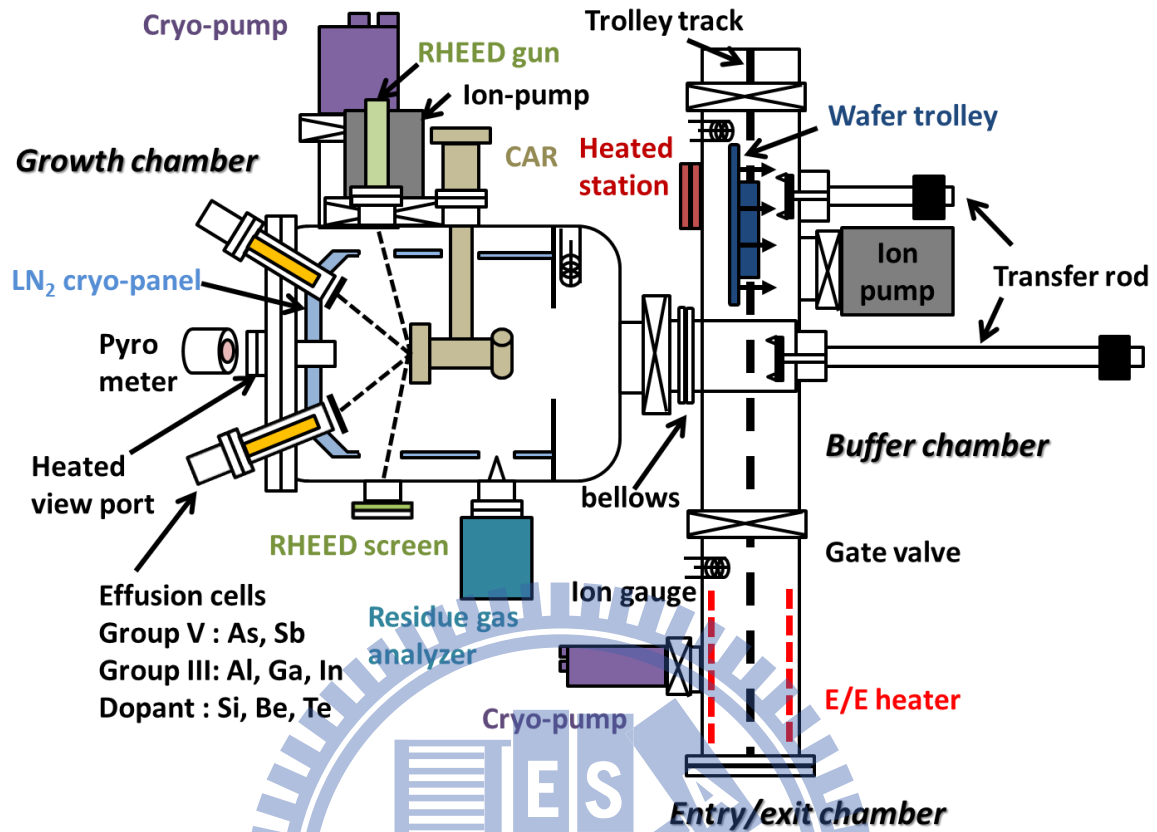
Fig. 3.3 The configuration sketch of the Rn MBE. Three parts of the system, Entry/exit, buffer, and growth chambers, are divided and separated by gate valves. The Entry/exit chamber functioned for sample loading is equipped with a cryo pump for ultra-high vacuum (UHV) maintenance and a heater for the 200°C bake. The buffer chamber functioned for wafer preparation is equipped with a heated station for wafer baking and an ion pump for UHV maintenance. The growth chamber functioned for wafer epitaxy is equipped with shutter controlled effusion cells contained sources of As, Sb, Al, Ga, In, and with dopant cells of Si, Be, and Te. The CAR holds the wafer during growth process, which could control the growth temperature and rotate continuously for the deposition uniformity. The RHEED system uses high energy electron beams hitting the wafer surface to in-situ monitor growth condition. The pyro meter monitors wafer surface temperature via optical detection. The growth chamber is equipped with a residue gas analyzer to analyze kinds of molecules inside the chamber and to detect leakage. The UHV environment is maintained by an ion pump and a cryo pump, and assisted by the liquid nitrogen flow in cry-panel during growth.

3.1-1 Chambers' configurations, utilities and functions

The entry/ exit (EE) chamber is also called load-lock chamber, where the trolley moves in or out through an oring-sealed quick door. Wafers are mounted by holders made from Mo, called uni-block, and hanged on the trolley, which moves on the trolley track inside the

chamber. The EE chamber equipped with a low vibration cryo-pump to maintain ultra-high vacuum (UHV) environment around an order of 10^{-9} torr. The EE heater could provide $200^{\circ}C$ baking for driving out the vapor accompanied with wafers and holder when reloading. As the vacuum below 1e-8, the trolley can be transferred into buffer chamber.

In the buffer chamber, wafers are pre-baked around ~4 hours at a heated station and stand by for growths. The purpose of baking is to remove organic contaminations of the wafer. Baking temperatures of $400^{\circ}C$, $350^{\circ}C$, and $300^{\circ}C$ are used respectively for substrates of GaAs, InP, and InAs. The UHV environment can be as low as an order of 10^{-10} torr, which is maintained by an ion pump integrated with a mini titanium sublimation pump (TSP). The titanium can be sublimated to help vacuum pumping by solidifying molecular gas.

Growth chamber is where substrates perform layer growths. Three kind sources of group-III: gallium (Ga), indium (In), and aluminum (Al) are charged in the effusion cells. The type of the cell has a brand name called sumo cell in VEECO company's products, the bulk and tip temperatures of which can be PID controlled and monitored. Except for the cold-lip design of Al cell, other cells are operated at a higher tip temperature than the bulk temperature. Group V species of arsenide (As) and antimonite (Sb) are supplied with two cracking cells, molecular flux of which can be adjusted by their step-motor-positioned needle valves. Dopants cells of silicon (Si), beryllium (Be), and tellurium (Te) are installed. Molecular beam source of every cell can be open or closed by a computer controlled shutter. UHV environment of growth chamber is maintained by an ion pump and a cryo pump. A TSP is also equipped and functions occasionally to help vacuum pumping. The cryo-panel is cooled down to a temperature of 77K and continuously flowed with liquid nitrogen during growth. Cold cryo-panel surface traps molecular beam and keeps a background pressure order of 10^{-9}~10^{-10} torr. The residual gas analyzer, operated as pressure under ~10^{-8} torr, is to analyze the amount and the species of molecule inside the chamber. It also provides the sensitive helium leakage

test mode (a sensitivity of ~10^{-12}) to detect a leakage place by monitoring helium partial pressure as purging helium from the outside of the chamber at the same time. The reflection high energy electron diffraction (RHEED) system is a very important utility; the high energy (~10KeV) electron beam emits from RHHED gun, hits the wafer surface at a small angle, and reflects to the RHEED screen. It can be used to monitor wafer surface reconstruction diffraction pattern during growth, and also can be used to check the growth rate, which will be elucidated later. The car holds the epi ready substrate on one side, which can control temperature, and has a beam flux ion gauge to monitor beam equilibrant pressure (BEP) on the other side. The CAR can rotate toward transfer direction or growth direction, and the substrate holder also can continuously spins during growth. The car holder can heat the wafer up to a maximum temperature of 850°C. A pyrometer can measure the wafer surface temperature through a heated view port.

3.1-2 Calibrations of growth rate and doping concentration

Growth rate can be decided by RHEED oscillation as shown in Fig.3.4. A cycle of RHEED on screen goes from bright to dark and back to bright when growth surface goes from intact plane to half-grown surface, which causes lower electron beam reflectivity due to scattering from random occupied sites of atom, and back to a smooth surface after growing a monolayer. The time period thus corresponds to growing a monolayer thickness. Except for In growing on an InAs substrate, others are performed on a GaAs substrate. The growth rate is proportional to group-III molecular beam flux. By correlating to the measured BEP, growth rate versus BEP can be drawn as in Fig. 3.5.
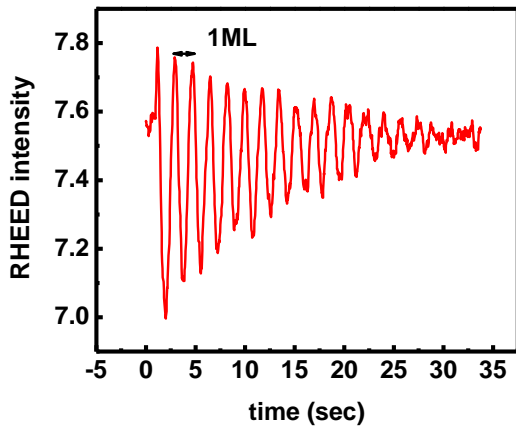
Fig. 3.4 REED intensity oscillation trace for the case of InAs growth.
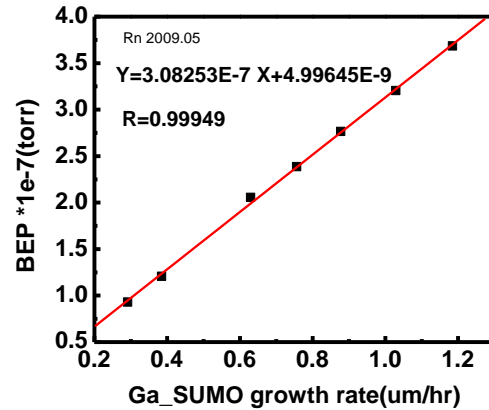
Fig. 3.5 Gallium BEP linearly depends with growth rate for the case of growing GaAs.

The doping concentrations are verified by etched C-V measurements of several layers of GaAs grown with various doping temperatures of cells as shown in Fig. 3.6. The Ga growth rate is fixed at 1μm/hr and each layer thickness is 700nm for every temperature. The n-type of Si, Te and P-type of Be are doing by the same method. The doping rate of material has an exponential relation with cell temperature which leads to a plot as shown in Fig. 3.7. The cell temperature than can be deduced for a target doping concentration.
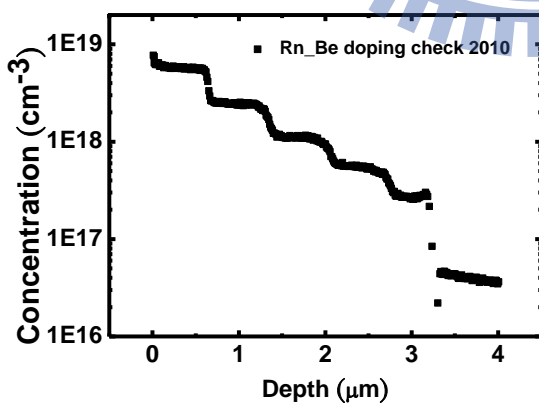
Fig. 3.6 Etched C-V measurement for doping check of the Be case, which is the result of 5 layers of GaAs, each 700nm thick, doped with various Be concentrations using different cell temperatures.
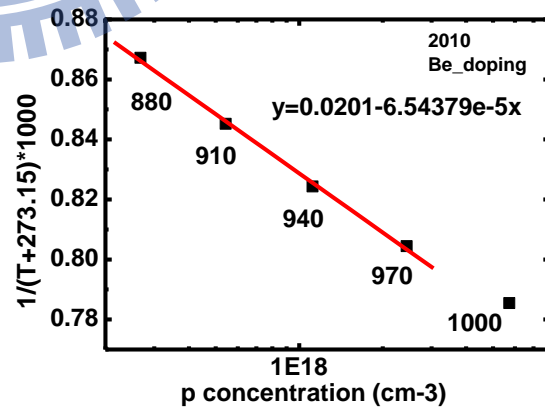
Fig. 3.7 The relationship of doping concentration and doping temperature of the Be cell.

3.1-2 Sample growth procedure

After baking at the heated station and waiting the buffer chamber pressure below 10^{-8} torr, substrate can be transfer to the LN2 cooled growth chamber. Cells warm up and stay steady to the set temperatures. As2 or As4 is provided by using a crack zone temperature of $840\,^{o}$C or $450\,^{o}$C. Sb2 is normally used with a crack zone temperature of $1050\,^{o}$C. The car rises to an appropriate temperature. Then the substrate is rotated and desorbs the surface native oxide under enough group-V BEP. Once the oxide layer has been removed, RHEED paten becomes streaky as shown in Fig. 3.8, which implies surface reconstruction situation under group-V stable condition. The desorption temperatures are ~$620\,^{o}$C for GaAs and ~$520\,^{o}$C for InP and InAs substrates. Group-V species are usually at over pressure to maintain a good growth condition. Typical values for As/III ratio is ~10-20 and Sb/III is ~3-5. After the desorption process, substrate can be set to an appropriate temperature and proceeded to epi-layer growth. All the structures can be programmed and shutter sequences can be precisely controlled by the computer.

Fig. 3.8 The streaky RHEED pattern randomly taken during desorption process on the (001) GaAs substrate. The pattern evolves periodically as the substrate rotates and the substrate direction paralleled to electron beam varies between [100] and [010] directions.

3.2 Material characteristics analysis

3.2-1 High resolution X-ray diffraction system

X-ray offers a non-invasive way to analyze sample properties, which interferences with regularly arranged atoms of crystal and reflect constructively if it meets the Bragg's condition. By varying the incident and received angles, sample information such as composition, layer thickness, lattice constant, and quality can be deduced. Our system is a commercial BeDe D1 high resolution X-ray diffraction meter, which uses crystals on the work path to get a better resolution. Measurements are usually performed at the (004) surface of the zinc-blende crystal and operated in ω−2θ mode. By comparing the signals of epi-layers to the substrate, compositions of epi-layers can be checked. Quality of layers can be judged from its full width of half maximum (FWHM). Fig 3.9 gives the example, which is three different GaAsSb layers with different composition grown on an InP substrate.
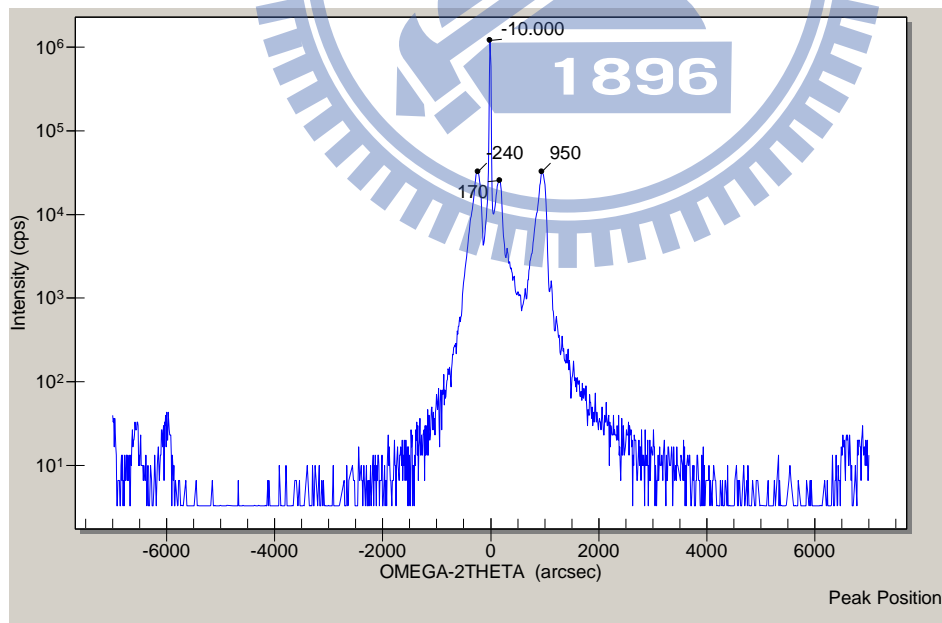
Fig. 3.9 X-ray data scanned in ω−2θ mode for the example of three GaAsSb layers grown on an InP substrate, where peak position values are noted.

3.2-2 Photoluminescence Spectroscopy

Photoluminescence spectroscopy is a simple and non-destructive tool to study samples. In principle the samples are excited by a light source and electron-hole are carriers generated. The carriers relax to lower electronic levels of the structure and recombine spontaneously to release photons. Intensity and spectrum of the luminescence can be collected and measured to analyze sample quality, quantized energy levels, emission wavelength, impurity levels, etc. Sample properties also can be characterized by varying excitation power and temperature.

Our homemade PL system setup is depicted in Fig. 3.10. A continuous Ar+ laser with a tunable wavelength of 488nm or 514.5nm serves as an excitation source, which is conducted via reflections of mirrors and normally incident to a 2-inch diameter CaF_2 focusing lens. It is focused on the sample surface with a spot size ~100μm diameter. The spontaneous emission from the sample goes through a CaF_2 window then collected and transformed into a parallel light by the CaF_2 lens. It goes successively through another 2-inch CaF_2 lens, a laser filter, and is finally focused on the entrance slit of our monochromator, Horiba iHR 550. Samples are placed on a copper chuck mounted to a helium close-cycled cryogenic system, which is capable of tuning temperature from ~10K to 390K inside the chamber under a vacuum~10^{-1} torr. The monochromator has gratings to disperse the light and is integrated with detectors to detect photons. We have two photo detectors for mid-IR regime; one is a thermal electric cooled InGaAsSb photodetector with optical response to ~2.5μm, while another is a liquid nitrogen cooled InSb photodetector with optical response to ~5μm. The signals are handled with a conventional lock-in technique to suppress noise. A chopper is inserted in the Ar+ laser light path and modulated at ~200Hz frequency. Photo detector signals and chopper triggers are fed to a SR-530 lock-in amplifier. The lock-in amplifier can process and output the data to a computer via IEEE 488 bus.
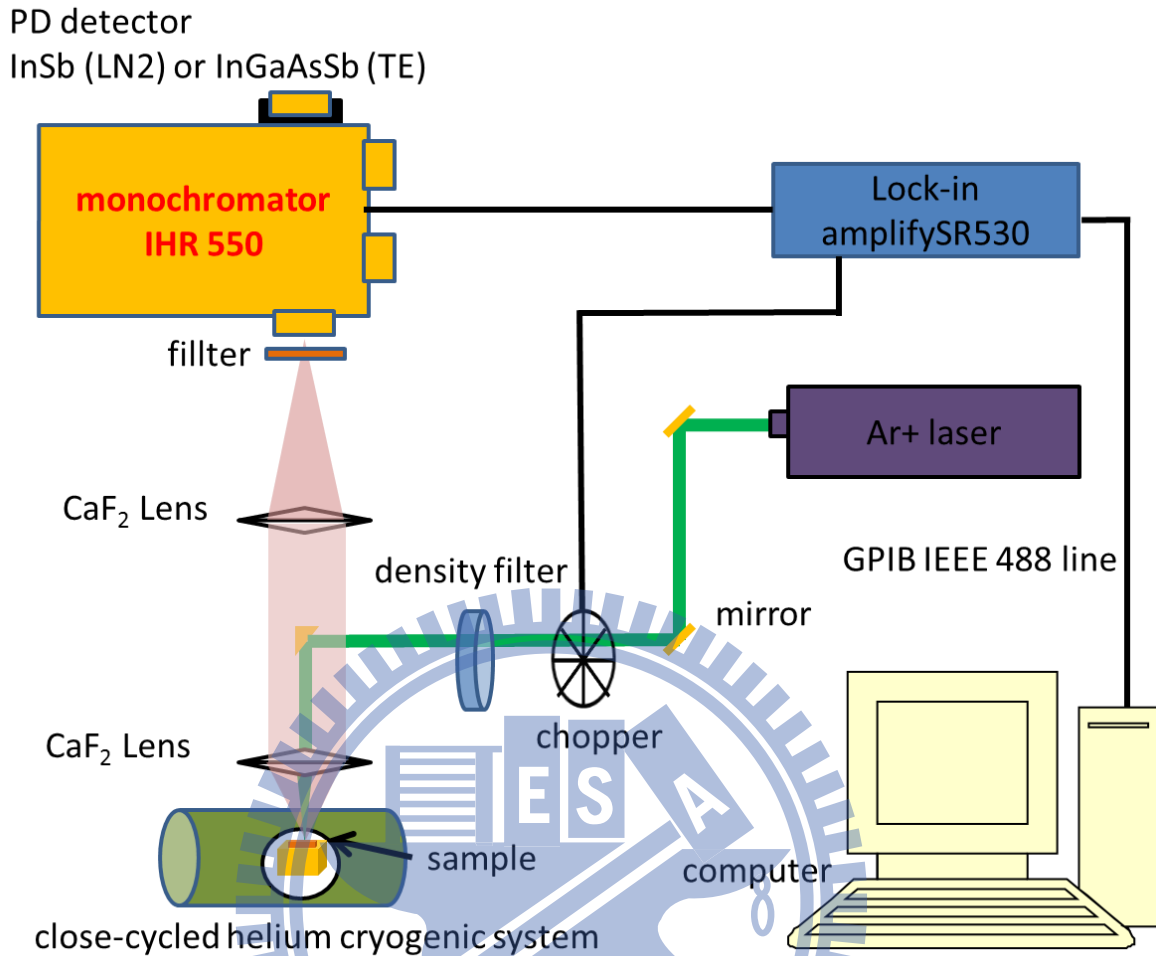
Fig. 3.10 The Scheme of the PL setup of our lab. The excitation source form an Ar+ laser beam (488nm/ 514nm) is directed via mirror reflections, going through chopper, density filter, and focused on to sample surface via a CaF_2 lens. The sample is placed on a copper chuck mounted on a closed cycle cryogenic system capable of temperature tuning from ~10K to 390K. The spontaneous emission is collected by two CaF_2 lenses, passing through a laser filter, and arrives at the entrance slit of the IHR550 monochromator. The singles from the photo detector, which is in the exit slit of the monochromator, finally go to the computer after processing with a conventional lock-in technique.

3.2-3 The setup for optically-pumped lasers measurements

Optically-pumped lasers are different from electrical injected p-n junction lasers, which establish carrier population inversions via optical pumping. The light of the pumping source can penetrate through the thick cladding layer and generate photo carriers inside the active region. Optical pumping provides the way to archive lasing when electrical injection is not favorable due to reasons like large turn on voltage and high resistivity. It has advantages that can be exploited to produce high output power laser and good beam quality. GaSb-based

49

optically pumped "W" lasers have been demonstrated with higher output peak powers and maximum operation temperatures over others [43-45]. It also offers a possibility to perform lasing at dual wavelengths [46].

The pumping source is a commercial 1064nm pulsed fiber laser. The photon energy of 1064nm is 1.17eV, which is small than the band gap of the cladding layer material, $In_{0.52}Al_{0.48}As$, for our lasers. This obviates pumping light absorption by the cladding layer, which is important for optical pumping consideration. The fiber laser can be controlled by a computer which can set the output power percentage, pulse duration, and repetition rate. The output power with maximum 100% percentage can reach a peak power of ~10KW. There are eight pulse durations of 10ns, 30ns, 20ns, 50ns, 75ns, 100ns, 150ns, and 200ns can be selected. The repletion rate can be synchronized by triggers from outside TTL signals and operated arbitrarily from single shot to 500 KHz. Fig 3.11 shows the measured output power as function of output percentage for 20ns pulse duration operated under 100Hz, 1KHz, and 10KHz.

A general optical pumping experiment setup is depicted in Fig. 3.12. The fiber laser is shaped into a size of 3mm x 200μm via a cylindrical lens. It then focuses on the top on sample surface with the along axis in parallel with cavity direction. The mid-IR laser emission from the sample cleaved edge is collected as the same way as the PL setup when measuring the laser spectrum. As for the total output laser intensity (L-L measurements), the mid-IR light from cleaved mirror is collected directly by a aspherical lens (with numerical valure > 0.5) and detected by a thermal-electric cooled InAs photodiode which has integrated with a front filter to block the 1064nm scattering light of the pumping source. The photo detector signal is fed to the lock-in amplify which processes and transfers the data to computer. A function generator is used to generate TTL signals which are sent to the fiber laser and the lock-in amplify for the reference input.
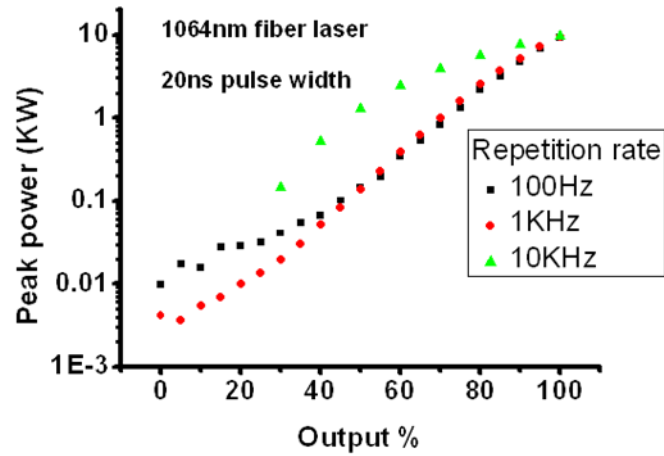
Fig. 3.11 The 1064 nm fiber laser output peak power as function of output percentage for 20ns pulse duration operated under 100Hz, 1 KHz, and 10 KHz.
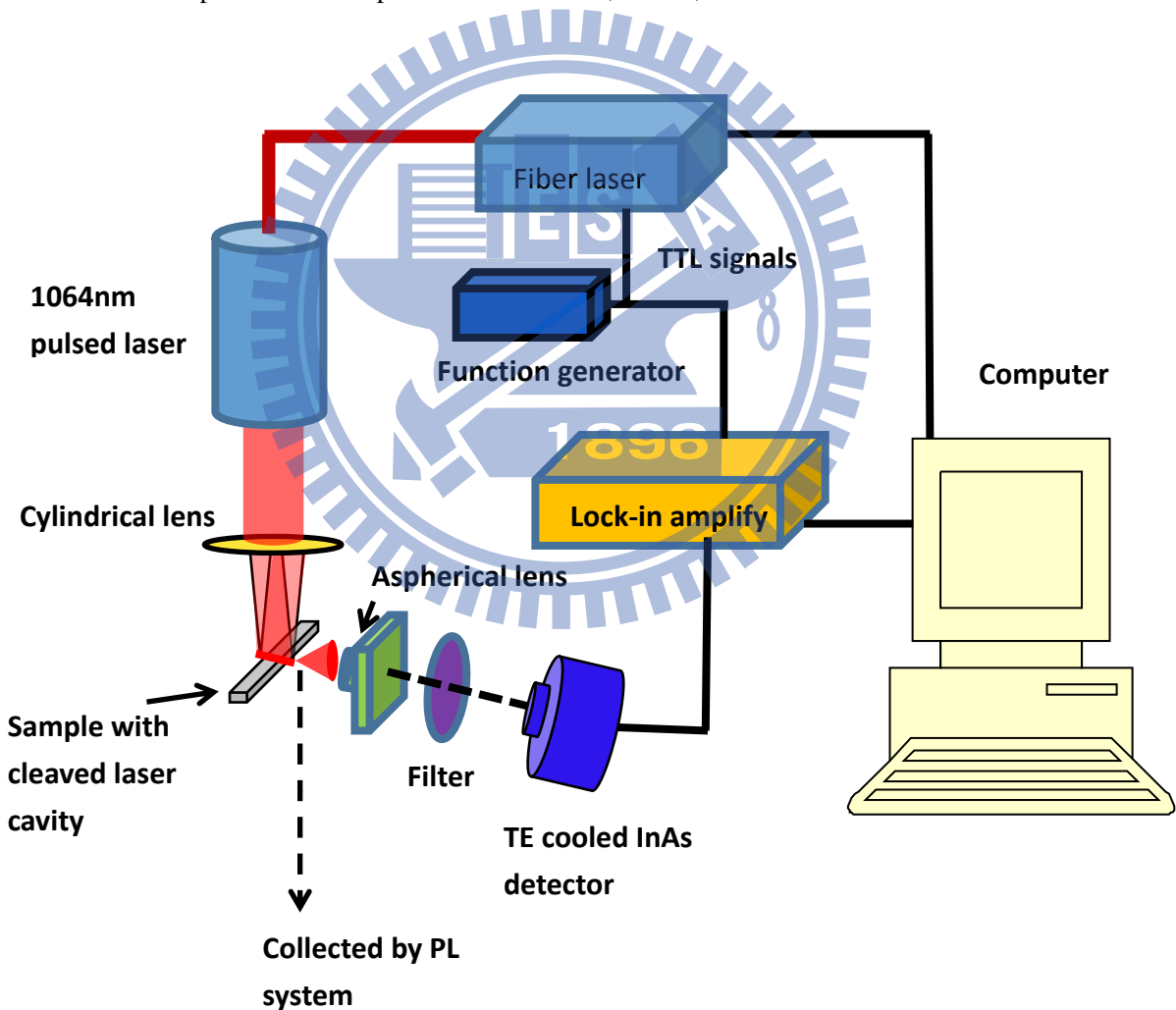
Fig. 3.12 The setup for optical pumping measurements (L-L curve). If the spectrum needs to be analyzed, the output light is collected using the PL system, which is equipped with the monochromator.

Chapter 4

2~3 μm mid infrared light sources using InGaAs/GaAsSb "W" type quantum wells on InP substrates

After introducing theoretical considerations and analysis techniques in chapter 2 and 3, this chapter moves to real growth of our designed type-II "W" quantum wells. The samples were studied via temperature and excitation power dependent photoluminescence experiments. The characteristics of the type-II "W" QWs, such as blue shift of PL spectrum along with increasing excitation power density and the trade-off situation between long emission wavelength and optical momentum matrix element, were discussed and compared with simulation results.

4.1 The growth of ternary alloys lattice-matched to InP substrate

Prior to the growth of real structure, it is important to assure the ternaries, $In_{0.53}Ga_{0.47}As$, $In_{0.52}Al_{0.48}As$ and $GaAs_{0.49}Sb_{0.51}$, have correct compositions to match with the lattice constant of InP substrate. For the ternaries with two group-III species, it was done by adjusting the growth rates of the two group-III species. In our lab, the indium growth rate was calibrated on the InAs substrate, which has a different lattice constant (6.06Å) with the GaAs substrate (5.65 Å) used for gallium and aluminum growth rate calibrations. It should be considered as to derive the correct alloy mole fraction ratio. Taking $In_{0.53}Ga_{0.47}As$ as an example, the indium growth rate (g_In) and gallium growth rate (g_Ga) roughly follow the relation $(g\_In/6.06^3)$ $/((\ g\_Ga/5.65^3)+(g\_In/6.06^3)) =0.53$. Notice that the growth rates are all normalized by its own cubic lattice constant. Conventionally we grew three layers with slightly various growth rate ratio of two III-species, each 200nm thick, on InP substrate. The lattice match condition is

finally checked by XRD measurement.   Fig. 4.1 shows the XRD results of InGaAs and

InAlAs for the lattice match check.
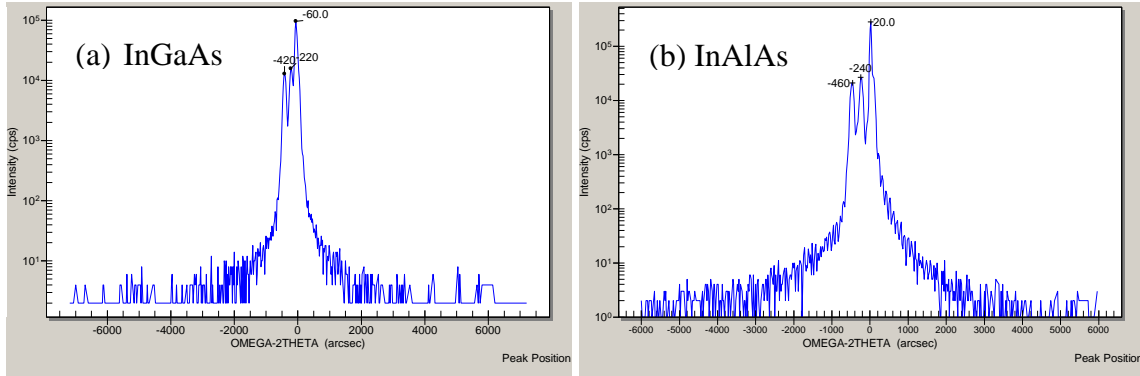
Fig. 4.1(a) InGaAs and (b) InAlAs XRD results for lattice match check on InP substrate. Each sample grown with three layers of slightly various compositions, one of which is nearly coincided with the main peak of InP substrate.

As seen by the Fig. 4.1, the lattice match condition were found and confirmed by one of the

three peaks coincided with the InP substrate. The growth rate of indium is 0.5 μm/hr; the

growth temperature is around 500°C (pyrometer value); the group V to total group III BEP

ratio is around 15-20. The samples were also performed with low temperature PL

measurements as shown in Fig 4.2 to check band gap energies.
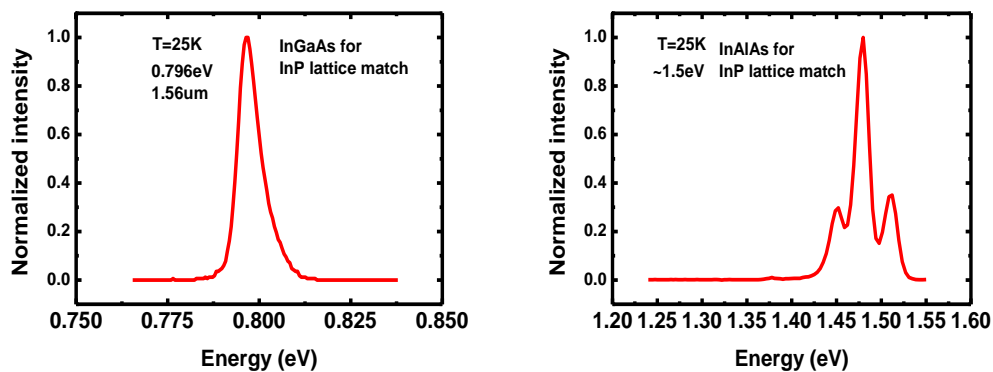
Fig. 4.2 InGaAs and InAlAs low temperature PL results for lattice match check on InP substrate. The bang gap for InGaAs is around 0.8eV and for InAlAs is around 1.5eV.

The GaAsSb ternary composition was mainly controlled by Sb_2/As_2 BEP ratio. The lattice

match condition is shown by the XRD data in Fig. 3.7. The low temperature PL measurement

is shown in Fig. 4.3, which reveals band gap energy around 0.81 eV.
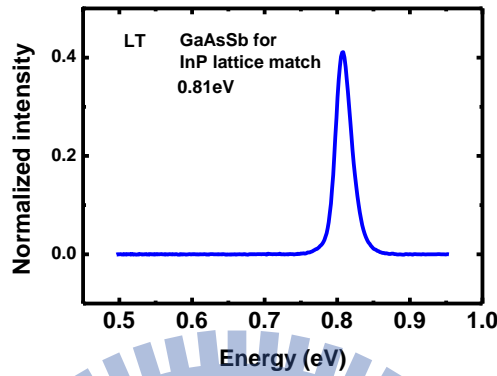
Fig. 4.3 GaAsSb low temperature PL result for lattice match check on InP substrate. The bang gap energy is around 0.81eV.

4.2 The growth condition dependence of Sb fraction in GaAsSb alloy

The GaAsSb includes two group V species that makes it is more difficult to control the

composition. The Sb fraction of the alloy is not linear with the As_2/Sb_2 BEP ratio, which is

shown in Fig. 4.4 according to the work [47].
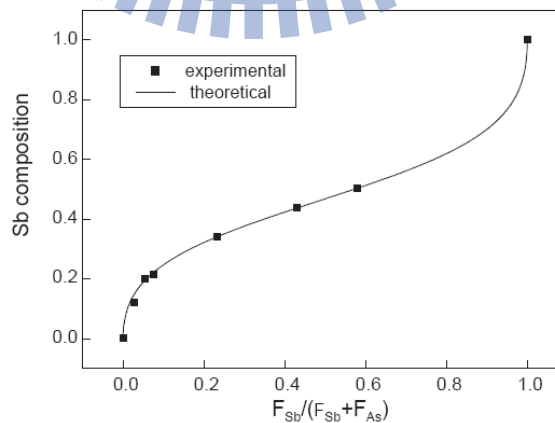
Fig. 4.4 Antimony composition of GaAsSb as a fuction of Sb and As
beam equivalent pressure ratio $F_{Sb}/(F_{Sb}+F_{As})$ [ref. 42].

The Sb incorporation is also greatly influenced by the growth temperature [48]. It has a higher sticking coefficient and incorporation efficiency for the Sb_2 molecular beam under lower growth temperature. The growth temperature effect for the Sb incorporation of the GaAsSb alloy in our MBE system was evaluated by the following experiment. Three GaAsSb layers each with 150nm thickness were grown on InP substrate at pyrometer temperatures, in turn, of 485 ^{o}C, 470 ^{o}C, and 460 ^{o}C, while the As_2 and Sb_2 BEP were kept the same (Sb_2 : 9.3x10^{-7} torr, As_2 : 8x10^{-7} torr). The compositions then were decided by XRD data assuming strain is relaxed in each layer, which is shown in Fig. 4.5. The composition and lattice constant values are listed in the Table.

Tem. (^{o}C)	460	470	485
Com.	$GaAs_{0.25}Sb_{0.75}$	$GaAs_{0.32}Sb_{0.68}$	$GaAs_{0.4}Sb_{0.6}$
Lattice con.(Å)	5.99	5.95	5.92
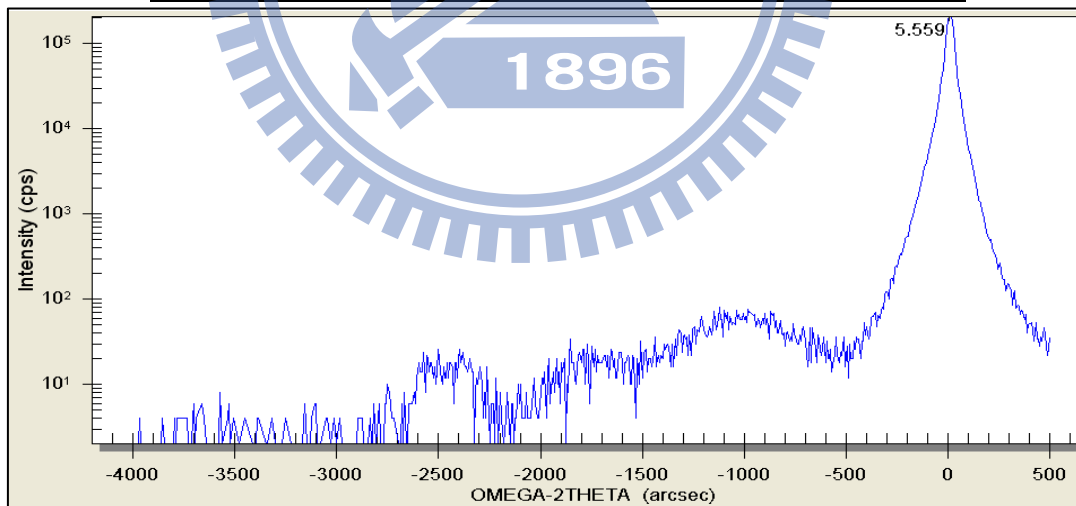
Fig. 4.5 XRD examinations of antimony incorporation of three GaAsSb layers grown on InP substrate at different temperatures, the growth temperatures, compositions ,and lattice constants of each layer listed in the Table.

As seen by the Fig. 4.5, the growth temperature indeed influences the Sb incorporation of GaAsSb ternary dramatically. The temperature difference from 485$^{\mathrm{o}}$C to 460$^{\mathrm{o}}$C leads to a change of the Sb mole fraction from 0.6 to 0.75 in GaAsSb alloy. For precisely determination of the Sb fraction of GaAsSb pseudomorphic layer in "W" structure, it had better to separately grow the GaAsSb layer with same condition during the same run for the XRD check of the composition.

4.3 "W" type quantum wells sample growth

In the following, the mid-IR light sources between 2 μm to 3 μm were studied and designed using the type-II "W" type QWs [27, 28, 49]. We demonstrate that the emission wavelength can be extended longer than 2.56μm at room temperature.

Our samples were grown on S-doped (001) InP substrates. The As$_2$ and Sb$_2$ species were used through the equipped needle-valve controlled cracking cells. The wafer surface temperature was monitored by an infrared pyrometer. For the multilayer growth consideration, the structure of the "W" QWs designed here are the symmetric In$_{0.53}$Ga$_{0.47}$As/ GaAsSb/In$_{0.53}$Ga$_{0.47}$As layers sandwiched between two 2nm In$_{0.36}$Al$_{0.32}$Ga$_{0.32}$As tensile strain layers to compensate the compressive strain in the GaAsSb layer. Nine such "W" type QWs spaced by 25 nm In$_{0.52}$Al$_{0.48}$As barrier layers were grown and placed between two 200 nm In$_{0.52}$Al$_{0.48}$As layers, as shown in Fig. 4.6. In order to optimize the "W" structure, this study was performed systematically by varying the thickness of the InGaAs/GaAsSb layers, the composition of the GaAsSb layer and the growth temperature. The growth parameters are listed in Table 4.1, where three series of samples are grouped and labeled as A, B, and C. Groups A and B are samples with variable thicknesses of InGaAs and GaAsSb, respectively. Group C contains samples with different Sb mole fraction in the GaAsSb layer by adjusting the Sb$_2$/As$_2$ beam equivalent pressure (BEP) ratio. The growth temperature is also changed

from group A to group C.
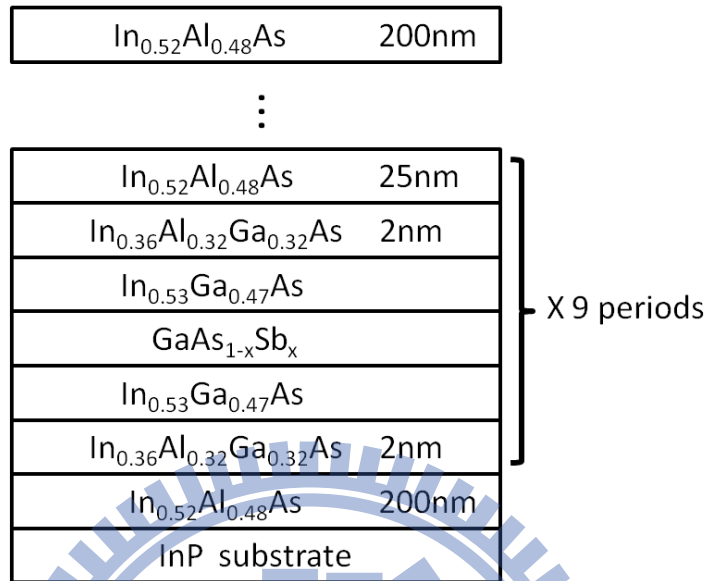
Fig. 4.6 The structure of the designed "W" type QWs.

Table 4.1 The InGaAs/GaAsSb layer thickness, the Sb_2/As_2 BEP ratio, the summarized PL peak wavelength, and FWHM of the "W" type QW samples in group A, B, and C.

Sample number	Layer thickness(nm)			BEP ratio Sb_2/As_2	Growth T(^{o}C)	λ_{peak} (μm)	FWHM (meV)
	$In_{0.53}GaAs$ (lattice match)	$GaAs_{1-x}Sb_x$	x				
A1	4	3	0.58	1.8	475	2.05	24.7
A2	7	3	0.58	1.8	475	2.34	22.4
A3	10	3	0.58	1.8	475	2.47	25.4
B1	5	2	0.65	2.0	470	2.17	22.7
B2	5	3	0.65	2.0	470	2.27	18.8
B3	5	4	0.65	2.0	470	2.42	13.9
C1	4	3	0.74	1.8	460	2.37	12.6
C2	4	3	0.78	2.9	460	2.48	13.8

4.4 Photoluminescence results and discussion

After the samples were grown, the photoluminescence (PL) measurement was carried out using a 488nm Ar^+ laser as the excitation source and a thermal electric cooled InGaAs(Sb) detector. All the PL spectra were calibrated by the response spectrum of a 1000^oC black radiation source. The PL spectra measured at 20K are presented in Fig 4.7(a). The peak emission wavelength (λ_{peak}) covers the range from ~2 μm to ~2.5 μm. As summarized in Table 4.1, the λ_{peak} can be extended from 2.05 μm to 2.47 μm by increasing the InGaAs layer thickness from 4 nm to 10 nm as shown in group A, and can be extended from 2.17 μm to 2.42 μm with the increase of GaAsSb layer thickness from 2 nm to 4 nm (in group B). The sensitivity of λ_{peak} to the InGaAs/GaAsSb layer thicknesses agrees well with our calculations. Notice that the full width of half to maximum (FWHM) of the PL spectra increases from 13.9meV to 22.7meV when the GaAsSb layer thickness is reduced, as indicated in group B. This is caused by the energy level broadening due to the thickness fluctuation when the GaAsSb layer is thin. The λ_{peak} can be also extended by the increase of the Sb-content, as shown by group C samples. The Sb fraction is determined by fitting the λ_{peak} with the calculation results. The λ_{peak} goes from 2.37 μm to 2.48 μm, around a 23 meV difference, as the Sb mole fraction increases from 0.74 to 0.78. We can also see the effect of growth temperature by comparing these three groups of samples. It is found that the samples grown at a lower temperature have a longer emission wavelength and a narrower PL spectrum. This indeed indicate that the Sb incorporation is more efficient and the fluctuation of alloy composition is less at lower growth temperatures [50, 51]. Figure 4.7(b) shows the integrated PL intensity as a function of the emission wavelength. It clearly shows the trade-off situation as predicted by the simulation. The calculated curve, which is based on the assumption that the integrated PL intensity is proportional to the square of the wave function overlap, fits very nicely with the experimental results.
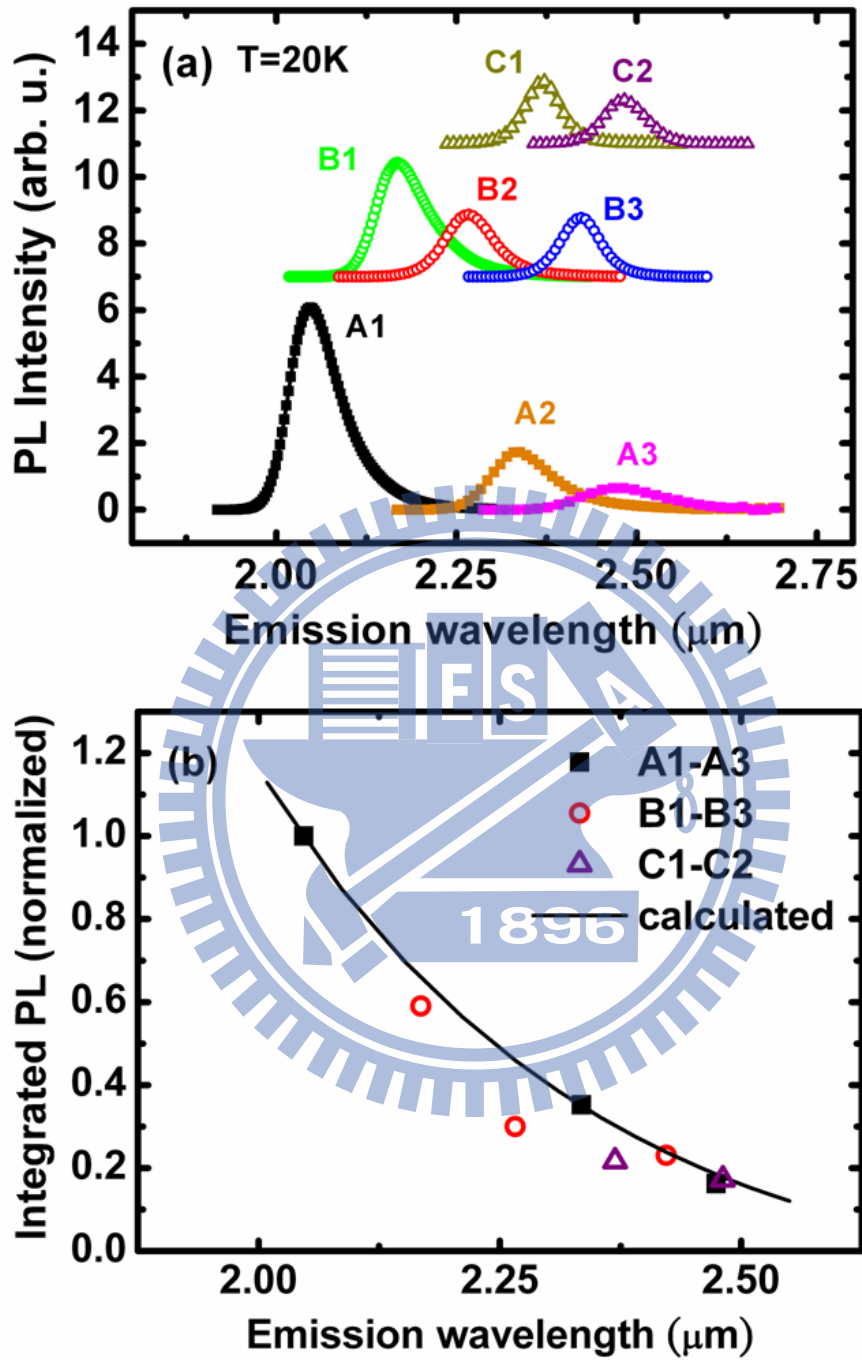
Fig. 4.7 (a) PL spectra of samples in group A, B, C, and (b) integrated PL intensity (normalized at sample A1) plotted against the peak wavelength. The calculated result is plotted as the solid curve.

The optical transition of the type-II heterostructure has been extensively studied previously [52, 53]. The λ_{peak} usually blue shifts with the excitation power (P_{ex}), and the amount of shift is linearly dependent on the one-third power of P_{ex} because of the band bending effect caused by the accumulation of spatially separated electrons and holes in the adjacent triangular interface potential wells. However, the power dependent emission of a "W" type QW has never been studied in detail. We found that, although λ_{peak} shifts to a shorter wavelength as P_{ex} is increased, the energy shift does not obey the $P_{ex}^{1/3}$ law, especially under low P_{ex}. The power dependent spectra of sample A1 and C1 are presented in Fig. 4.8(a), and the amount of energy shift is plotted as a function of the P_{ex} in Fig. 4.8(b) along with the ideal $P_{ex}^{1/3}$ curve for comparison (both axes in log scale). Since the curves are not linear in this log-log plot, the energy shift vs. P_{ex} does not follow any power law. We also notice that sample A1 has a more pronounced energy shift than sample C1. This power dependent behavior is not due to the heating effect since the integrated PL intensity is linearly proportional to P_{ex}, as shown in the inset of Fig. 4.8(b). The possible reason for the amount of blue shift to deviate from the $P_{ex}^{1/3}$ law is the state filling effect of the localized states. The localized states are caused by interface roughness and alloy composition fluctuation, which are common in the ternary alloy [54, 55]. Under low excitation powers, the generated carriers occupy the localized states with lower energies. As the amount of carriers is increased with increased P_{ex}, higher energy states are occupied and therefore the peak of the emitted light shifts to a shorter wavelength. The extended tail in the low energy side of the PL spectra shown in Fig. 4.7(a) and Fig. 4.8(a) is an indication of the radiation from these localized states.
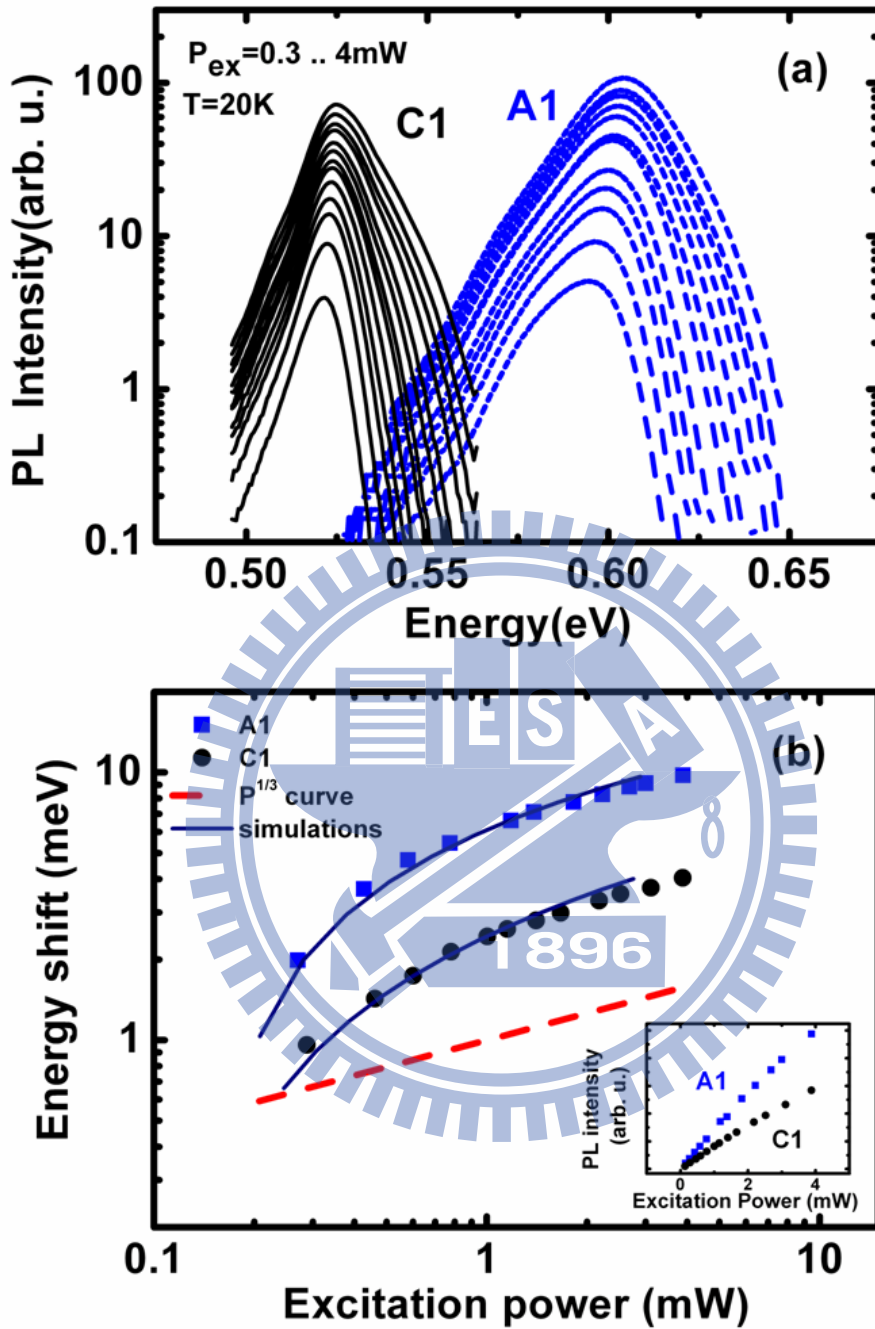
Fig. 4.8 (a) Power dependence PL spectra of sample A1 and sample C1, and (b) the energy shifts versus P_{ex} along with the simulation results and the ideal $P_{ex}^{1/3}$ curve for comparison. The inset shows the power dependence of the integrated PL intensity.

We have performed a simulation for such effect by assuming a joint density of states associated with the localized states as erfc(($<E_0>$-E)/δE), where erfc is the complementary error function, $<E_0>$ and δE refer to the average and the standard deviation of the transition energy to take into account of the inhomogeneous broadening effect [56]. δE values of 30meV and 18meV were used in the calculation for samples A1 and C1. When the Fermi level is raised because of a higher pumping power, the emission peak blue shifts to a higher energy. This behavior is represented schematically in Fig 4.9. The calculated results are shown together with the experiment data in Fig. 4.8(b). Excellent agreement between the calculated and the experimental results was achieved. Since sample A1 has a broader PL spectrum, it has a larger δE and a more pronounced states filling effect. Therefore it has a larger energy shift compared to that of sample C1. We have also estimated the blue shift contributed by the band bending effect. The bending potential profile is solved by the Poisson equation, which depends on the charge distributions. However, the charge distributions, assumed proportional to the wavefunction probability, are solved by the potential profile depended Schrödinger equation. We solve the two coupled equations iteratively until the results are convergent. It turns out the blue shifts along with the carrier densities are not much, for example the mount of blue shift is around 5meV for the structure A1 as the 2D carrier density is increased from $2x10^{11}$ cm^{-1} to $1x10^{12}$ cm^{-2}, which is over the density range Ar+ laser excited in the experiments. The reason is that both electron and hole have been under the strong quantum confinement in the "W" structure. The band bending effect caused by the charge separation merely perturbs the system without altering the quantum levels much, which might be different to general type-II structures that only one carrier is confined inside a quantum well. In general, both the states filling effect and the band bending effect should contribute to the energy shift. The reason that states filling effect dominates here is due to the large δE and the relative small band bending effect in "W" type QWs.

Joint density of states
~ erfc(-(E-E$_0$)/ΔE)

ΔE: 30meV for sample A1
18meV for sample C1

Fermi filling
as P$_{ex}$ increases

PL spectrum
blue shifts

Sample A1: larger FWHM
So more pronounced states
filling effect (blue shifts faster)

Energy
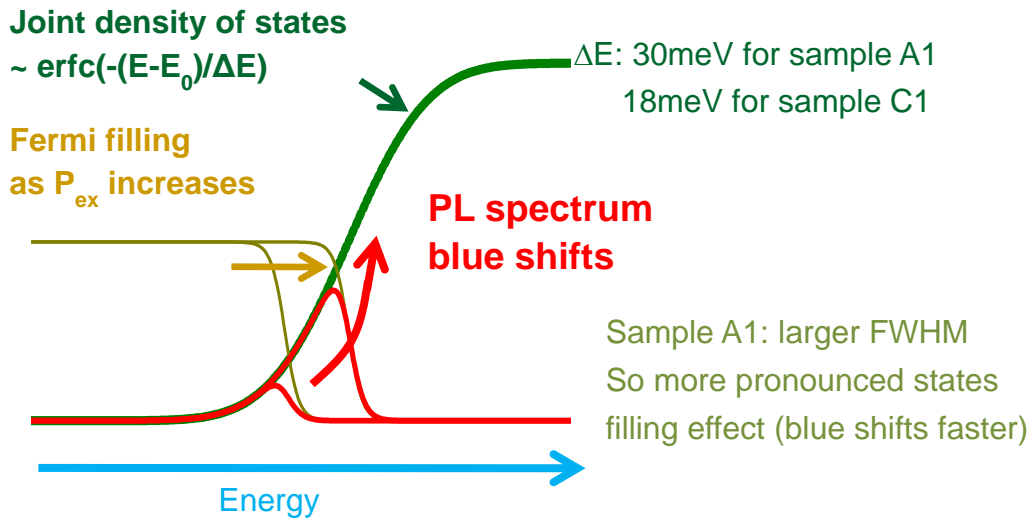
Fig. 4.9 The scheme represents that the localized states filling effect leads to blue shifts of PL spectrum.

In order to examine the sample emission at higher temperatures, we have done the PL measurement with the temperature varied from 35K to 290K under a fixed 10mW excitation power. Figure 4.10(a) shows λ_{peak} as a function of temperature for samples A1, B1, B2, and B3. As the temperature rai33ses, the emission wavelength red shifts as expected due to the band gap shrinkage. The cut-off λ_{peak} around 2.56μm in the spectrum of sample B3 is caused by the lens absorption in our measure system. The temperature dependence of the emission peak is fitted well with the Varshni relation, $E(T)=E(0)-\alpha T^2/(\beta+T)$, as shown the curves in Figure 4.10(a). The peak wavelength can be extrapolated to 2.67 μm at room temperature in sample B3. The temperature dependence of the normalized integrated PL intensity is presented in Fig. 4.10(b). It shows only about one order of magnitude reduction in the PL intensity from LT to RT. The reason that the "W" type QWs emission intensity can be well sustained to high temperatures is due to the good carrier confinement and a low density of nonradiative defects in our samples.
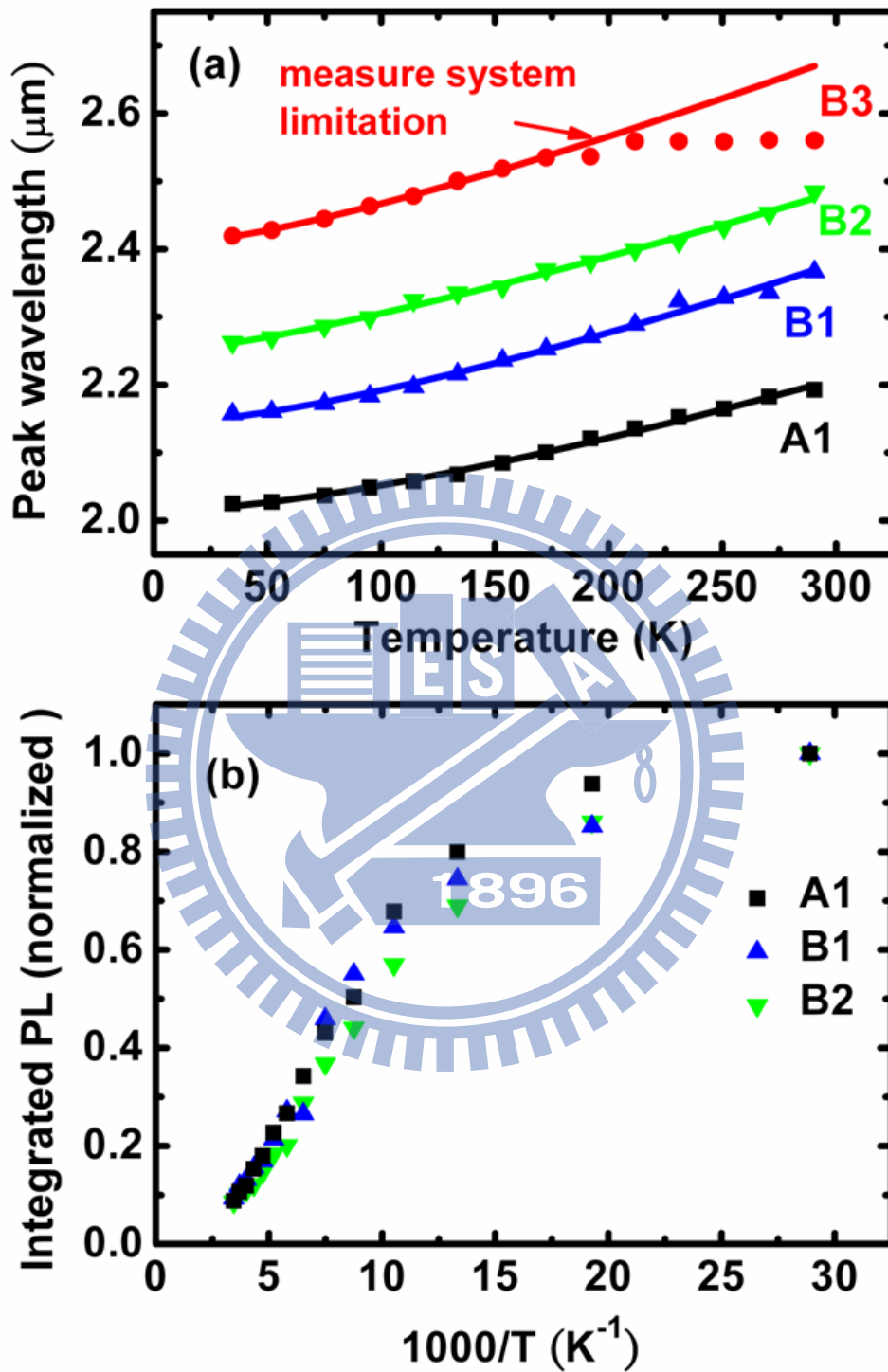
Fig. 4.10 (a) PL peak wavelength v.s. temperature in sample A1, B1, B2, and B3. (b)Temperature dependence of the normalized integrated PL intensity (points) with the fitted Varshni curves.

4.5 Brief conclusions and light emission over 3μm at room temperature

In previous section, we have presented the systematical studies of the InGaAs/GaAsSb/InAlGaAs/InAlAs "W" type QWs grown on InP substrates. The emission wavelength covers the range from ~2 to ~2.5 μm at low temperature. The trade-off between long wavelength emission and high optical matrix element predicted by the simulation has been confirmed by the results of PL spectra. The type-II band alignment in the "W" structure has been characterized by the power dependent PL measurements. The peak position shifts to shorter wavelength as P_{ex} increases. It was found the amount of energy shifts does not follow the $P_{ex}^{1/3}$ law as most type II structures. The localized states filling effect due to the surface roughness and alloy fluctuation is proposed to explain the observed phenomenon. The calculated results agree well with the experiment results. The temperature dependent PL spectra show the well sustained emission at RT, and the emission wavelength of the "W" type QWs can be extended to over 2.56 μm.

Actually the recent progresses have been made to extend emission wavelength over 3 μm at room temperature. Four samples, A, B, C, and D, were grown with "W" type QWs designed as $In_{0.53}Ga_{0.47}As/GaAs_{1-x}Sb_x/In_{0.53}Ga_{0.47}As$ thickness of 4/3/4 nm and nominal Sb fraction, in turn, of 0.74, 0.78, 0.84 and ~0.9 in GaAsSb (samples A and B are the same as C1 and C2 in previous section). Normalized photoluminescence (PL) intensities at 77K and room temperature are shown in Fig. 4.11(a) and Fig. 4.11(b).Absorption problem had been handled by using CaF_2 lenses and an InSb detector were used for longer wavelength emission detection. The tradeoff situation can be observed as predicted by calculations; although there are vapor absorptions around 2.7μm causing multiple peaks in spectrum. The C and D samples show wavelengths emission up to ~3.3μm at 77K and ~3.1 μm at room temperature respectively, which were achieved for the first time in this material system.

According to our experiments and simulation results, it is very promising to develop the

Mid-IR lasers on InP substrates employing the "W" structure of InGaAs/GaAsSb/InGaAs QWs.
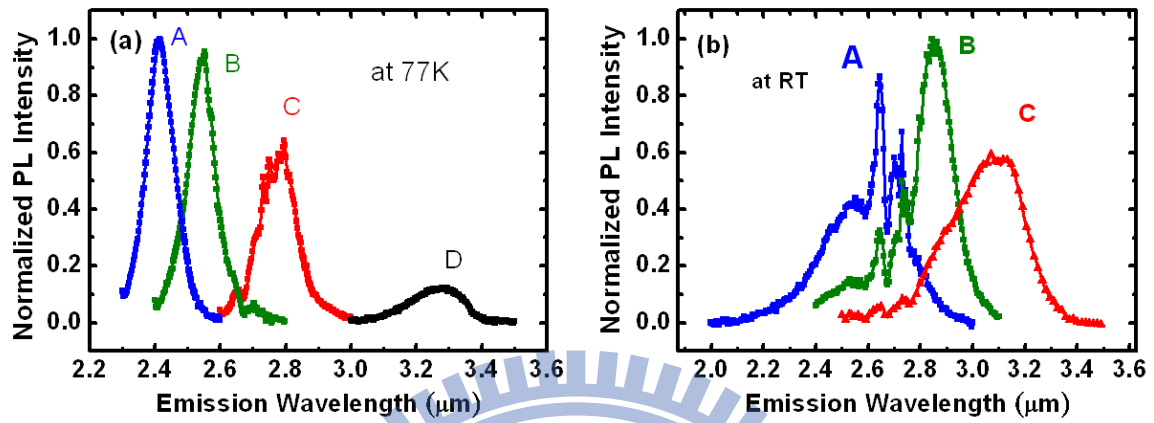
Fig. 4.11 Normalized photoluminescence spectrum of samples at (a) 77K and (b) room temperature (multiple peaks around 2.7μm are caused from vapor absorptions)
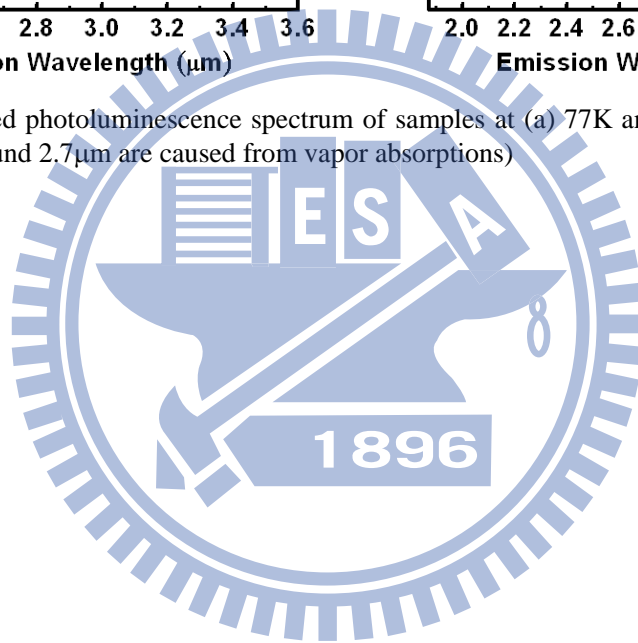
Chapter 5

Room temperature optically-pumped mid-IR lasers with "W" type InGaAs/GaAsSb quantum wells on InP substrates

In chapter 4, basic features of type-II "W" QWs have been studied by PL measurements. In this chapter, we describe the design and fabrication of type-II "W" QWs mid-IR lasers. For the first time, we successfully demonstrated the room temperature mid-IR lasers with the emission wavelength up to 2.56 μm using InGaAs/GaAsSb "W" type QWs on InP substrates via optical pumping. Lasers with laser cavity lengths were characterized at different temperatures to obtain the characteristic temperature, T_0, and the internal optical loss. We also performed band structure E-k relation calculation, modal gain calculation, and waveguide simulation. The Auger process was evaluated by the estimation of an Auger coefficient.

5.1 The structure of type-II "W" QWs mid-IR laser

The samples were grown on S-doped (001) InP substrates by our Veeco GEN Ⅱ molecular beam epitaxy system equipped with needle valve controlled As and Sb cracking cells. The group V species of As_2 and Sb_2 were used during the growth process. The active region of the laser diode had 15 stacks of the "W" QWs with each consisting of a symmetric $In_{0.53}Ga_{0.47}As/GaAs_{0.25}Sb_{0.75}/In_{0.53}Ga_{0.47}As$ (4/3/4nm) structure sandwiched between two 2 nm $In_{0.36}Al_{0.32}Ga_{0.32}As$ strain-compensated layers. The stacks were separated by 5 nm $In_{0.52}Al_{0.48}As$ barrier layers. The active region had a total thickness of ~300nm and was grown at 460°C. The bottom and top optical cladding layers were made of lattice-matched $In_{0.52}Al_{0.48}As$ grown at 500°C. Taking advantage of the lower refractive index of the InP substrate, only 0.3μm bottom cladding layer was used. The top cladding layer had a thickness

of 2.25 μm and was capped by a 100 nm $In_{0.53}Ga_{0.47}As$ layer. The laser structure is shown in Fig. 5.1.

	Composition	Thickness(nm)
cover layer	$In_{0.53}Ga_{0.47}As$	100
Top cladding layer	$In_{0.52}Al_{0.48}As$	2250
Active region	15 x "W" type QW	300
Bottom cladding layer	$In_{0.52}Al_{0.48}As$	200
(001) n+ InP substrate		

	$In_{0.52}Al_{0.48}As$	5
	$In_{0.36}Al_{0.32}Ga_{0.32}As$	2
	$In_{0.53}Ga_{0.47}As$	4
"W" type QW per stack	$GaAs_{0.25}Sb_{0.75}$	3
	$In_{0.53}Ga_{0.47}As$	4
	$In_{0.36}Al_{0.32}Ga_{0.32}As$	2
	$In_{0.52}Al_{0.48}As$	5

x 15 times

Fig. 5.1 The structure of designed type-II "W" QWs mid-IR laser.

5.2 E-k band structure calculation and waveguide simulation

We have theoretically calculated the band structure of our "W" type QW using the 8-band *k.p* theory. The result is shown in Fig. 5.2. The material parameters used in the calculation were taken from the published literature [4]. Based on the calculation, the effective band gap is ~0.5eV. Because of the coupling between the two InGaAs electron QWs, there is a small energy splitting of ~11meV between the symmetric E1 and the anti-symmetric E2 bands at the Brillouin zone center. The energy separation between the first heavy hole (HH1) band and the

first light hole (LH1) band, however, has a large value of ~197 meV, which is due to the small width of the hole QW and the large valence band offset of the InGaAs/GaAsSb type-II structure. The calculated squared optical momentum matrix element between E1and HH1 at zone center is 1.24 (eV*m_0), and that between E2 and HH1 at zone center is zero due to the anti-symmetric nature of the E2 wavefunction. The in-plane effective masses determined via parabolic curve fitting are $0.071m_0$ for the E1 band edge and $-0.095m_0$ for the HH1 band edge at zone center. The greatly reduced heavy hole effective mass is attributed to the compressively strained GaAsSb layer. This could lead to a lower transparency carrier density and a higher differential gain for the laser operation.

The 15 stacks "W" QWs also form the optical core for the waveguide. The fundamental TE_0 optical mode was simulated using the refractive index (n_r) values of 3.1/ 3.14/ 3.49(3.49) for the layers of InP/ InAlAs/ InGaAs(GaAsSb). The results are presented in Fig. 5.3, which show the near field pattern with an effective refraction index of ~3.17 and the far field profile with a ~48 degree of vertical divergence angle. A calculated value of 17.6% is derived for the confinement factor.
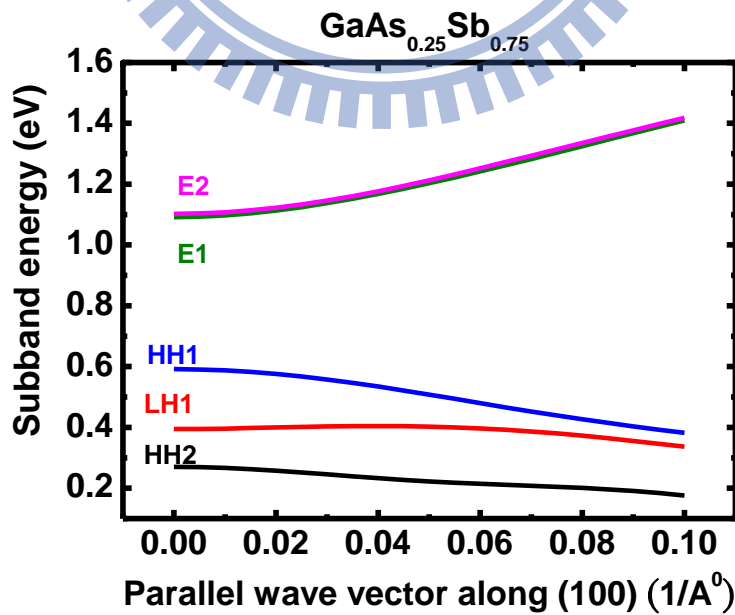
Fig. 5.2 The E-k band structure of the designed "W" type QW based on the 8-band *k.p* model.
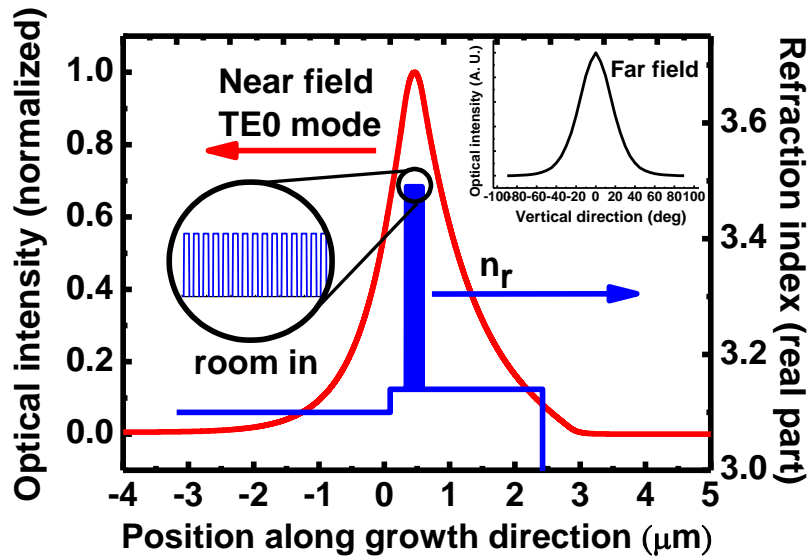
Fig. 5.3 The simulated near field TE0 mode and wave guide index profile. The inset figure is far field pattern versus vertical angle.

5.3 Experimental results and laser characteristics discussion

The sample was cleaved to form a 1 mm long cavity and optically pumped by a 1064nm (~1.2eV) pulsed fiber laser shaped via two cylindrical lenses, resulting in a beam size of ~ 200μm (width) x 3mm (length). The long axis of the pump beam was aligned in parallel with the cavity direction. The pumping light penetrated the thick InAlAs (~1.5eV) cladding layer and was absorbed by the active region. Photo-generated carriers then down converts the pumping light into mid-IR light through the radiative recombination in the "W" QWs. The light output from the cleaved mirror went through a long-pass filter and two focusing lenses. It was then dispersed through a monochromator and detected by a thermal electric cooled InGaAsSb photodetector. The room temperature lasing behavior is shown in Fig. 5.4. The L-L curve was measured under pulsed operation with 20 ns pumping pulses at a 100 Hz repetition rate. The lasing phenomenon is confirmed by the dramatically increased output power as well as the abruptly shrunk spectrum after a threshold power density (P_{th}) of ~40 kW/cm^2. Using separate measurements of the transmission and reflection of samples with and without the epilayers, we estimated that around 25% of the pumping light was absorbed by the active

region. The transmission spectrum and the reflection spectrum are shown in Fig. 5.5. Taking into account of the surface reflection and the percentage of the power absorbed, the absorbed threshold power density per well is ~0.467kW/cm^2. The spectra at 0.98P$_{th}$ and 1.02P$_{th}$ are shown in the inset of Fig. 5.4. The lasing wavelength is at 2.56 µm corresponding to the transition between the lowest E1 state and the first quantized heavy hole state (HH1).
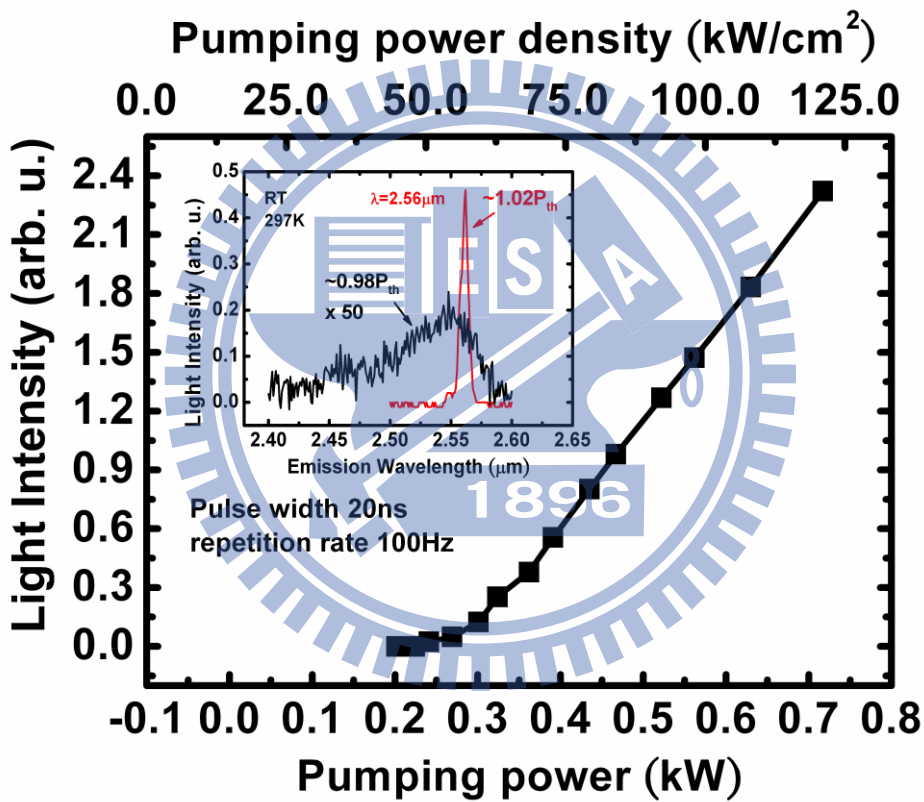
Fig. 5.4 The L-L curve of a 1mm long "W" type laser at room temperature. The inset figure is the lasing spectra at ~0.98P$_{th}$ (Intensity 50x) and ~1.02P$_{th}$.
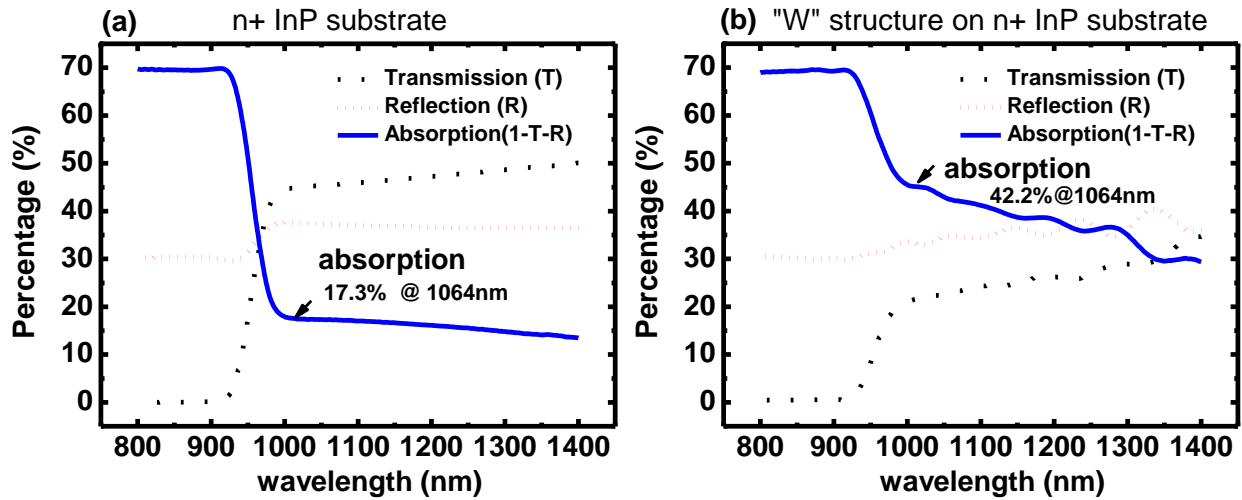
Fig. 5.5 Transmission, reflection, and absorption spectra of (a) n+ InP substrate only indicated with 17.3% absorption at 1064nm pumping wavelength, and (b) "W" laser structure on n+ InP substrate indicated with 42.2% absorption at 1064nm. ~25% absorption of active region is estimated, based on the calculation of 42.2%-17.3%.

We have measured L-L curves of lasers with different cavity length (L) to extract internal loss (αi) at room temperature. The obtained external quantum efficiency (ηd') can be described as the actual external quantum efficiency (ηd) multiplied by a correction factor C accounted for the imperfect light collection. Although C is unknown, the plot of 1/ηd' versus L can still be used to derive αi based on the relation ηd'=C*ηd=C*ηi /(1+αi/ln(1/R)*L), with ηi referring to internal quantum efficiency and R referring to the facet reflectivity (here ~0.27). The derived αi is around 10.7cm^{-1}(in below Fig 5.6.).
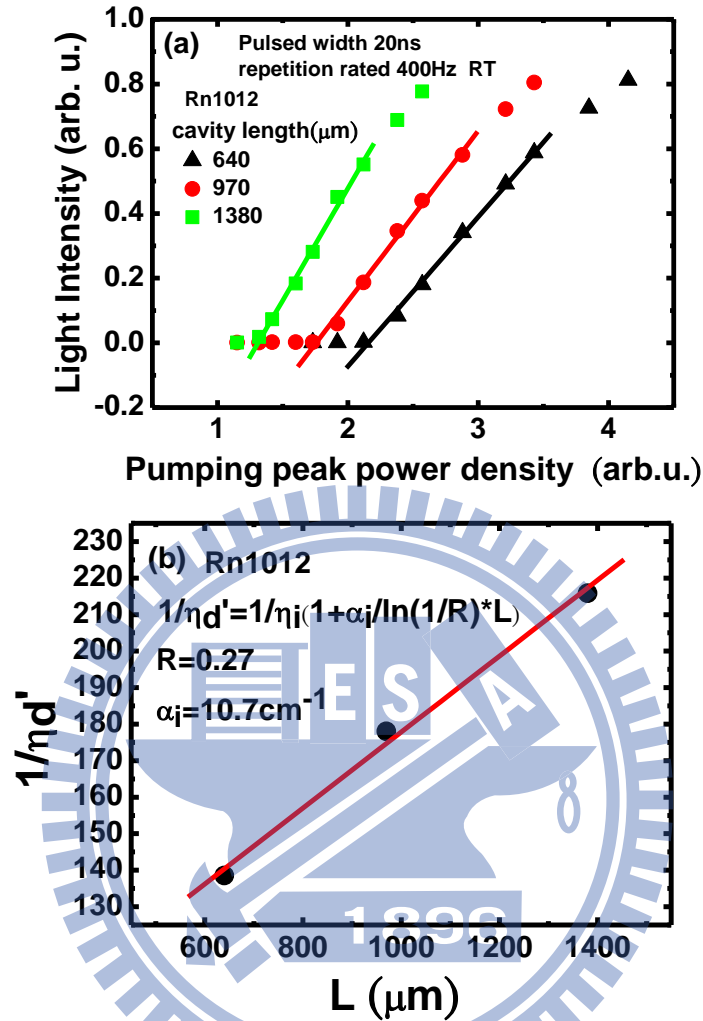
Fig. 5.6 (a) The L-L curves measured with different cavity length, and (b) the plot of inverse external quantum efficiency ($\eta d'$) versus cavity length (L) to extract internal loss (αi).

In order to further characterize our laser, we have measured the lasing performance at different temperatures. The temperature dependent L-L curves are plotted in Fig. 5.7. The extracted P_{th} as a function of temperature is shown in the inset (in log scale). It is found that the slope efficiency hardly changes for temperatures below 250K. The slowly increased P_{th} from 78K to 250K has a exponentially fitted characteristic temperature (T_0) of 487.8K. However, when the temperature is increased above 250K, the slope efficiency decreases and the threshold power increases at a much faster rate. The characteristic temperature is 41.8K

when the temperature goes beyond 250K. It is known that the monomolecular (Shockley-Read-Hall) recombination and the radiative recombination are dominating processes at low temperatures. But they could not cause this T_0 change behavior because the Shockley-Read-Hall coefficient varies with $\sim T^{1/2}$ and the radiative coefficient gradually decays with T. According to the theoretical analysis of ref.[53], the integrated PL intensity should decay with T^{-2} as temperature goes up if the defect related Shockley-Read recombination dominates the whole process. Our results, however, is quite different. The comparison between our measured result and the theoretical T^{-2} curve is shown in Fig. 5.8. The intensity decays at a much slower rate than what is predicted by the Schottky-Read-Hall process. The leakages due to escaped carriers should also not play a role here since both the E1 level in the conduction band and the HH1 level in the valence band are more than 300meV deep compared to the surrounding potential barriers. The most probable reason for the rapid increase of the threshold power when temperature goes beyond ~250K is the Auger processes.
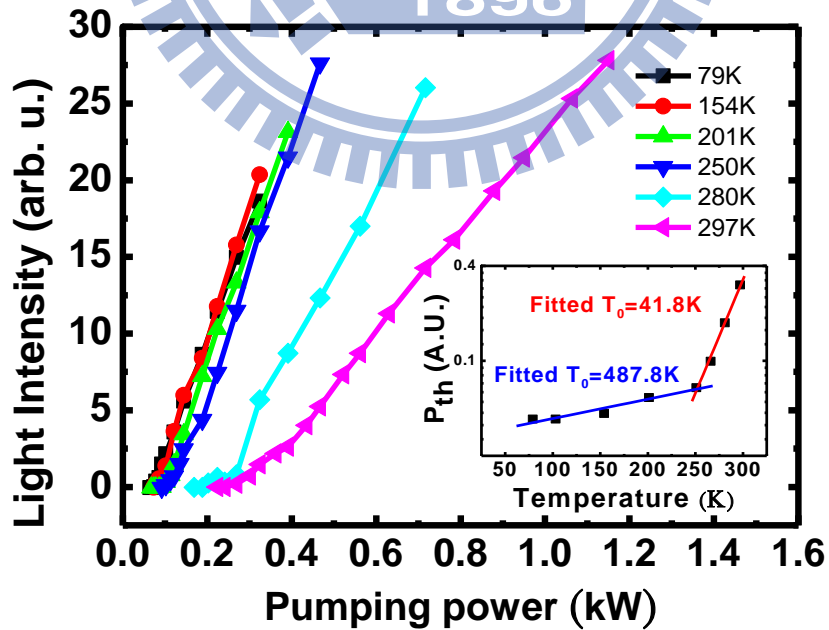
Fig. 5.7 L -L curves measured at different temperatures. The inset shows the plot of P_{th} as a function of temperature.
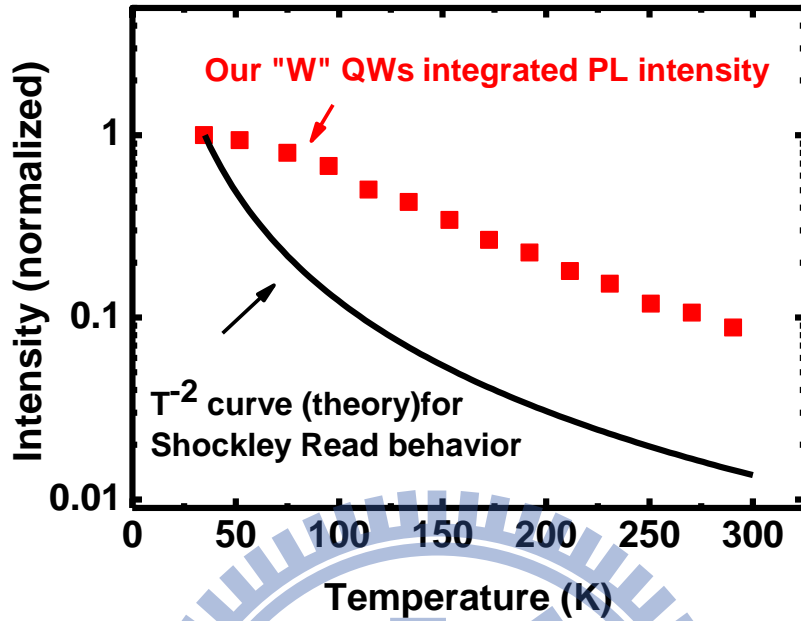
Fig. 5.8 The comparison between our "W" QWs integrated intensity changed along with temperature and the T^{-2} curve for the case of Shockley Read process dominated.

The amount of the Auger effect for our laser is analyzed in the following. We first calculated the laser's modal gain as a function of carrier density for multiple "W" quantum wells using the 8–band $k.p$ method including a Lorenzian line broadening function ($\Gamma=30$meV) and a confinement factor (17.6%) based on previous wave guide simulation. The result of the modal gain spectra with 2D carrier density varied from 1×10^{12}cm^{-2} to 3×10^{12}cm^{-2} are shown in Fig. 5.9. The theoretically obtained 2D transparency carrier density was ~1.1×10^{12}cm^{-2}. Based on the measured internal loss, 1mm long cavity mirror loss and the calculated modal gain, we estimated a 2D threshold density around 1.5×10^{12}cm^{-2} per well at room temperature. We can estimate the carrier life time (τ_{th}) at threshold using the relation, $\tau_{th} \approx N_{th}\hbar\omega_p/P_{th}f_{ab}(1-R)$, where N_{th}, $\hbar\omega_p$, f_{ab}, and R refer to the 2D threshold current density, the photon energy of the pump beam, the absorbed fraction, and the surface reflectivity, respectively. The obtained τ_{th} is in the range of ~0.6 ns. This will lead to an Auger coefficient,

$\gamma 3 \sim 1/(\tau_{th}(N_{th}/d)^2)$, of 1.67×10^{-27} cm^6/s at room temperature, where d of 15nm is used here for the thickness of one period "W" QW. This relatively high Auger coefficient explains why T_0 goes down at high temperatures. The value obtained is comparable to those in InAs/InGaSb type-II quantum wells on GaSb substrate, which also show similar T_0 at room temperatures [57, 58].
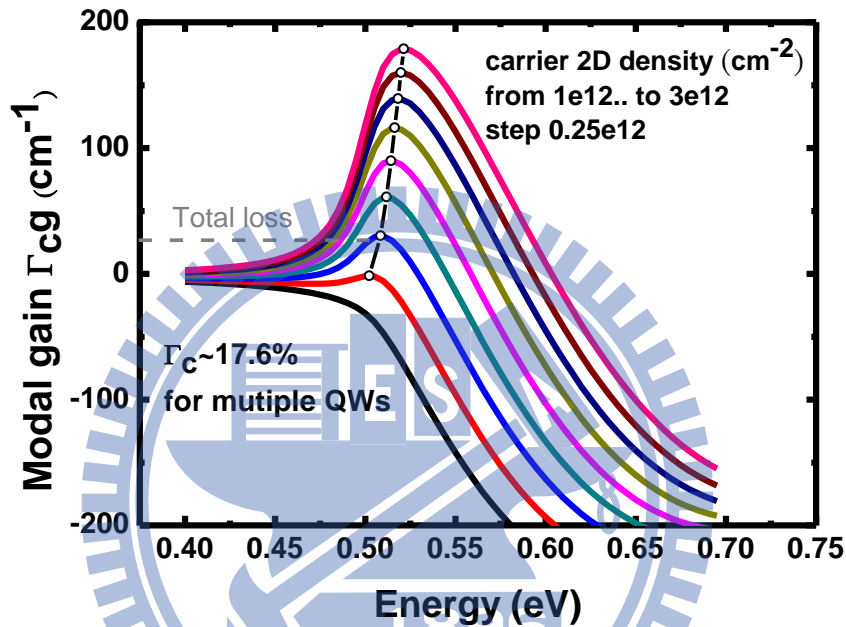
Fig. 5.9 Modal gain calculations based on the 8-band $k.p$ theory with 2D carrier density varied from 1×10^{12}cm^{-2} to 3×10^{12}cm^{-2}. The simulated confinement factor is ~17.6% and the total optical loss is indicated by the dash line.

The Auger processes often start to become dominated in a higher carrier density which is estimated around 5×10^{11} cm^{-2} for the "W" laser discussed above according to the threshold value at 250K. Not all "W" lasers we grown posse such a large T_0 in low temperature and an obvious T_0 change behavior as the operation temperature is raised. The temperature dependent L-L curves and the laser T_0 value versus operation temperature form the "W" laser sample named Rn1024, are shown in Fig. 5.10(a) and Fig. 5.10(b). The "W" structure layer thicknesses are the same as the precious one, however with Sb fraction around 0.65 in GaAsSb and total with 30 stacks of "W"QWs in the active region. The highest operation

temperature is up to 87°C with lasing wavelength at 2.42 μm shown in the inset of Fig. 5.10(b). We can see that the T_0 value in low temperature is 113.6K, which is smaller than the previous one, and is 41.7K around RT, which is similar to the previous sample. The T_0 change behavior is smoother and still around 250K. We found that the T_0 value changes to 22.2K as the operation temperature is raised above 340K. These phenomena, different T_0 behavior among samples and the correlation between the "W" QWs structure and Auger related processes are still under investigation.
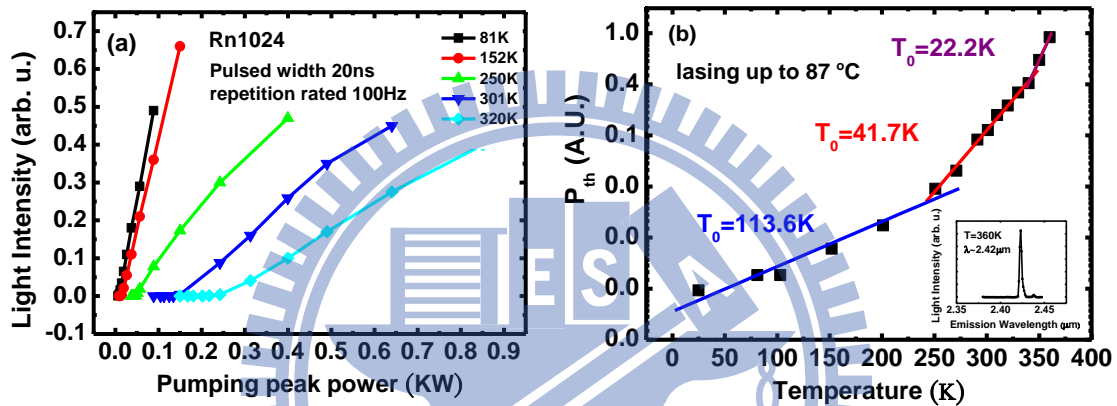
Fig. 5.10(a) Temperature dependent L -L curves for the "W" laser named Rn1024, and (b) the T_0 value versus the laser operation temperature. The inset shows the lasing spectrum at the highest operation temperature with a lasing peak at 2.42μm.

5.4 Conclusions

In conclusion, for the first time we have demonstrated the room temperature optically-pumped mid-IR "W" type lasers on InP substrates. The lasing wave length is 2.56 μm with a threshold pumping power density of ~40kW/cm^2. The laser shows a characteristic temperature (T_0) of 487.8K when it is operated below 250K and a T_0 of 41.8K near room temperature. The small T_0 at room temperature is considered due to the dominated Auger processes. An Auger coefficient of 1.67 x10^{-27} cm^6/s was estimated. More studies are needed to improve the laser performance. We believe that the "W" structure on InP substrates are promising for the fabrication of mid-IR optoelectronics devices.

Chapter 6

Conclusions and Future works

6.1 Conclusions of the present studies

In this dissertation, we have studied the type-II InGaAs/GaAsSb "W" QWs grown on InP substrates for the goal of developing cost effective mid-IR light sources and semiconductor lasers.

First, we have performed theoretical calculations and design considerations. The characteristic of trade-off between long emission wavelength and high optical transition rate is inherent to the "W" structure, which is revealed via one band effective mass approximation calculations with various structure parameters. However, according to our simulation results, a higher optical transition rate at a fixed emission wavelength can derived with using the design of thinner InGaAs/GaAsSb QWs thickness and higher Sb mole fration in GaAsSb alloy. We have calculated momentum matrix elements and material gains of designed "W" QWs based on eight band k.p theory. With the proper design the material gain of a single "W" QW can be readily above $10^3 cm^{-1}$ under a 2D carrier density of $3 \times 10^{12} cm^{-2}$. We also have shown that with proper compressive strain in GaAsSb hole QW by increasing Sb mole fraction can be beneficial, which leads to a smaller hole more effective mass and a more balance electron-hole effective masses. It then could reduce the transparency carrier density and enhance the material gain.

Second, we have successfully grown high quality samples in our MBE system varying the "W" structure parameters of InGaAs width, GaAsSb width, and Sb fraction in the GaAsSb alloy. The results of PL measurement show the 2-2.5 μm peak emission wavelengths for the samples in cryogenic temperature, and, for the first time, demonstrate over 3 μm emission

wavelength in RT. The integrated PL intensities of samples indeed reflect the trade-off characteristic and can be fitted well as comparing to calculation results. From cryogenic temperature to RT, the integrated PL intensities only decrease about an order, which indicates good sample quality. The blue shift behavior of peak emission wavelength as increasing excitation power for the type-II band alignment of "W" structure has been studied by power dependent PL measurements. The deviation from the theoretical predicted one-third rule has been explained by the purposed model of band filling of localized state, which is caused by the QW width roughness and the alloy composition disorder. The dependent of blue shift against excitation power could agree well with the simulation result.

Finally, we have demonstrated RT 2.56 μm mid-IR "W" QWs lasers via optical pumping, which are longest wavelength for the interband transition of QW grown on InP substrates as we known. The threshold pumping power density is ~40kW/cm^2. As laser operated temperature below 250K, the T_0 is 487.8K. However, it abruptly goes to 41.8K from 250K to RT. This behavior and small T_0 at RT are considered due to the dominated Auger recombination process. An Auger coefficient of 1.67 x10^{-27} cm^6/s has been estimated based on the laser analysis and the modal gain simulation results. More studies and analysis are needed to improve the mid-IR lasers performance. We believe that the "W" structure on InP substrates are promising for the fabrication of mid-IR optoelectronics devices.

6.2 Suggestions for the future works

6.2-1 Extending the InP-based "W" QWs mid-IR into 3-5 μm regime

We have mainly studies the InP-based InGaAs/GaAsSb "W" QWs in the wavelengths of 2-3μm region. For applications in atmospheric transparency window, one needs to extend to the emission wavelength into 3-5μm regime. In the current design, one can either increase the InGaAs/GaAsSb layer thickness to reduce quantization energies or increase Sb fraction in GaAsSb alloy to reduce type-II band offset (Δ) as indicated in Fig. 2.4. However, the optical momentum matrix might be too small for practical uses due to the trade-off feature of "W" QW as extending the wavelength into this regime. Besides, increasing Sb fraction in GaAsSb layer has its limit due to strain relaxation and forming dislocation which may degrade the film quality.

Here, we propose an approach that metamorphically grown buffer layers with lattice constant from 5.87A^o to 5.94A^o and then using the design of In$_{0.7}$Ga$_{0.3}$As/GaSb/In$_{0.7}$Ga$_{0.3}$As in "W" structure. Studies on metamorphic buffer layers on InP substrates are few especially for the realization of mid-IR lasers [59, 60]. There have been reports of using InAlAs and GaAsSb as metamorphic buffer layers grown InP substrates [61, 62]. In our proposed approach, only ~2% lattice relaxation is needed for InP-based materials to 5.94A^o system. It may easier to reduce and handle the generated dislocations and more prospective for the realization of high quality mid-IR devices.

There are at least two advantages for the 5.94 A^o system. One is that it could employ high-indium and lattice matched In$_{0.7}$Ga$_{0.3}$As ternary, which has lower energy band gap. The other is that it could grow binary GaSb thin pseudomorphic layer for hole QW in the "W" structure, which obviates the complexity of incorporating two V-groups as comparing to grow GaAsSb ternary. It also has suitable ~2% compressive strain for the hole QW design

consideration and the raised conduction band edge helps to extend emission wavelength into 3-5 μm regime.

The band alignment of a represented $In_{0.7}Ga_{0.3}As$ (4nm)/GaSb (2nm)/$In_{0.7}Al_{0.3}As$ "W" structure together with the electron and hole wavefunctions are shown in Fig. 6.1, which theoretically could emit 3.25μm mid-IR in RT. We calculated the emission wavelength and the matrix element based on the eight band k.p theory. Fig. 6.2(a) and Fig. 6.2(b) respectively show the layer thickness dependence of the "W" type QWs emission wavelength and the matrix element square. Basically in our modified range the of InGaAs and GaSb thicknesses, wavelength can be tuned up to ~4μm at RT while remaining the optical matrix element in a good value.
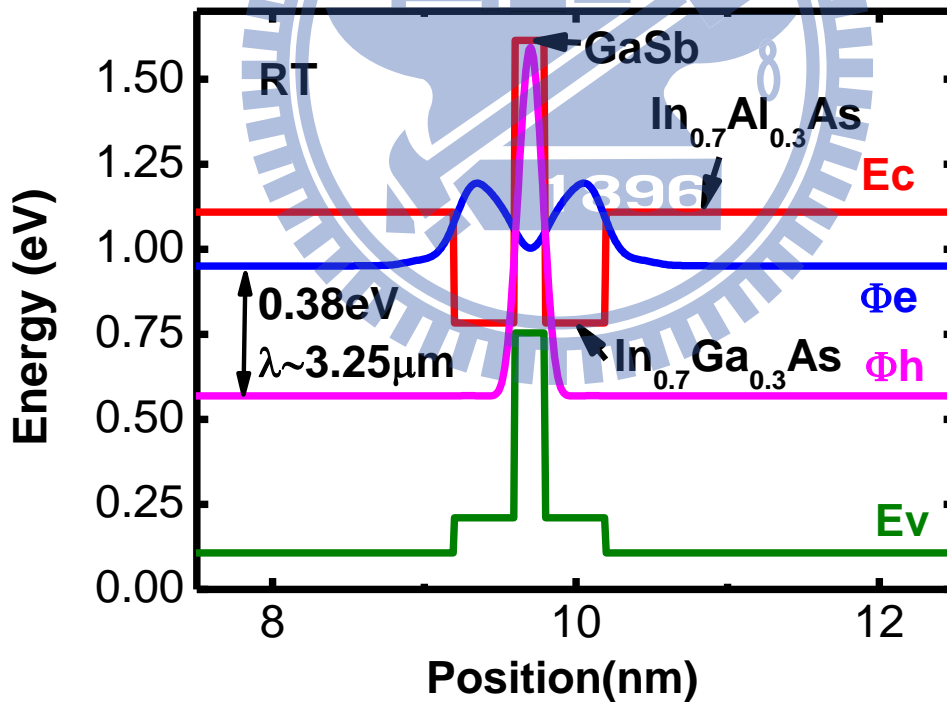
Fig. 6.1 Energy band diagram of the designed "W" type QW (InGaAs 4nm /GaSb 2nm/InAlAs) with the wavefunctions for electron and hole, which could emit 3.25 μm light in RT based on the eight band k.p theory calculation.

Wavelength(μm) @RT

Matrix element ^{2}(m$_0$∗eV) @RT
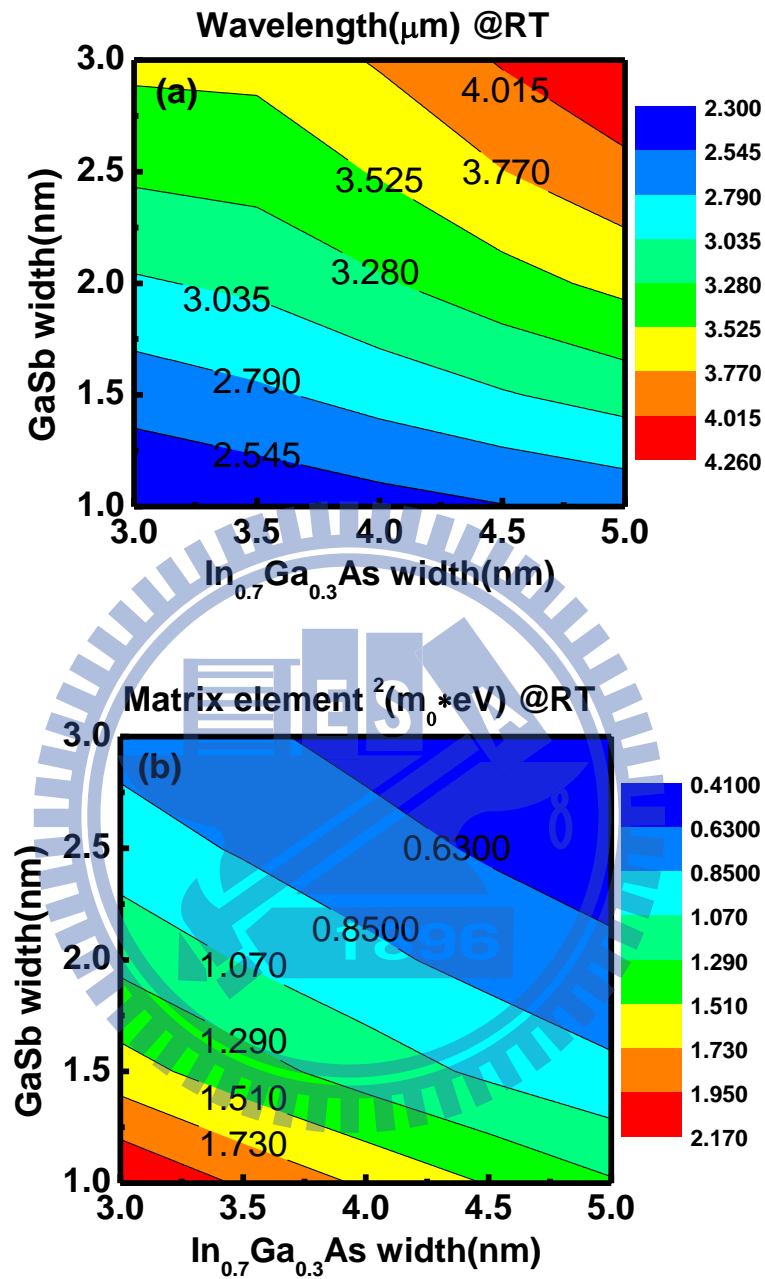
Fig. 6.2 Eight band k.p theoretically calculated contour plots of (a) emission wavelength and (b) the matrix element square versus GaSb (vertical axis) and In$_{0.7}$Ga$_{0.3}$As (horizontal axis) layer thickness.

6.2-2 Dual wavelength lasing of optically-pumped mid-IR lasers

and fabrication of tunable optically-pumped DFB lasers

Optically-pumped GaSb-based type-II "W" lasers own the records of highest output power and operated temperature, which is promising in the 3-4 μm range for the applications like range finding and free space communication [44, 63]. Optically-pumped mid lasers have another advantage that could operate dual wavelengths or even multiple wavelengths lasing at the same time [46, 64]. There are possible applications such as nonlinear optics generation, terahertz generation, two wavelength interferometry, and differential wavelength absorption spectroscopy.

In our lab, we accidentally grew an InP-based "W" laser with two wavelengths, as shown the low temperature PL spectrum in Fig. 6.3. One wavelength is centered in 2.23μm, while the other is in 2.35 μm. We performed the optical pumping experiment using the setup scheme depicted in Fig. 6.4. The 1064nm pumping source back illuminated and focused on the sample which was grown on the double side polished InP substrate. The light was collected from the top surface of the sample. The spectra measured along with increased pumping power are shown in Fig. 6.5 (in log scale).
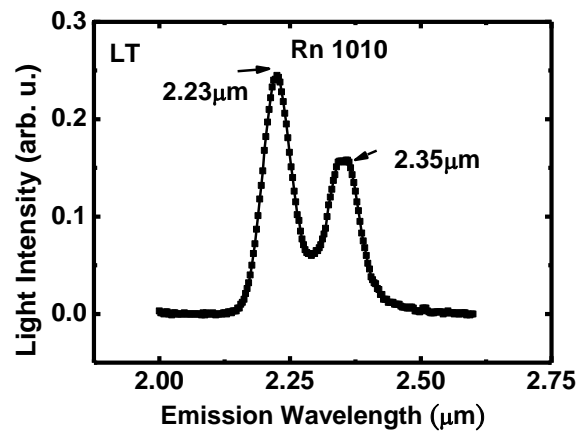
Fig. 6.3 PL spectrum of the InP-based "W" mid-IR laser with two kinds of emission wavelengths.
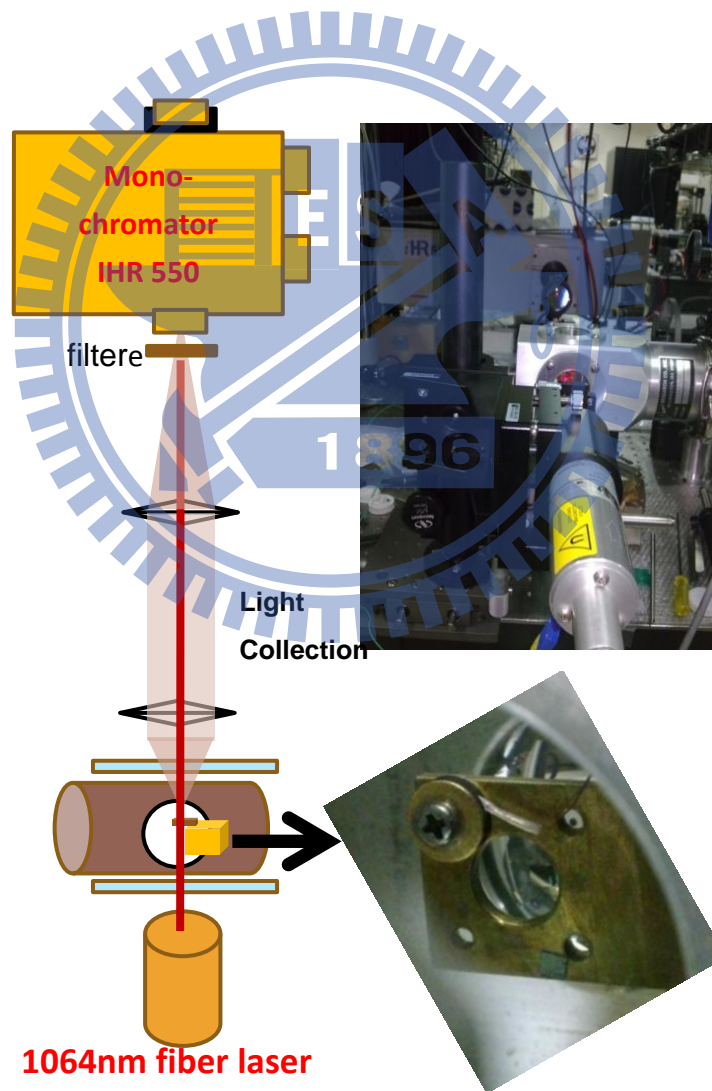
Fig. 6.4 The setup for optical pumping measurement with back illumination on the sample and light collection from the front surface.
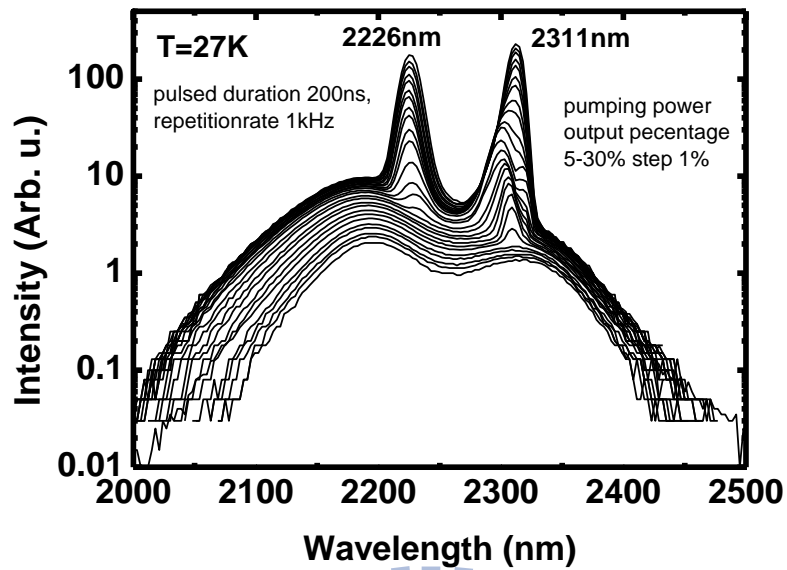
Fig. 6.5 The power dependent spectra of the optical pumping measurements for the InP-based ''W'' mid-IR laser with dual wavelengths.
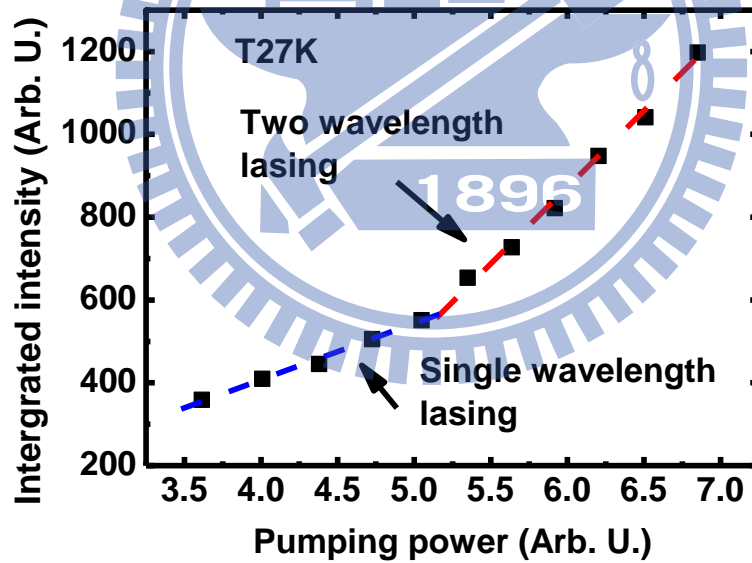
Fig. 6.6 The integrated intensity versus pumping power after lasing. The laser is operated under single wavelength lasing for the first slope and transit to two wavelengths lasing after the kink for the more oblique slope.

As seen in the Fig. 6.5, the broad spectra from spontaneous emission change to narrow lasing spectra as the pumping power increases above threshold. The edge-emitted lasing photons are scattered and collected via front-surface aligned light path to the monochromator showing more intense light than the spontaneous emission. The laser firstly operated in single wavelength lasing at 2311nm under lower pumping powers, and indeed can operated in dual wavelengths lasing (the other at 2262nm) after a certain sufficient pumping power. Drawing a plot of integrated intensity versus pumping power, it reveals a kink before and after two wavelengths lasing as shown in Fig 6.6.

We elaborately designed and grew the dual wavelength InP-based InGaAs/GaAsSb "W" mid-IR lasers hoping it could operate at room temperature. The structure is shown in Fig. 6.7.

"W" QW per stack		λ long	λ short
	$In_{0.52}Al_{0.48}As$	5	5
	$In_{0.36}Al_{0.32}Ga_{0.32}As$	2	1
	$In_{0.53}Ga_{0.47}As$	4	3
	$GaAs_{0.25}Sb_{0.75}$	3	2
	$In_{0.53}Ga_{0.47}As$	4	3
	$In_{0.36}Al_{0.32}Ga_{0.32}As$	2	1
	$In_{0.52}Al_{0.48}As$	5	5
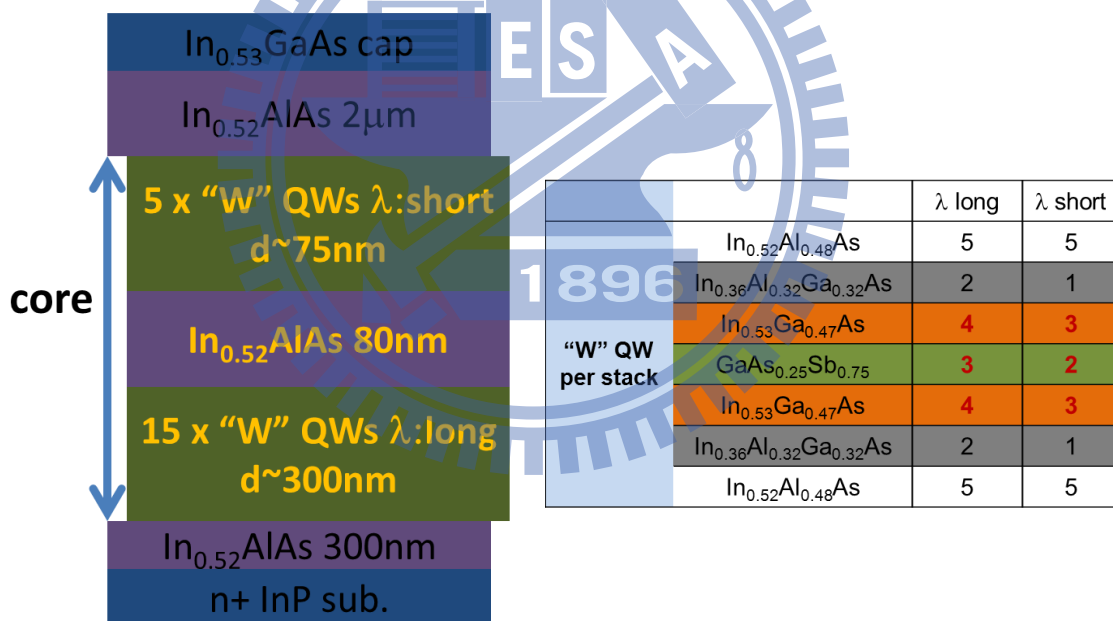
Fig. 6.7 The designed structure for the optically pumped InP-based "W" mid-IR laser with two kinds of QWs emitting different wavelengths, which are separated by the InAlAs partition layer inside the waveguide core.

The design includes two kinds "W" QWs; one is 15 period QWs with longer emission wavelength near the InP substrate, while the other is 5 period QWs, located on the top of the

waveguide core, with shorter emission wavelength by reducing the InGaAs/GaAsSb layer thicknesses of the "W" structure. The two sets of QWs are separated by the 80nm InAlAs partition layer inside the core, which prevents the interdiffusion of carriers inside the two sets QWs as optically pumping. Thus, ideally each of the QWs is capable get into carrier population inversion under a sufficient pumping power density. Once each media had enough modal gain that could conquer the optical loss, the laser is able to operate with dual wavelength lasing.

We have successfully got two wavelengths lasing at room temperature from the optical pumping measurements of the designed laser as shown in Fig. 6.8. The two lasing peaks (one at 2170nm, the other at 2440nm) have a wide separation over 200nm and comparable intensities.
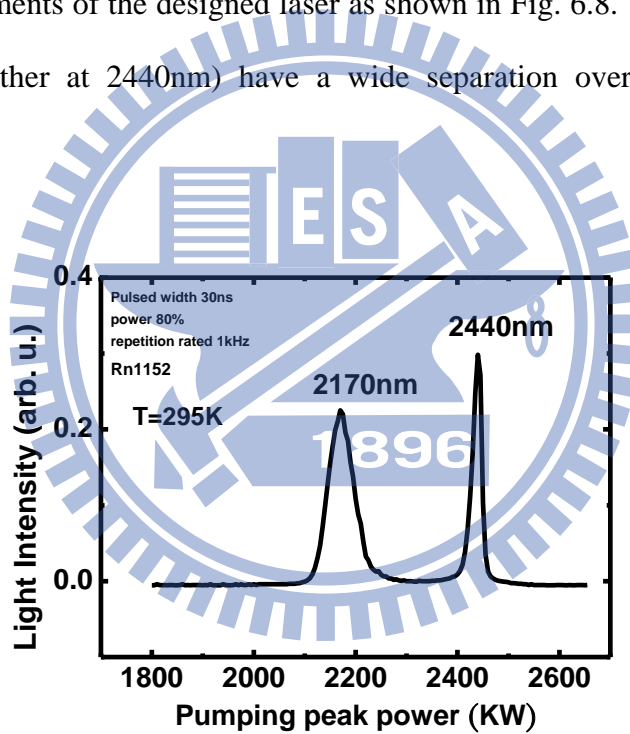
Fig. 6.8 Dual wavelength lasing spectra of the designed InP-based "W" QWs laser optically pumped at room temperature.

However, it needs more detail studies. During the process of increasing pumping power, we usually observed the blue shift of the long wavelength "W" QWs due to band filling effect and then the laser achieved lasing at shorter wavelength. The 2440nm lasing peak did not appear until exerting certain amount pumping power above the threshold after the lasing of

2170nm. The role of the 5 period short wavelength "W" QWs remain unclear. It may act like saturable absorber which increases the optical loss. We also discovered that the mid-IR lasing output power is far smaller than the 15 stack single medium "W" QWs laser. Rapidly switching between the two lasing wavelengths may happen. More laser dynamic measurements are needed to discuss the lasing behavior of the designed structure.

Multiple "W" QWs are suitable for broad band mid-IR light sources, one group recently demonstrated widely tunable optically pumped DFB laser [65]. They fabricated chirped grating by using interferometry lithography on mid-IR lasers based on type-II GaSb/InAs media. The grating and the pumping stripe have a ~6 °C tilted angle respect to the laser facet to suppress the longitudinal modes lasing. Over 80nm tuning range, from 3058nm to 3158nm, was achieved by shifting the pumping stripe position as shown in Fig. 6.9.

Similar ideas also can apply to our InP-based "W" mid-IR laser. Methods like chirped photonics crystal and DBR could be fabricated. Widely tuning range single mode mid-IR lasers than be developed and believed to be novel and possessed with application potential.
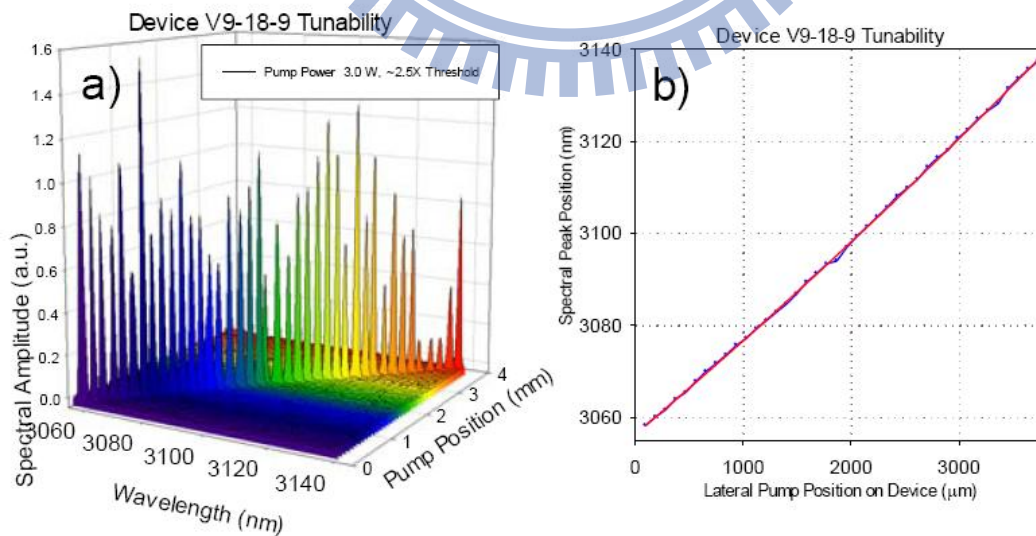
Fig. 6.9 (a) water full plot and (b) plot of the spectra peaks along with the variation of the pumping stripe position showing the tuning ability test of the device. [ref. 6.10]

6.2-3 Fabrication of electrical injection InP-based "W" mid-IR lasers

Electric injected InP-based "W" mid-IR lasers are ultimate goals since they are compact and easy to be integrated with other system. However, it is difficult for carriers to homogenously fill our multiple "W" QWs in the active region with vertically injected p-n laser diodes, and sometimes the resistance is large since the carriers need to come across many type-II hetero-interfaces before recombination. One possible way is to employ laterally injected p-n diodes. There are reports about fabricating lateral injection type or transverse injected devices [66-68]. The lateral p-n junction can be formed by methods of ion implantation, impurity diffusion, and structure regrowth. Carriers then could access to the multiple QWs active region more uniformly from side directions without passing interfaces of the heterojunction. One of the reports is also on the InP-based material [64], which employed the Zn-diffusion process to fabricate transvers p-n junction for broad optical bandwidth light-emitting-diodes (LEDs), the active region composed of $In_xAl_yGa_{1-x-y}As$ multiple QWs, as shown in Fig.10 (a). The result presents a wide optical bandwidth (580nm, from 1042 to 1622nm) and insensitive to bios current, as shown in Fig. 10(b), which is an evident for more uniformly distributed carriers inside the multiple QWs even under low current injection. It could be useful to develop our electrically injected InP-based "W" QWs mid-IR lasers or broad band mid-IR LEDs.
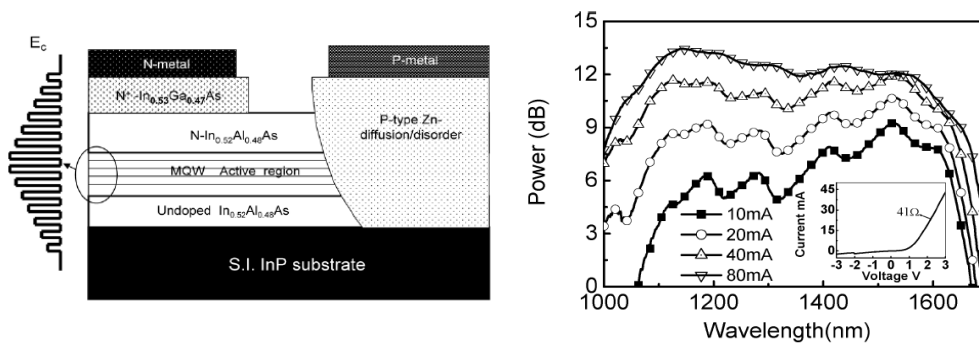
Fig. 6.10 (a) The structure of the Zn diffusion fabricated LED structure, the inset showing multiple QWs with different center wavelengths. (b) Measured spectra of the device under various bios currents and with the I-V curve in the inset. [ref. 64]

References

[1]   A. Joullié and P. Christol, "GaSb-based mid-infrared 2-5 μm laser diodes," *Comptes Rendus Physique,* vol. 4, pp. 621-637, 2003.

[2]   U. Willer, M. Saraji, A. Khorsandi, P. Geiser, and W. Schade, "Near- and mid-infrared laser monitoring of industrial processes, environment and security applications," *Optics and Lasers in Engineering,* vol. 44, pp. 699-710, Jul 2006.

[3]   L. S. Rothman, I. E. Gordon, A. Barbe, D. C. Benner, P. F. Bernath, M. Birk, V. Boudon, L. R. Brown, A. Campargue, J. P. Champion, K. Chance, L. H. Coudert, V. Dana, V. M. Devi, S. Fally, J. M. Flaud, R. R. Gamache, A. Goldman, D. Jacquemart, I. Kleiner, N. Lacome, W. J. Lafferty, J. Y. Mandin, S. T. Massie, S. N. Mikhailenko, C. E. Miller, N. Moazzen-Ahmadi, O. V. Naumenko, A. V. Nikitin, J. Orphal, V. I. Perevalov, A. Perrin, A. Predoi-Cross, C. P. Rinsland, M. Rotger, M. Šimečková, M. A. H. Smith, K. Sung, S. A. Tashkun, J. Tennyson, R. A. Toth, A. C. Vandaele, and J. Vander Auwera, "The HITRAN 2008 molecular spectroscopic database," *Journal of Quantitative Spectroscopy and Radiative Transfer,* vol. 110, pp. 533-572, 2009.

[4]   I. Vurgaftman, J. Meyer, and L. Ram-Mohan, "Band parameters for III-V compound semiconductors and their alloys," *Journal of Applied Physics,* vol. 89, p. 5815, 2001.

[5]   C. Caneau, A. K. Srivastava, A. G. Dentai, J. L. Zyskind, and M. A. Pollack, "Room-temperature GaInAsSb/AlGaAsSb DH injection lasers at 2.2 μm," *Electronics Letters,* vol. 21, pp. 815-817, 1985.

[6]   H. K. Choi and S. J. Eglash, "Room-temperature cw operation at 2.2 μm of GaInAsSb/AlGaAsSb diode lasers grown by molecular beam epitaxy," *Applied Physics Letters,* vol. 59, pp. 1165-1166, 1991.

[7]   W. Lei and C. Jagadish, "Lasers and photodetectors for mid-infrared 2-3 μm applications," *Journal of Applied Physics,* vol. 104, p. 091101, 2008.

[8]   Z. Yin and X. Tang, "A review of energy bandgap engineering in III-V semiconductor alloys for mid-infrared laser applications," *Solid-State Electronics,* vol. 51, pp. 6-15, 2007.

[9]   W. Li, J. Heroux, H. Shao, and W. Wang, "Strain-compensated InGaAsSb/AlGaAsSb mid-infrared quantum-well lasers," *Applied Physics Letters,* vol. 84, p. 2016, 2004.

[10]   M. Grau, C. Lin, O. Dier, C. Lauer, and M. C. Amann, "Room-temperature operation of 3.26 μm GaSb-based type-I lasers with quinternary AlGaInAsSb barriers," *Applied Physics Letters,* vol. 87, p. 241104, 2005.

[11]   L. Shterengas, G. Kipshidze, T. Hosoda, J. Chen, and G. Belenky, "Diode lasers emitting at 3 μm with 300 mW of continuous-wave output power," *Electronics Letters,* vol. 45, pp. 942-943, 2009.

[12]   T. Hosoda, G. Kipshidze, L. Shterengas, and G. Belenky, "Diode lasers emitting near

3.44 μm in continuous-wave regime at 300K," *Electronics Letters,* vol. 46, pp. 1455-1457, 2010.

[13] V. Kristijonas and A. Markus-Christian, "Room-temperature 3.73 μm GaSb-based type-I quantum-well lasers with quinternary barriers," *Semiconductor Science and Technology,* vol. 27, p. 032001, 2012.

[14] W. W. Bewley, C. L. Felix, E. H. Aifer, I. Vurgaftman, L. J. Olafsen, J. R. Meyer, H. Lee, R. U. Martinelli, J. C. Connolly, A. R. Sugg, G. H. Olsen, M. J. Yang, B. R. Bennett, and B. V. Shanabrook, "Above-room-temperature optically pumped midinfrared W lasers," *Applied Physics Letters,* vol. 73, pp. 3833-3835, 1998.

[15] W. W. Bewley, C. L. Felix, I. Vurgaftman, D. W. Stokes, E. H. Aifer, L. J. Olafsen, J. R. Meyer, M. J. Yang, B. V. Shanabrook, H. Lee, R. U. Martinelli, and A. R. Sugg, "High-temperature continuous-wave 3-6.1 μm "W" lasers with diamond-pressure-bond heat sinking," *Applied Physics Letters,* vol. 74, pp. 1075-1077, 1999.

[16] D. W. Stokes, L. J. Olafsen, W. W. Bewley, I. Vurgaftman, C. L. Felix, E. H. Aifer, J. R. Meyer, and M. J. Yang, "Type-II quantum-well "W" lasers emitting at λ=5.4-7.3 μm," *Journal of Applied Physics,* vol. 86, pp. 4729-4733, 1999.

[17] C. L. Canedy, W. W. Bewley, J. R. Lindle, I. Vurgaftman, C. S. Kim, M. Kim, and J. R. Meyer, "High-power continuous-wave midinfrared type-II "W" diode lasers," *Applied Physics Letters,* vol. 86, p. 211105, 2005.

[18] J. L. Bradshaw, R. Q. Yang, J. D. Bruno, J. T. Pham, and D. E. Wortman, "High-efficiency interband cascade lasers with peak power exceeding 4 W/facet," *Applied Physics Letters,* vol. 75, pp. 2362-2364, 1999.

[19] M. Kim, C. L. Canedy, W. W. Bewley, C. S. Kim, J. R. Lindle, J. Abell, I. Vurgaftman, and J. R. Meyer, "Interband cascade laser emitting at λ = 3.75 μm in continuous wave above room temperature," *Applied Physics Letters,* vol. 92, p. 191110, 2008.

[20] I. Vurgaftman, C. L. Canedy, C. S. Kim, M. Kim, W. W. Bewley, J. R. Lindle, J. Abell, and J. R. Meyer, "Mid-infrared interband cascade lasers operating at ambient temperatures," *New Journal of Physics,* vol. 11, p. 125015, 2009.

[21] A. Bauer, F. Langer, M. Dallner, M. Kamp, M. Motyka, G. Sek, K. Ryczko, J. Misiewicz, S. Hofling, and A. Forchel, "Emission wavelength tuning of interband cascade lasers in the 3-4 μm spectral range," *Applied Physics Letters,* vol. 95, p. 251103, 2009.

[22] J. R. Reboul, L. Cerutti, J. B. Rodriguez, P. Grech, and E. Tournie, "Continuous-wave operation above room temperature of GaSb-based laser diodes grown on Si," *Applied Physics Letters,* vol. 99, pp. 121113-3, 2011.

[23] J. B. Rodriguez, L. Cerutti, and E. Tournie, "GaSb-based, 2.2 μm type-I laser fabricated on GaAs substrate operating continuous wave at room temperature,"

Applied Physics Letters, vol. 94, p. 023506, 2009.

[24]   G. R. Nash, S. J. B. Przeslak, S. J. Smith, G. de Valicourt, A. D. Andreev, P. J. Carrington, M. Yin, A. Krier, S. D. Coomber, L. Buckle, M. T. Emeny, and T. Ashley, "Midinfrared GaInSb/AlGaInSb quantum well laser diodes operating above 200 K," *Applied Physics Letters,* vol. 94, p. 091111, 2009.

[25]   T. Sato, M. Mitsuhara, N. Nunoya, T. Fujisawa, K. Kasaya, E. Kano, and Y. Kondo, "2.33-mu m-wavelength distributed feedback lasers with InAs-In0.53Ga0.47As multiple-quantum wells on InP substrates," *IEEE Photonics Technology Letters,* vol. 20, pp. 1045-1047, 2008.

[26]   I. Vurgaftman, J. R. Meyer, N. Tansu, and L. J. Mawst, "InP-based dilute-nitride mid-infrared type-II ``W'' quantum-well lasers," *Journal of Applied Physics,* vol. 96, pp. 4653-4655, 2004.

[27]   J. Y. T. Huang, D. R. Xu, L. J. Mawst, T. F. Kuech, I. Vurgaftman, and J. R. Meyer, "GaAsSbN-GaAsSb-InP type-II "W" quantum wells for mid-IR emission," *IEEE Journal of Selected Topics in Quantum Electronics,* vol. 13, pp. 1065-1073, 2007.

[28]   J. Huang, L. Mawst, T. Kuech, X. Song, S. Babcock, C. Kim, I. Vurgaftman, J. Meyer, and A. Holmes, "Design and characterization of strained InGaAs/GaAsSb type-II ¡¥W¡ quantum wells on InP substrates for mid-IR emission," *Journal of Physics D: Applied Physics,* vol. 42, p. 025108, 2009.

[29]   S. Sprengel, C. Grasse, K. Vizbaras, T. Gruendl, and M.-C. Amann, "Up to 3 μm light emission on InP substrate using GaInAs/GaAsSb type-II quantum wells," *Applied Physics Letters,* vol. 99, p. 221109, 2011.

[30]   M. Nobile, H. Detz, E. Mujagic, A. M. Andrews, P. Klang, W. Schrenk, and G. Strasser, "Midinfrared intersubband absorption in InGaAs/GaAsSb multiple quantum wells," *Applied Physics Letters,* vol. 95, p. 041102, 2009.

[31]   C. Baile, A. L. Holmes, W. Y. Jiang, and J. Yuan, "Design of strain compensated InGaAs/GaAsSb type-II quantum well structures for mid-infrared photodiodes," *Numerical Simulation of Optoelectronic Devices (NUSOD) 11th International Conference*, pp. 203-204, 2011.

[32]   J. Hu, X. G. Xu, J. A. H. Stotz, S. P. Watkins, A. E. Curzon, M. L. W. Thewalt, N. Matine, and C. R. Bolognesi, "Type II photoluminescence and conduction band offsets of GaAsSb/InGaAs and GaAsSb/InP heterostructures grown by metalorganic vapor phase epitaxy," *Applied Physics Letters,* vol. 73, pp. 2799-2801, 1998.

[33]   M. Nobile, P. Klang, E. Mujagic, H. Detz, A. M. Andrews, W. Schrenk, and G. Strasser, "Quantum cascade laser utilising aluminium-free material system: InGaAs/GaAsSb lattice-matched to InP," *Electronics Letters,* vol. 45, pp. 1031-1033, 2009.

[34]   T. Mozume and N. Georgiev, "Interface control of InGaAs/AlAsSb heterostructures,"

Thin Solid Films, vol. 380, pp. 249-251, 2000.

[35] A. Yamamoto, Y. Kawamura, H. Naito, and N. Inoue, "Optical properties of GaAs0.5Sb0.5 and In0.53Ga0.47As/GaAs0.5Sb0.5 type II single hetero-structures lattice-matched to InP substrates grown by molecular beam epitaxy," *Journal of Crystal Growth,* vol. 201–202, pp. 872-876, 1999.

[36] C. G. Van de Walle, "Band lineups and deformation potentials in the model-solid theory," *Physical Review B,* vol. 39, pp. 1871-1883, 1989.

[37] M. P. C. M. Krijn, "Heterojunction band offsets and effective masses in III-V quaternary alloys," *Semiconductor Science and Technology,* vol. 6, p. 27, 1991.

[38] S. L. Chuang, Physics of Optoelectronic Devices (Wiley, New York, 1995).

[39] A. Zakharova, S. T. Yen, and K. A. Chao, "Strain-induced semimetal-semiconductor transition in InAs/GaSb broken-gap quantum wells," *Physical Review B,* vol. 66, p. 085312, 2002.

[40] B. A. Foreman, "Elimination of spurious solutions from eight-band k·p theory," *Physical Review B,* vol. 56, pp. R12748-R12751, 1997.

[41] M. Sugawara, "Theoretical calculation of optical gain in $In_xGa_{1-x}As$/InP quantum wells under biaxially compressive and tensile strain," *Applied Physics Letters,* vol. 60, pp. 1842-1844, 1992.

[42] M. Sugawara and S. Yamazaki, "Theoretical calculation of optical gain and threshold current density in strained $In_{1-x}Ga_xAs$/InP quantum-well lasers using strain-dependent conduction-band and valence-band structures (invited paper)," *Microwave and Optical Technology Letters,* vol. 7, pp. 107-113, 1994.

[43] R. Kaspi, A. P. Ongstad, G. C. Dente, J. R. Chavez, M. L. Tilton, and D. M. Gianardi, "High performance optically pumped antimonide lasers operating in the 2.4-9.3 μm wavelength range," *Applied Physics Letters,* vol. 88, p. 041122, 2006.

[44] T. C. McAlpine, K. R. Greene, M. R. Santilli, L. J. Olafsen, W. W. Bewley, C. L. Felix, I. Vurgaftman, J. R. Meyer, H. Lee, and R. U. Martinelli, "Resonantly pumped optical pumping injection cavity lasers," *Journal of Applied Physics,* vol. 96, pp. 4751-4754, 2004.

[45] L. J. Olafsen and T. C. McAlpine, "Transparency pump intensity and differential gain in resonantly pumped W optical pumping injection cavity lasers," *Journal of Applied Physics,* vol. 108, p. 053106, 2010.

[46] R. Kaspi, A. P. Ongstad, G. C. Dente, M. L. Tilton, and A. Tauke-Pedretti, "Optically Pumped Midinfrared Laser With Simultaneous Dual-Wavelength Emission," *IEEE Photonics Technology Letters,* vol. 20, pp. 1467-1469, 2008.

[47] S. D. Wu, L. W. Guo, W. X. Wang, Z. H. Li, X. Z. Shang, H. Y. Hu, Q. Huang, and J. M. Zhou, "The incorporation behavior of arsenic and antimony in GaAsSb/GaAs grown by solid source molecular beam epitaxy," *Journal of Crystal Growth,* vol. 270,

pp. 359-363, 2004.

[48] K. Biermann, A. Hase, and H. Künzel, "Optical pyrometry for in situ control of MBE growth of (Al,Ga)As$_{1-x}$Sb$_x$ compounds on InP," *Journal of Crystal Growth,* vol. 201–202, pp. 36-39, 1999.

[49] L. Mawst, J. Huang, D. Xu, J. Yeh, G. Tsvid, T. Kuech, and N. Tansu, "MOCVD-Grown Dilute Nitride Type II Quantum Wells," *IEEE Journal of Selected Topics in Quantum Electronics,* vol. 14, pp. 979-991, 2008.

[50] J. Klem, O. Blum, S. Kurtz, I. Fritz, and K. Choquette, "GaAsSb/InGaAs type-II quantum wells for long-wavelength lasers on GaAs substrates," *Journal of Vacuum Science & Technology B: Microelectronics and Nanometer Structures,* vol. 18, p. 1605, 2000.

[51] C. Renard, X. Marcadet, J. Massies, and O. Parillaud, "Molecular beam epitaxy of (Ga,Al)AsSb alloys on InP(001) substrates," *Journal of Crystal Growth,* vol. 278, pp. 193-197, 2005.

[52] N. N. Ledentsov, J. Böhrer, M. Beer, F. Heinrichsdorff, M. Grundmann, D. Bimberg, S. V. Ivanov, B. Y. Meltser, S. V. Shaposhnikov, I. N. Yassievich, N. N. Faleev, P. S. Kop'ev, and Z. I. Alferov, "Radiative states in type-II GaSb/GaAs quantum wells," *Physical Review B,* vol. 52, p. 14058, 1995.

[53] M. C. Lo, S. J. Huang, C. P. Lee, S. D. Lin, and S. T. Yen, "Discrete monolayer light emission from GaSb wetting layer in GaAs," *Applied Physics Letters,* vol. 90, p. 243102, 2007.

[54] A. Ait-Ouali, R. Yip, J. Brebner, and R. Masut, "Strain relaxation and exciton localization effects on the Stokes shift in InAsP/InP multiple quantum wells," *Journal of Applied Physics,* vol. 83, p. 3153, 1998.

[55] M. Dinu, J. E. Cunningham, F. Quochi, and J. Shah, "Optical properties of strained antimonide-based heterostructures," *Journal of Applied Physics,* vol. 94, pp. 1506-1512, 2003.

[56] J. Christen and D. Bimberg, "Line shapes of intersubband and excitonic recombination in quantum wells: Influence of final-state interaction, statistical broadening, and momentum conservation," *Physical Review B,* vol. 42, p. 7213, 1990.

[57] C. L. Felix, J. R. Meyer, I. Vurgaftman, C. H. Lin, S. J. Murry, D. Zhang, and S. S. Pei, "High-temperature 4.5-µm type-II quantum-well laser with Auger suppression," *IEEE Photonics Technology Letters,* vol. 9, pp. 734-736, 1997.

[58] J. R. Meyer, C. L. Felix, W. W. Bewley, I. Vurgaftman, E. H. Aifer, L. J. Olafsen, J. R. Lindle, C. A. Hoffman, M. J. Yang, B. R. Bennett, B. V. Shanabrook, H. Lee, C. H. Lin, S. S. Pei, and R. H. Miles, "Auger coefficients in type-II InAs/Ga$_{1-x}$In$_x$Sb quantum wells," *Applied Physics Letters,* vol. 73, pp. 2857-2859, 1998.

[59] A. Krier, D. Chubb, S. E. Krier, M. Hopkinson, and G. Hill, "Light sources for

wavelengths >2 μm grown by MBE on InP using a strain relaxed buffer," *IEE Proceeding-Optoelectronics,* vol. 145, pp. 292-296, 1998.

[60]   J. Kirch, T. Garrod, S. Kim, J. H. Park, J. C. Shin, L. J. Mawst, T. F. Kuech, X. Song, S. E. Babcock, I. Vurgaftman, J. R. Meyer, and T.-S. Kuan, "InAs$_y$P$_{1-y}$ metamorphic buffer layers on InP substrates for mid-IR diode lasers," *Journal of Crystal Growth,* vol. 312, pp. 1165-1169, 2010.

[61]   F. M. Mohammedy, O. Hulko, B. J. Robinson, D. A. Thompson, M. J. Deen, and J. G. Simmons, "Growth and characterization of GaAsSb metamorphic samples on an InP substrate," *Journal of Vacuum Science & Technology A: Vacuum, Surfaces, and Films,* vol. 24, pp. 587-590, 2006.

[62]   Y. Zhang, Y. Gu, Z. Tian, A. Li, X. Zhu, and Y. Zheng, "Wavelength extended 2.4 μm heterojunction InGaAs photodiodes with InAlAs cap and linearly graded buffer layers suitable for both front and back illuminations," *Infrared Physics & Technology,* vol. 51, pp. 316-321, 2008.

[63]   A. P. Ongstad, R. Kaspi, G. C. Dente, M. L. Tilton, and J. Chavez, "Midinfrared, optically pumped, unstable resonator lasers," *Applied Physics Letters,* vol. 90, p. 191107, 2007.

[64]   A. P. Ongstad, R. Kaspi, A. Tauke-Pedretti, J. C. Chavez, M. L. Tilton, and G. C. Dente, "Controlling the outcoupled power in a dual wavelength optically pumped semiconductor laser," *Applied Physics Letters,* vol. 94, p. 241111, 2009.

[65]   X. He, S. Benoit, S. R. Brueck, and R. Kaspi, "Widely Tunable Optically Pumped Mid-IR DFB Laser," Lasers and Electro-Optics (CLEO) Conference, p. CF1K.7, May 2012.

[66]   S.-Y. Yang and J.-B. Yoo, "Characteristics of Zn diffusion in planar and patterned InP substrate using Zn$_3$P$_2$ film and rapid thermal annealing process," *Surface and Coatings Technology,* vol. 131, pp. 66-69, 2000.

[67]   J. W. Shi, T. J. Hung, Y. Y. Chen, Y. S. Wu, L. Wei, and Y. Ying-Jay, "InP-Based Transverse Junction Light-Emitting Diodes for White-Light Generation at Infrared Wavelengths," *Photonics Technology Letters, IEEE,* vol. 18, pp. 2053-2055, 2006.

[68]   T. Shindo, T. Okumura, H. Ito, T. Koguchi, D. Takahashi, Y. Atsumi, J. Kang, R. Osabe, T. Amemiya, N. Nishiyama, and S. Arai, "GaInAsP/InP lateral-current-injection distributed feedback laser with a-Si surface grating," *Opt. Express,* vol. 19, pp. 1884-1891, 2011.

Vita

Name: Chien-Hung Pan (潘建宏)

Date of birth: May 8, 1984

Place of birth: Hualien, Taiwan, ROC

E-mail: panjoan.ee95g@g2.nctu.edu.tw

Sex: Male

Education:

National Chiao Tung University   Ph. D.   September, 2007－December, 2012

Department of Electronics Engineering & Institute of Electronics

National Chiao Tung University   M. S.   September, 2006－June, 2007

Department of Electronics Engineering & Institute of Electronics

National Chiao Tung University   B. S.   September, 2002－June, 2006

Department of Electrophysics

Title of Ph. D. Dissertation:

Optical Characteristics of Type-II InGaAs/GaAsSb "W" Quantum Wells and

Optically-Pumped Mid Infrared Lasers

Publication List

[1] **C. H. Pan,** S. D. Lin, and C. P. Lee**, "**2-3μm mid infrared light sources using InGaAs/GaAsSb "W" type quantum wells on InP substrates," *J. Appl. Phys.,* vol. 108, pp. 103105-103109, 2010.

[2] **C. H. Pan,** C. H. Chang, and C. P. Lee, "Room Temperature Optically Pumped 2.56-μm Lasers With "W" Type InGaAs/GaAsSb Quantum Wells on InP Substrates," *Photonics Technology Letters, IEEE,* vol. 24, pp. 1145-1147, 2012.

[3] **C. H. Pan,** S. D. Lin, and C. P. Lee, "2~2.5μm mid infrared light sources using InGaAs/GaAsSb "W" type quantum wells on InP substrates," 16th international conference in molecular beam epitaxy 2010, Berlin, German (Aug. 22-27, 2010)

[4] **C. H. Pan**, C. H. Chang, S. D. Lin, C. P. Lee, "Room temperature 2.38 μm laser using InGaAs/GaAsSb W-type quantum wells on InP substrate," Optics and Photonics Japan (OPJ 2010), Tokyo, Japan (Nov. 2010).

[5] C. Cheng, S.-D. Lin, **C.-H. Pan**, C.-H. Lin, and Y.-J. Fu, "Observation of long-lived excitons in InAs quantum dots under thermal redistribution temperature," *Physics Letters A,* vol. 376, pp. 1495-1498, 2012.

[6] C. Cheng, S.-D. Lin, **C.-H. Pan** and C.-H. Lin, "Low-temperature hump of time-resolved photoluminescence in InAs quantum dots," Oral presentation on *IEEE International NanoElectronics Conference* , Taoyuan, Taiwan (2011).

[7] **C. H. Pan** and C. P. Lee, "Design and modeling of InP-based InGaAs/GaAsSb type-II "W" type quantum well mid-Infrared lasers, " submitted to *J. Appl. Phys.*, 2012 and has been accepted in 2013 Jan..